

REVIEW**Ultrafast Electron Diffraction (UED)
A New Development for the 4D Determination of Transient Molecular Structures**by **Ramesh Srinivasan, Vladimir A. Lobastov, Chong-Yu Ruan, and Ahmed H. Zewail*¹⁾**Laboratory for Molecular Sciences, Arthur Amos Noyes Laboratory of Chemical Physics, California Institute of Technology, Pasadena, CA 91125, USA
(phone: 626395 6536; fax: 626792 8456; e-mail: zewail@caltech.edu)

With properly timed sequences of ultrafast electron pulses, it is now possible to image complex molecular structures in the four dimensions of space and time with resolutions of 0.01 Å and 1 ps, respectively. The new limits of ultrafast electron diffraction (UED) provide the means for the determination of transient molecular structures, including reactive intermediates and non-equilibrium structures of complex energy landscapes. By freezing structures on the ultrafast timescale, we are able to develop concepts that correlate *structure* with *dynamics*. Examples include structure-driven radiationless processes, dynamics-driven reaction stereochemistry, pseudorotary transition-state structures, and non-equilibrium structures exhibiting negative temperature, bifurcation, or selective energy localization in bonds. These successes in the studies of complex molecular systems, even without heavy atoms, and the recent development of a new machine devoted to structures in the condensed phase, establish UED as a powerful method for mapping out temporally changing molecular structures in chemistry, and potentially, in biology. This review highlights the advances made at Caltech, with emphasis on the principles of UED, its evolution through four generations of instrumentation (UED-1 to UED-4) and its diverse applications.

Table of Contents

1. Introduction
2. Principles of UED
 - 2.1. Concepts
 - 2.2. Theory
 - 2.3. The Diffraction-Difference Method – Transient Structures
 - 2.4. Ground-State Structures
 - 2.5. Structure Search and Refinement
3. Generations of UED
 - 3.1. Instrumentation
 - 3.1.1. Femtosecond Laser System
 - 3.1.2. Vacuum Chambers and Molecular Beams
 - 3.1.3. Electron Gun
 - 3.1.4. CCD Camera System
 - 3.2. UED Methodology
 - 3.2.1. Streaking: Electron Pulse Characterization

¹⁾ We are very pleased to contribute this invited review article in honor of Professor *Jack D. Dunitz*, a friend, scholar, and polymath.

- 3.2.2. Clocking: Zero of Time
- 3.2.3. Temporal and Spatial Overlap: Velocity Mismatch
- 4. Scope of Applications of UED
 - 4.1. Bond Breaking and Bond Making
 - 4.1.1. Ground State of Pyridine
 - 4.1.2. Transient Structure of Pyridine
 - 4.2. Reactive Intermediate Structures
 - 4.2.1. Ground-State Structures of $C_2F_4I_2$
 - 4.2.2. Structural Dynamics of the $C_2F_4I_2$ Reaction
 - 4.2.3. Freezing the Structure of the C_2F_4I Intermediate
 - 4.3. Transition-State Pseudorotary Structures
 - 4.3.1. Ground State of $CpCo(CO)_2$
 - 4.3.2. Transient Structures of Cp
 - 4.4. Non-Equilibrium Structures
 - 4.4.1. Concepts of Equilibrium vs. Non-Equilibrium Structures
 - 4.4.2. Ground-State Structures of CHT, CHD, and COT3
 - 4.4.3. Thermal *Cope* Rearrangement of COT3
 - 4.4.4. Structural Dynamics of CHT
 - 4.4.5. Structural Dynamics of CHD
 - 4.4.6. Structural Dynamics of COT3
 - 4.5. From Carbenes to Organometallics
 - 4.5.1. Carbenes
 - 4.5.2. Organometallics
- 5. The Future of Ultrafast Electron Diffraction

1. Introduction

The twentieth century has been witness to major advances in our ability to peer into the microscopic world of molecules, thereby giving us unparalleled insights into their static and temporal behavior [1]. Beginning with X-rays at the turn of the 20th century, diffraction techniques have allowed determination of *equilibrium* three-dimensional structures with atomic resolution, in systems ranging from diatoms (NaCl) to DNA, proteins, and complex assemblies such as viruses [2]. For dynamics, the time resolution has similarly reached the fundamental atomic-scale of motion. With the advent of femtosecond time resolution nearly two decades ago, it has become possible to study – in real time – the dynamics of *non-equilibrium* molecular systems, also from the very small (NaI) to the very large (DNA, proteins and their complexes) [3].

Armed with this ability to capture both the static architecture as well as the temporal behavior of the chemical bond, a tantalizing goal that now stimulates researchers the world over is the potential to map out, in real time, the coordinates of all individual atoms in a reaction, as, for example, when a molecule unfolds to form selective conformations, or when a protein docks onto the cell surface. These transient structures provide important insights into the function of chemical and biological molecules. As function is intimately associated with intrinsic conformational dynamics, knowing a molecule's static structure is often only the first step toward unraveling how

the molecule functions, especially in the world of biology. Thus, elucidating the real-time ‘structural dynamics’ of *far-from-equilibrium* conformations at atomic scale resolution is vital to understanding the fundamental mechanisms of *complex* chemical and biological systems.

Time-resolved experiments with femtosecond time resolution have been performed in the past with probe wavelengths ranging from the ultraviolet to the infrared and far-infrared. On this time scale, one is able to freeze localized structures in space (wave packets) and observe their evolution in time – thus elucidating the elementary processes of bond transformation *via* transition states, in chemistry and biology [3–9]. Recent advances have been made in multidimensional spectroscopy to correlate frequencies of optical transitions with temporal evolution, thereby probing structural changes in different relaxation processes (see [10][11] and refs. cit. therein). For complex molecular structures, however, the positions of all atoms at a given time can only be obtained if the probe is able to ‘see’ interferences of all atoms. Diffraction methods using X-rays or electrons have the unique ability of revealing all internuclear coordinates with very high spatial resolution, thus providing a global picture of structural change on the ultrafast time scale with atomic level detail.

Electron or X-ray pulses can, in principle, be used to obtain time-varying molecular structures. These pulses must be short enough to freeze the atomic motions, yet bright enough to provide a discernible diffraction pattern. In the case of X-rays, photons are scattered by electrons in the molecular sample, so the diffracted intensity depends directly on the electronic density. Because most electrons are centered on atoms, these electron densities reflect the positions of nuclei, especially for heavy atoms. At present, ultrafast pulsed X-ray sources include third-generation synchrotron radiation, laser-produced plasma sources, high-order harmonics production in gases and on solid surfaces, and free-electron lasers (see [12] and refs. cit. therein). While high-flux X-ray pulses from synchrotron sources are relatively long (tens of picoseconds; dictated by the duration of electron bunches in a storage ring), the sub-picosecond X-ray pulses from other generation schemes suffer from rather low fluxes [13]. As a result, ultrafast X-ray diffraction studies have primarily focused on solid samples (see, *e.g.*, [12][14] and refs. cit. therein) where the intrinsic long-range order enhances the signal-to-noise ratio of the interference patterns. X-Ray absorption spectroscopy (XAS) techniques such as extended X-ray absorption fine structure (EXAFS) and X-ray absorption near-edge structure (XANES) spectroscopies have been used to obtain local structural information in solutions on the nanosecond timescale [15][16], and on the ultrafast timescale, in gases [17] and liquids [18].

The method of choice in our laboratory has been ultrafast electron diffraction (UED), which has unique advantages. First, unlike X-ray photons, which are scattered by the electron distribution (*Thompson* scattering), electrons are scattered by both the atomic nuclei and the electron distribution. Because of *Coulomb* scattering, electron-scattering cross-section is some six orders of magnitude stronger than X-ray scattering from molecules [19]. It was this feature of electron–matter interaction that prompted *Mark* and *Wierl* in 1930 [20] to use electrons (instead of X-rays) to study gas-phase molecular structures; they produced a diffraction pattern from CCl_4 that was more distinct than similar X-ray scattering exposures obtained earlier by *Debye* and co-workers [21], and required a fraction of the exposure time (1 s compared to 20 h for the

X-ray pattern). Second, UED experiments are ‘tabletop’ scale and can be implemented with ultrafast laser sources. Third, electrons are less damaging to specimens per useful scattering event. For example, using electrons in microscopy [22] has shown [23] that the ratio of inelastic/elastic scattering events for 80–500 keV electrons is 3, and that for 1.5-Å X-rays is 10. The energy deposited per inelastic scattering event for 1.5-Å X-rays is 400 times that of electrons, thus implying that the energy deposited per useful (elastic) scattering event is 1000 times smaller for 80–500 keV electrons. Fourth, electrons, because of their short penetration depth arising from strong interaction with matter, are well-suited for surface characterization, gases, and thin samples.

Imaging transient molecular structures on ultrafast time scales demands not only the marriage of ultrafast probing techniques with those of conventional diffraction, but also the development of new concepts for reaching simultaneously the temporal and spatial resolutions of atomic scale. Following the development of femtochemistry in the mid 1980s, we embarked upon the challenge of achieving time-resolved electron diffraction in the sub-picosecond and picosecond regime. In 1991, we proposed that replacing the ‘probe’ laser pulse in femtochemistry experiments with an electron pulse would open up new vistas in our understanding of structural dynamics [24][25]. A year later, we reported diffraction patterns with picosecond electron pulses, but without recording the temporal evolution of the reaction [26]. Since those first images, technical and theoretical advances in our laboratory [27–42] have culminated in the third-generation UED apparatus (UED-3) with spatial and temporal resolution of 0.01 Å and 1 ps, respectively [35]. Moreover, we can now detect chemical change as low as 1%. As a result of these advances, a wide variety of phenomena have been studied in our laboratory [27–42]. Recently, we have completed the design and construction of our fourth-generation instrument (UED-4) for the studies of condensed matter and biological systems.

Historically, the first gas-phase electron diffraction (GED) investigation of a molecular structure, that of CCl_4 , was reported by *Mark* and *Wierl* in 1930 [20], only three years after the discovery of electron diffraction by *Davisson* and *Germer* for a crystal of nickel [43], and by *Thomson* and *Reid* for a thin film of celluloid [44]. The utility of gas-phase electron diffraction was recognized by several research groups, beginning with that of *Linus Pauling* and his graduate student, *Lawrence Brockway* [45] at Caltech. GED was further refined to elucidate the precise arrangement of atoms in molecules for understanding the *static* nature of the chemical bond (see, e.g., [46–48] and refs. cit. therein). The original method for analyzing GED data, initiated by *Mark* and *Wierl*, and further developed by *Pauling* and *Brockway*, was called the ‘visual method’ because the patterns were analyzed simply by measuring the positions of maxima and minima, and estimating their relative height and depth by eye, thanks to the extraordinary ability of the human eye to correct for the steeply falling background. Soon, however, a more direct method of determining bond distances was proposed by *Pauling* and *Brockway* [49] – the so-called radial distribution method – that invoked the *Fourier* transform of the estimated intensity data.

A significant advance in the quantitative measurement of the intensity distribution was the introduction of the ‘rotating sector’ into the diffraction apparatus, proposed by *Trendelenburg* [50], *Finbak* [51], and *Debye* [52] in the 1930s, which obviated the use of visual estimates. This rotating sector (a metallic disk of special shape) – which

attenuates the inner, more intense part of the pattern, effectively enhancing the outer, weaker signals – was a crucial step in the development of what came to be known as the ‘sector-microphotometer’ method. Until the early 1970s, diffraction patterns were recorded exclusively with photographic film. The replacement of these film-based detectors with an electronic detector by *Fink* and *Bonham* [53] was a turning point towards electronic microdensitometry – evolving from scintillator-photomultipliers [54][55] to linear array detectors [56]. The introduction of 2D area detectors – charge-coupled device (CCD) with fiber optic coupling and image intensification – in our laboratory [26][30][35] represents the current state-of-the-art in digital diffraction imaging.

It is not surprising that the earliest attempts at introducing time resolution into electron diffraction mirrored the development of digital detection techniques. *Ischenko et al.* [57] created microsecond electron pulses by chopping a continuous electron beam with an electromagnetic chopper to study the IR multiphoton dissociation of CF_3I (see [48]) for a critique. *Rood* and *Milledge* [58] conducted diffraction studies on the decomposition of ClO_2 with 100- μs electron pulses, while *Bartell* and *Dibble* [59] studied phase change in clusters produced in supersonic jets, with a time-of-flight resolution of *ca.* 1 μs . *Ewbank et al.* [60] advanced the temporal resolution to nanoseconds (and later shorter [61]) by combining a laser-initiated electron source with a linear diode array detector, and investigated the photofragmentation of small molecules (*e.g.*, CS_2). *Mourou* and *Williamson* [62] pioneered the use of a modified streak camera to generate 100-ps electron pulses to record diffraction images from thin aluminum films in transmission mode; they subsequently produced 20-ps electron pulses to study the phase transformation in these films before and after irradiation with a laser [63]. *Elsayed-Ali* and co-workers succeeded in using 200-ps (and later shorter) electron pulses to investigate surface melting with reflection high-energy electron diffraction (RHEED) [64][65].

In the field of ultrafast electron diffraction, for the studies of isolated structures *evolving with time*, the leap forward came from the use of digital processing with CCD cameras, generation of ultrashort electron packets using femtosecond lasers and high extraction fields, and *in situ* pulse sequencing and clocking – all of which gave us unprecedented levels of sensitivity and spatiotemporal resolution. Using these developments, we have studied a variety of complex molecular structures and resolved the temporal evolution of different classes of reactions, as discussed below. More recently, *Weber* and co-workers have succeeded in obtaining ultrafast diffraction images of cyclohexadiene [66], a system we have studied both theoretically and experimentally [35][38]. Theoretical analysis of the diffraction signatures of individual vibrational modes in polyatomic molecules prepared in a specific vibrational state was also reported [67][68].

This review highlights the progress made at Caltech: the conceptual foundations of UED (*Chapt. 2*), the evolution of our UED experimental apparatus over three generations, along with the issues central to achieving picosecond/sub-picosecond temporal resolution (*Chapt. 3*), and the rich scope of applications of UED (*Chapt. 4*). *Chapt. 5* concludes with a perspective on the field of ultrafast structure determination in general, and the direction of our UED research efforts, presently being realized in UED-4 for condensed matter and biological systems.

2. Principles of UED

2.1. Concepts

The UED technique employs properly timed sequences of ultrafast pulses – a femtosecond laser pulse to initiate the reaction and ultrashort electron pulses to probe the ensuing structural change in the molecular sample (*Fig. 1*). The resulting electron diffraction patterns are then recorded on a CCD camera. This sequence of pulses is repeated, timing the electron pulse to arrive before or after the laser pulse; in effect, a series of snapshots of the evolving molecular structure are taken. Each time-resolved diffraction pattern can then, *in principle*, be inverted to reveal the three-dimensional molecular structure that gave rise to the pattern at that specific time delay. However, *in practice*, a key challenge lies in recovering the molecular structural information that is embedded in the as-acquired diffraction images.

One of the most powerful features of electron diffraction is that the electrons scatter off all atoms and atom–atom pairs in the molecular sample. Thus, unlike spectroscopy wherein the probe is tuned to specific transitions in the molecule, the electron probe is sensitive to all species in its path and can hence uncover structures that spectroscopy may be blind to. However, it is this strength of UED that also poses a tremendous challenge in retrieving information on molecular structure change. The recorded electron diffraction patterns contain contributions from incoherent atomic scattering as well as the coherent molecular interferences arising from atom–atom pairs. Since there is no long-range order in gases to enhance coherent interferences, the incoherent atomic scattering from gases is orders of magnitude higher. Also, since the fraction of molecules undergoing change is small (typically 10% or less), the recorded diffraction patterns contain large contributions from unreacted molecules.

A key advance in accessing this small population of changing structures embedded in the large background signal has been the development of the Diffraction-Difference Method in our laboratory [31]. The method consists of timing the electron pulses so as to establish an *in situ* reference signal (usually the ground-state structure obtained at negative time). The digital nature of our processing methodology then allows us to obtain the difference of each time-resolved diffraction pattern from this reference signal, thus revealing the change from the reference structure in the form of difference rings (*Fig. 1*).

The diffraction-difference method has several general advantages. First, the large (unwanted) background signal from atomic scattering is a common contribution to all images – regardless of the temporal delay and the nature of the reaction – and can, therefore, be practically eliminated in the difference. Thus, whereas the total diffraction signal is dominated by the background intensity, the diffraction-difference curve is dominated by the molecular scattering intensity. Second, any intrinsic systematic error of the detection system will be effectively eliminated or greatly reduced by the difference. Third, each diffraction-difference image reflects comparable contributions from the reactant and transient structures – in contrast, in the original raw data, only a relatively small fraction of the signal comes from transient structures, with the vast majority of the signal originating from the unreacted parent. Therefore, the significance of transient structure contribution is dramatically enhanced in the diffraction-difference curves. Furthermore, because the diffraction-difference signal contains compa-

Ultrafast Electron Diffraction

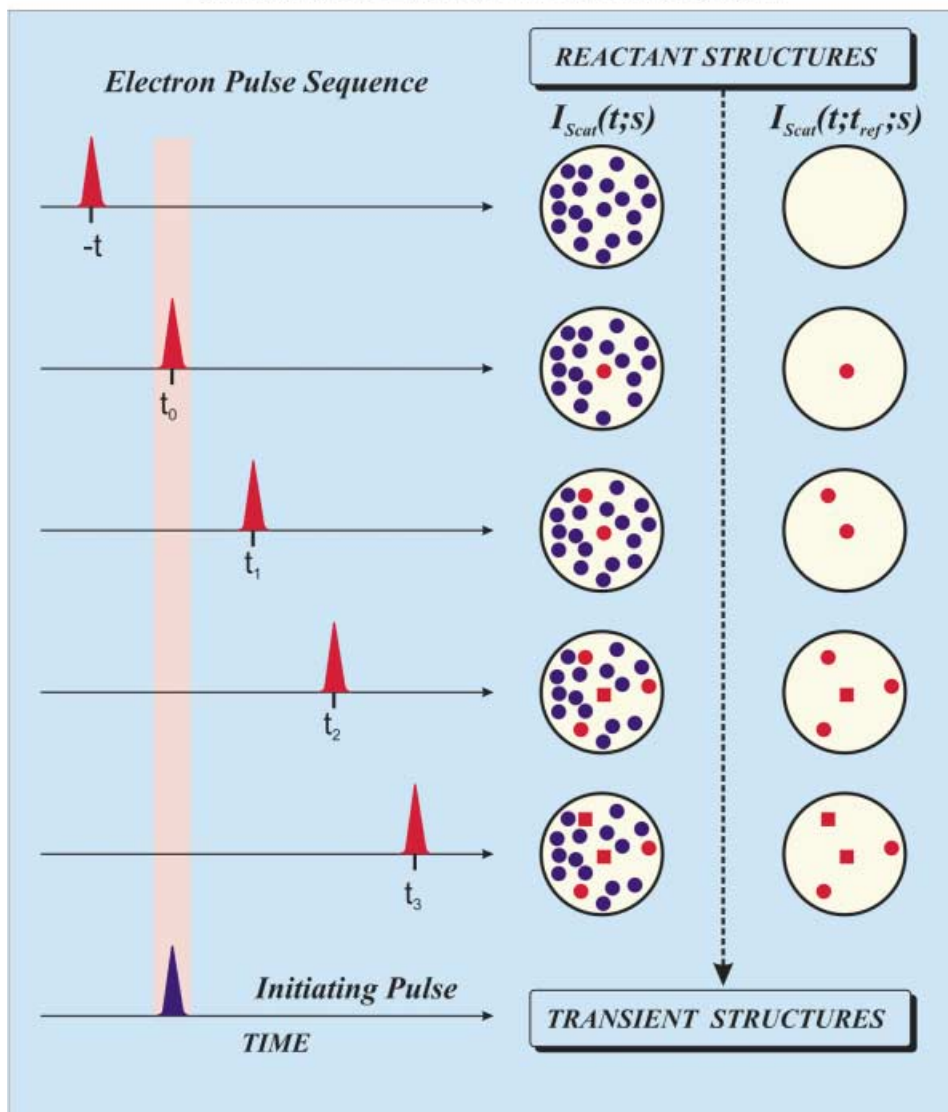


Fig. 1. The concept of Ultrafast Electron Diffraction (UED). An ultrafast initiation pulse (shown in blue) triggers the reaction, and a second ultrashort electron pulse (shown in red) probes the resulting structural change. The electron pulse can be timed to arrive before the initiating pulse (negative time) thus probing the parent (shown as blue filled circles) or after the laser pulse (positive time), now probing the transient structures also (shown as red filled circles and squares). The time at which the light and electron pulses arrive simultaneously at the molecular sample is the zero-of-time (t_0). With increasing time lapse after the initiation pulse, the transient species undergoes a population change (indicated by the growth of the red filled units at the expense of the blue filled circles), and a structural change (shown as the transformation of red circles into red squares). The difference of each time-resolved diffraction pattern from a reference pattern, t_{ref} (chosen at negative or at positive time), via the Diffraction-Difference Method allows the extraction of this small population of time-evolving structures embedded in the large background signal of unreacted parents. Note that this dramatically enhances the significance of the transient species contribution in the diffraction-difference patterns, $I_{Scat}(t; t_{ref}; s)$. The small residual contribution of unreacted parents to the diffraction-difference pattern is not shown here for sake of simplicity.

nable contributions from both parent and transient species, we can isolate the molecular diffraction signal resulting *only* from transient species – *via* the ‘transient-isolated’ or ‘transient-only’ method – wherein the parent diffraction signal (obtained at a negative time) is scaled by the fractional change and added to the diffraction-difference signals (obtained at positive times), thereby canceling out the parent contribution.

This development of the diffraction-difference methodology, combined with the large electron-scattering cross-section inherent in the UED experiment, provides the impetus for investigating diverse molecular phenomena with UED. However, to realize this potential of UED, several other conceptual challenges had to be surmounted. First, there had not previously been a way to determine *in situ* the zero-of-time in UED experiments. Second, for an ultrafast electron pulse, electron–electron repulsion takes place. These space–charge effects broaden the pulse duration over time, leading to a trade-off between temporal resolution and the electron pulse density. Third, the orders-of-magnitude lower density of gas-phase samples relative to solids and surfaces results in much weaker scattering intensities. Last, the limited extent of reaction requires unprecedented sensitivity in the number of molecules detected. These challenges in UED – the clocking of the change, the space–charge-limited temporal resolution of the electron pulse, the low densities in the gas phase, and the small number of molecules undergoing change – were major hurdles that had to be circumvented in order to reach the current state-of-the-art.

To clock the change on the picosecond/sub-picosecond time scale, we have developed an ion-induced ‘lensing’ method [29], as discussed below. To limit space–charge-induced broadening, the electron density in the ultrashort electron packets is maintained low; 1 ps electron pulses typically contain 1000 electrons. Consequently, the total scattering intensity is considerably lower when compared with conventional GED experiments. The orders-of-magnitude difference in the beam current of UED (pA) relative to conventional GED experiments (μA to mA) must be accounted for by the length of the exposure and the detector construction. Realistically, exposure times have an upper limit on the order of a few hours given that several diffraction patterns, with different time delays, are to be taken in one experiment. The key to overcoming the intensity deficit in UED is the introduction of a sensitive CCD capable of single-electron detection.

These challenges and our continuous efforts to enhance system performance by improvements in pulsed electron flux, repetition rate, detection sensitivity, and experimental stability have led to four generations of UED machines in this laboratory. Before discussing these in detail, we will first review the theory of gas-phase diffraction, in general, and the diffraction-difference method, in particular.

2.2. Theory

The general theory of GED is well-established [19]; here, we summarize the basic equations used in the analysis of scattering patterns and the subsequent extraction of internuclear separations. Electron scattering intensity is typically expressed as a function of s , the magnitude of momentum transfer between an incident electron and an elastically scattered electron:

$$s = \frac{4\pi}{\lambda} \sin\left(\frac{\theta}{2}\right) \quad (1)$$

where λ is the *de Broglie* wavelength of the electrons (0.067 Å at 30 keV) and θ is the scattering angle.

The total scattering intensity, I , is a sum of contributions from individual atoms (atomic scattering, I_A) superimposed with interference terms from all atom–atom pairs (molecular scattering, I_M):

$$I(s) = I_A(s) + I_M(s) \quad (2)$$

In the independent-atom model, where the independence of the electronic potentials of each atom in the molecule is assumed, the atomic scattering intensity can be written as a sum of elastic and inelastic scattering contributions:

$$I_A(s) = C \sum_{i=1}^N \left(|f_i(s)|^2 + 4 \frac{S_i(s)}{a_0^2 s^4} \right) \quad (3)$$

where N is the number of atoms in the molecule; f_i and S_i are the elastic and inelastic scattering amplitudes for atom i , respectively; a_0 is the *Bohr* radius; and C is a proportionality constant. The contributions from spin-flip scattering amplitudes (g_i) have not been included as they are generally neglected for high-energy electron diffraction experiments [69].

For the purpose of structural determination, only I_M is of interest because it contains the information regarding internuclear separations. The molecular scattering intensity of an isotropic sample can be written as a double sum over all N atoms in the molecule:

$$I_M(s) = C \sum_i^N \sum_{j \neq i}^N |f_i||f_j| \exp\left(-\frac{1}{2} l_{ij}^2 s^2\right) \cos(\eta_i - \eta_j) \frac{\sin(sr_{ij})}{sr_{ij}} \quad (4)$$

where f_i is the elastic scattering amplitude for the i th atom, η_i is the corresponding phase term, r_{ij} is the internuclear separation between atoms i and j , l_{ij} is the corresponding mean amplitude of vibration, and C is a proportionality constant. The atomic scattering factors f and η depend on s and atomic number Z ; tables of f and η are available in the literature [70] with f scaling as Z/s^2 (*Rutherford* scattering). The relative contribution of each atomic pair to the total molecular scattering intensity (from Eqn. 4) is, therefore, roughly proportional to $(Z_i Z_j)/r_{ij}$. Since $I_M(s)$ decays approximately as s^{-5} , the modified molecular scattering intensity, $sM(s)$, is often used instead of $I_M(s)$ in order to highlight the oscillatory behavior ($\sin(sr_{ij})/r_{ij}$) of the diffraction signal at higher values of s ; note that the $\sim s^{-5}$ dependence arises from the s^{-2} contribution from f_i and similarly from f_j , along with the $1/s$ term of the sinc function, which results from isotropic averaging in the gas sample. The modified molecular scattering intensity can be defined either as:

$$sM(s) = s \frac{I_M(s)}{I_A(s)} \quad (5a)$$

or

$$sM(s) = s \frac{I_M(s)}{|f_a||f_b|} \quad (5b)$$

where a and b correspond to two chosen atoms in the molecule (usually atoms with relatively high Z). Note that the experimental $I_M^E(s)$ can be transformed into $sM^E(s)$ by simply dividing by an atomic reference signal (xenon gas, in our case) and multiplying by s (obtained from measured θ through the known camera length).

Although the molecular scattering function contains all of the structural information about the molecule, a more intuitive interpretation of experimental results is achieved by taking the *Fourier* (sine) transform of $sM(s)$ and examining $f(r)$, the radial distribution function.

$$f(r) = \int_0^{s_{\max}} sM(s) \sin(sr) \exp(-ks^2) ds \quad (6)$$

where k is a damping constant. The exponential damping term filters out the artificial high frequency oscillations in $f(r)$ caused by the cutoff at s_{\max} . The radial distribution curve reflects the relative density of internuclear distances in the molecule. In our UED-3 experiments, the available experimental scattering intensity, $sM^E(s)$, typically ranges from $s_{\min} = 1.5 \text{ \AA}^{-1}$ to $s_{\max} = 18.5 \text{ \AA}^{-1}$ (θ from 0.9° to 11.3°). For the range from 0 to s_{\min} , the theoretical scattering intensity, $sM^T(s)$, is appended to avoid distortions of the radial distribution baseline. It should be noted that all data analyses and structural refinements are performed on $sM^E(s)$ and not $f(r)$ because of inaccuracies that could potentially be introduced into $f(r)$ through improper choice of k .

2.3. The Diffraction-Difference Method – Transient Structures

To follow the structural changes that occur over the course of a given reaction, a series of averaged 2D diffraction images are recorded – with varying time delay, t . Before analyzing the time-dependent diffraction signals, we normalize the intensity of each time-dependent 2D image to the total number of electrons detected on the CCD. This normalization procedure accounts for any systematic variation (1% or less) in electron scattering intensity as a function of temporal delay. Each of these normalized, averaged images, thus, reflects the transient behavior of the molecular structures at a particular temporal delay following excitation. Unlike the ground-state data, the scattering intensity at time $t > 0$, $I(t > 0; s)$, contains contributions from more than one type of molecular species – not just the reactant structures, but also the transient, intermediate, and product structures of the reaction.

Structural dynamics of a species involves two important changes: *population* change and *structural* change. Consider the following reaction:



where there is a change of species from reactant (S_R) through intermediate (S_I) to product (S_P). A species is defined as a molecular entity with a particular chemical formula. The time-resolved scattering intensity $I(t; s)$ can be written as a sum of the individual scattering intensities from each species, $I_\alpha(t; s)$, at time t :

$$I(t; s) = \sum_\alpha I_\alpha(t; s) = \sum_\alpha p_\alpha(t) \cdot \sigma_\alpha(t; s) \quad (8)$$

where α indexes all possible species (reactant, intermediate, or product) occurring over the course of the reaction, $p_\alpha(t)$ is the normalized probability, henceforth referred to as the population of a given species α , and $\sigma_\alpha(t; s)$ is the effective scattering cross-section from that species. Depending on the time resolution of the diffraction experiment, we can resolve either the temporal change in species population, $p_\alpha(t)$, or the temporal change in species structure – manifested as a change in the effective scattering cross-section, $\sigma_\alpha(t; s)$ – or both.

In UED, all species present will scatter the incident electrons regardless of their participation in the reaction. Thus, in most cases, the vast majority (> 85–90%) of the diffracting media is comprised of non-reacting parent molecules: $p_{\text{reactant}} \gg p_{\text{intermediate}}$ or p_{product} . Furthermore, the molecular scattering intensity from a reaction fragment is usually weaker than that from the parent molecule because it has fewer internuclear pairs. Therefore, to accentuate the diffraction signal arising from structural changes occurring over the course of the reaction, we employ the diffraction-difference method [31], wherein we use a reference image to obtain the diffraction-difference signal, $\Delta I(t; t_{\text{ref}}; s)$, from the relation

$$\Delta I(t; t_{\text{ref}}; s) = I(t; s) - I(t_{\text{ref}}; s) \quad (9)$$

where t_{ref} refers to the reference time (*e.g.*, prior to the arrival of the reaction-initiating laser pulse). Combining *Eqns.* 8 and 9 gives

$$\Delta I(t; t_{\text{ref}}; s) = \sum_{\alpha} p_{\alpha}(t) \cdot \sigma_{\alpha}(t; s) - \sum_{\alpha} p_{\alpha}(t_{\text{ref}}) \cdot \sigma_{\alpha}(t_{\text{ref}}; s) \quad (10)$$

The experimental diffraction intensity curve is a sum of the desired structural information, $I_{\text{M}}^E(s)$, and a background intensity profile, $I_{\text{B}}^E(s)$:

$$I^E(s) = I_{\text{B}}^E(s) + I_{\text{M}}^E(s) \quad (11)$$

where $I_{\text{B}}^E(s)$ contains contributions from atomic scattering, $I_{\text{A}}(s)$, and the experimental background response. It follows from this definition that the experimental difference curve is given by

$$\Delta I^E(t; t_{\text{ref}}; s) = \Delta I_{\text{M}}^E(t; t_{\text{ref}}; s) + \Delta I_{\text{B}}^E(t; t_{\text{ref}}; s) \quad (12)$$

Because I_{B}^E is comprised mostly of atomic scattering, which is unchanged over the course of a chemical reaction, $\Delta I_{\text{B}}^E(t; t_{\text{ref}}; s)$ should be nearly zero. Thus, whereas the total diffraction signal, $I(t; s)$, is dominated by the background intensity, $I_{\text{B}}^E(t; s)$, the diffraction-difference curve is dominated by the molecular scattering intensity, $I_{\text{M}}^E(t; s)$:

$$\Delta I^E(t; t_{\text{ref}}; s) \approx \Delta I_{\text{M}}^E(t; t_{\text{ref}}; s) \quad (13)$$

Thus, *Eqn. 13*, which is a direct consequence of the diffraction-difference approach, allows us to obtain transient molecular structures even if their population is small relative to the unchanging background (*Fig. 1*). It may be noted that the diffraction-difference method does not depend on the specific formulae used to express I_{M} . While

the well-known description, Eqn. 4, is usually used, formulae more sophisticated than Eqn. 4 have been used in our UED studies.

One of the most important features of the diffraction-difference method is the control over t_{ref} . The choice of t_{ref} – the sequence of the electron pulses – allows us to isolate structures of different species evolving with time:

1) By choosing t_{ref} to be at negative time, we can obtain the ground-state diffraction pattern. Also, by recording diffraction images at two different negative times (probing the same reactant structure at each of these times), we can obtain a control diffraction-difference image to verify the absence of rings.

2) By choosing t_{ref} to be at a specific positive time, we can isolate different transient species in, say, non-concerted reactions based on the relevant timescales of the non-concerted bond breaking, as described below for the case of $\text{C}_2\text{F}_4\text{I}_2$ in Sect. 4.2.

3) Finally, we can also extract the molecular diffraction signal resulting only from the transient species via the ‘transient-only’ or the ‘transient-isolated’ method. In this case, the reactant diffraction signal ($I_{\text{reactant}}(s)$, obtained at a negative time) is scaled by the fractional change, $\Delta p_{\text{reactant}}(t; t_{\text{ref}})$, and added to the diffraction difference signals obtained at positive times, thereby canceling out the parent contribution:

$$\Delta I(t; t_{\text{ref}}; s) + \Delta p_{\text{reactant}}(t; t_{\text{ref}}) \cdot I_{\text{reactant}}(s) = \sum_{\alpha \neq \text{reactant}} \Delta p_{\alpha}(t; t_{\text{ref}}) \cdot \sigma_{\alpha}(t; s) \quad (14)$$

2.4. Ground-State Structures

Ground-state diffraction patterns are obtained by timing the electron pulse to arrive at the molecular sample before the laser pulse (negative time; see Fig. 1) or by completely blocking the laser arm (to reduce the noise due to laser light). From Eqn. 5, the modified experimental molecular scattering intensity of the ground-state is given by

$$sM^E(s) = s \frac{I^E(s) - I_{\text{B}}^E(s)}{I_{\text{A}}(s)} \quad (15a)$$

or

$$sM^E(s) = s \frac{I^E(s) - I_{\text{B}}^E(s)}{|f_{\text{a}}||f_{\text{b}}|} \quad (15b)$$

We do not obtain the curve for $I_{\text{B}}^E(s)$ by merely calibrating the detector because the amount of scattered laser light and other factors vary from experiment to experiment and with each molecular system. Instead, background curves are independently obtained for each experiment. Such background curves may be ascertained by different methods, three of which are described: 1) A crude yet often effective approximation is a low-order polynomial curve fit through all the data points of $I^E(s)$; 2) A more rigorous way of obtaining $I_{\text{B}}^E(s)$ exploits the sinusoidal nature of $I_{\text{M}}(s)$, cycling above and below zero several times over the experimental detection range. This approach introduces a set of zero-positions, s_n , of s where the theoretical molecular intensity curve, $I_{\text{M}}^T(s)$, crosses zero, *i.e.*, $I_{\text{M}}^T(s_n) = 0$. If $I_{\text{M}}^T(s)$ approaches $I_{\text{M}}^E(s)$, it should then hold from Eqn. 2 that $I^E(s_n) = I_{\text{B}}^E(s_n)$ at the zero-positions, s_n . Therefore, $I_{\text{B}}^E(s)$ can be approximated by

fitting a polynomial curve through $[s_n, I^E(s_n)]$; 3) A third way to obtain $I_B^E(s)$ is to express $I_B^E(s)$ independently as a polynomial curve defined by the variable coefficients of each order, and to optimize these variables by minimizing the difference (more precisely, χ^2) between $I_M^T(s)$ and $I_M^E(s)$. This method should produce the same background curve obtained with the second method if there is no systematic error. The three methods can also be applied to the time-resolved diffraction data. Currently, method 3) as described above is the method of choice in UED-3.

2.5. Structure Search and Refinement

UED utilizes quantum-chemical calculations as a starting point for the global conformational search. In UED-3, the structure parameters are constructed with internal coordinates of a geometrically consistent structural model for the molecule – the so-called *Z*-matrix of quantum chemistry – to facilitate easier comparison between theory and experiment. To ensure that all possible structures are considered in the refinements, Monte Carlo sampling procedures are applied to search all possible good fits to the data (in terms of χ^2) in a configuration space set up by the *Z*-matrix coordinates. The distance between any two given structures is defined as the square root of the sum of the squared displacements between all corresponding nuclear coordinates of the two structures. Based on the distance between randomly sampled structures to a starting structure, the configuration hyperspace is first partitioned and then searched for local minima. When the sampling within the partitioned subspace is found to converge to a local χ^2 minimum, the radius of convergence is determined along each adjustable internal coordinate to give the size of local minimum basin. Finally, lowest-local-minima structures are statistically analyzed to reveal the ensemble distribution of a global minimum structure. The Monte Carlo sampling algorithm, coupled with the internal coordinate representation, allows the fit structure to be vastly different from the starting model provided by quantum calculations. This forms the basis of the UED-3 structural search in large conformational space guided by experiment.

Refinement of the diffraction data is performed with software developed in our laboratory at Caltech using a procedure that iteratively minimizes the statistical χ^2 . For example, for a given difference curve, $\Delta I^E(t; t_{\text{ref}}; s)$, the determination of the relative fractions or structural parameters of each molecular species is made by minimizing

$$\chi^2 = \sum_{s_{\text{min}}}^{s_{\text{max}}} \frac{[S_c \cdot \Delta s M^T(t; t_{\text{ref}}; s) - \Delta s M^E(t; t_{\text{ref}}; s)]^2}{[\delta(s)]^2} \quad (16)$$

where the $\Delta s M(s)$ is the difference-modified molecular-scattering intensity, $\delta(s)$ is the standard deviation of $\Delta s M^E(t; t_{\text{ref}}; s)$ at each s position (over the available range), and S_c is a scaling factor (whose magnitude is determined by the amplitude of the ground-state signal). $\Delta s M^E(t; t_{\text{ref}}; s)$ is obtained from $\Delta I^E(t; t_{\text{ref}}; s)$ by *Eqn. 15*, and the $\delta(s)$ values are calculated from the corresponding values of $\delta(\text{pix})$ (the standard deviation of the scattering intensity at each pixel radius) with appropriate error propagation.

Beginning with an assumed initial species distribution and the starting structural parameters for each species, the software first fits the residual background, $\Delta I_{\text{B}}^E(t; t_{\text{ref}}; s)$, as a polynomial curve by optimizing the variable coefficients in order to minimize the difference (more precisely, χ^2) between $I_{\text{M}}^T(s)$ and $I_{\text{M}}^E(s)$. Then, the experimental $\Delta sM^E(t; t_{\text{ref}}; s)$ curve is obtained with the background-free ΔI by Eqn. 15, and χ^2 is calculated to evaluate the quality of the fit. This procedure is repeated until the best least-squares fit between theoretical and experimental $\Delta sM(s)$ curves is reached (*i.e.*, until χ^2 is minimized).

3. Generations of UED

3.1. Instrumentation

Ultrafast electron diffraction combines several disparate fields of study: femtosecond pulse generation, electron beam optics, CCD detection systems, and GED. Output from a femtosecond laser is split into a pump path and an electron-generation path. The pump laser proceeds directly into the vacuum chamber and excites a beam of molecules. The probe laser is directed toward a back-illuminated photocathode, where the laser generates electron pulses *via* the photoelectric effect; the electrons are accelerated, collimated, focused, and scattered by the isolated molecules (*Fig. 2*). The time delay between the arrival of the pump laser pulse and the probe electron pulse is controlled with a computer-driven translation stage. The resulting diffraction patterns are detected with a CCD camera, and the images are stored on a computer for later analysis. The UED-3 apparatus (*Fig. 3*) is also equipped with a time-of-flight mass spectrometer (MS-TOF) to aid in the identification of species generated during the course of chemical reactions. The following sections describe the individual components of the apparatus in more detail.

3.1.1. *Femtosecond Laser System.* The laser system can be divided into three stages: 1) ultrashort pulse generation, 2) pulse amplification, and 3) wavelength selection. In the first and second generations of UED, femtosecond laser pulses centered at 620 nm were generated with a home-built colliding-pulse, mode-locked ring dye laser (CPM) similar to the original system built for femtochemistry studies [3]. Output from the CPM (100 MHz, 200 pJ) was amplified to 2 mJ in a 30-Hz, homebuilt, four-stage, NdYAG-pumped dye amplifier (PDA). The pump wavelength was either maintained at 620 nm or converted to 310 nm through second harmonic generation with a KD*P crystal. A wavelength of 258 nm was required to create photoelectrons from the gold photocathode. Therefore, part of the pump laser was focused into a quartz crystal to generate continuum, and 516 nm was selected with a 10-nm bandpass filter. The energy of these pulses was then boosted to microjoules in a two-state, transversely-pumped dye amplifier. The amplified output was frequency-doubled with a BBO crystal to form ultraviolet light at 258 nm, and the final laser output was focused and directed toward the photocathode.

In UED-3, femtosecond laser pulses (82 MHz, 8 nJ) centered at 800 nm are generated with a Ti:sapphire oscillator (*Tsunami, Spectra-Physics*). These pulses are then amplified in a 1-kHz two-stage Ti:sapphire amplifier (*SuperSpitfire, Spectra-Physics*) to yield an output pulse energy of 3 mJ. Both stages are pumped by 1-kHz

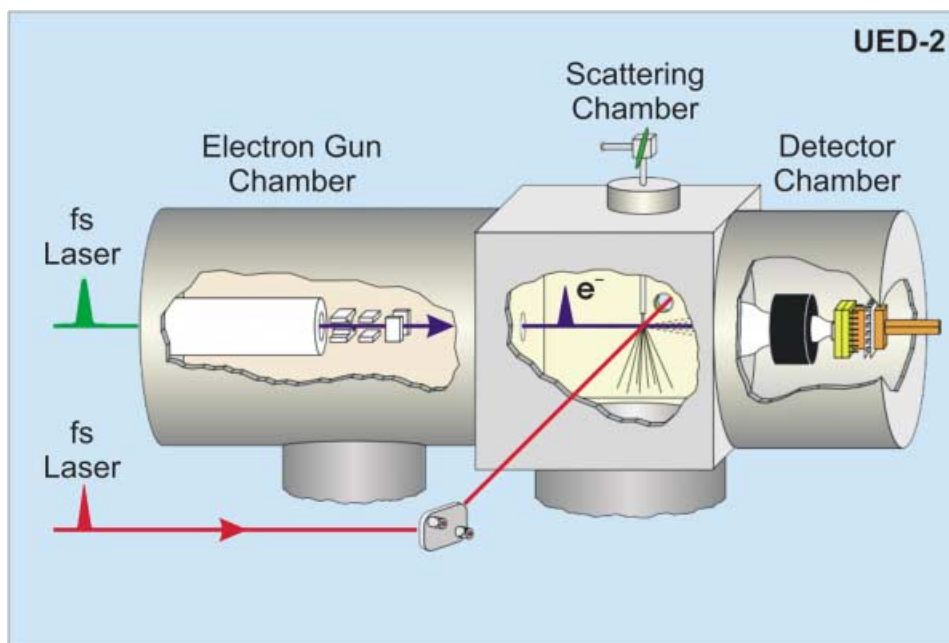


Fig. 2. Second-generation UED-2 apparatus schematic, consisting of an electron gun chamber, a scattering chamber, and a detector chamber

intra-cavity doubled Nd:YLF lasers (*Merlin, Spectra-Physics*). Single-shot autocorrelation of the amplified pulses yields a pulse duration full-width at half-maximum (*fwhm*) of 120 fs. These pulses are frequency-tripled in a femtosecond third-harmonic generator (*Uniwave Technology*) to give UV femtosecond pulses (350 μ J, 267 nm). An optical beam splitter is used to split this UV output into two arms to form the pump beam and the electron generation beam. Most (90%) of the UV beam is directed into the scattering chamber to initiate the chemical reaction, whereas a smaller fraction of the laser power is directed into a delay line with a computer-controlled translation stage, and then focused onto the photocathode in the electron gun.

3.1.2. *Vacuum Chambers and Molecular Beams*. The first-generation UED apparatus housed the electron gun, molecular beam, and the CCD detector in the same chamber. However, the electron gun was prone to arcing if the background pressure rose much above 1×10^{-4} Torr, and on at least one occasion, an electrical arc was strong enough to destroy a CCD. Keeping the electron gun clean and free from arcing was the motivation for introducing differential pumping in the second-generation apparatus (*Fig. 2*), so that the electron-gun-chamber pressure could be kept below 1×10^{-6} Torr even while running sample gas in the scattering chamber at 1×10^{-4} Torr or higher.

The UED-3 apparatus (*Fig. 3*) consists of four separate vacuum chambers – the electron gun, the scattering chamber, the detection chamber and the time-of-flight mass spectrometry chamber – in order to protect sensitive instruments from potentially corrosive sample molecules. Pressures below 1×10^{-7} Torr are attained in the scattering

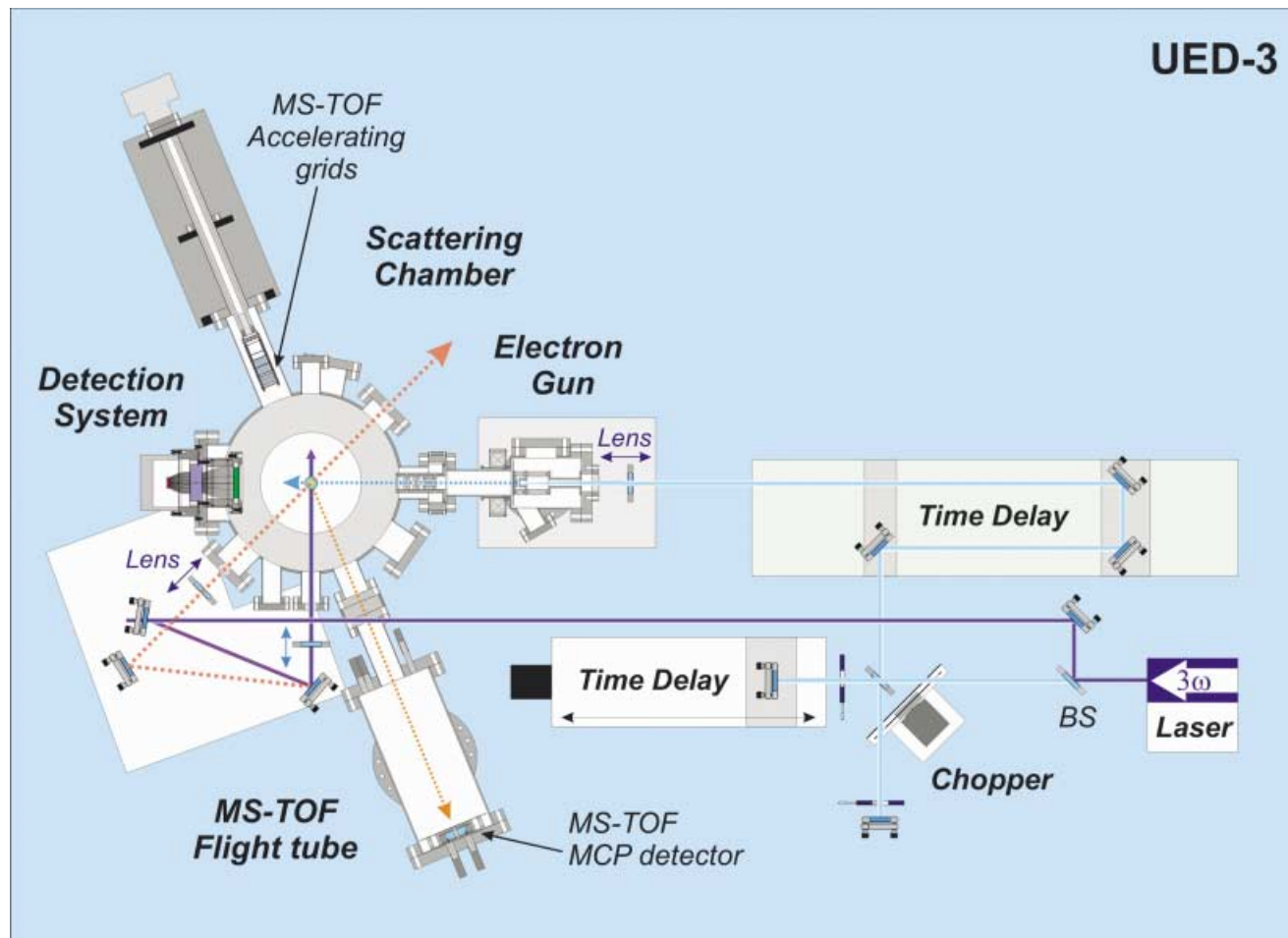


Fig. 3. Third-generation UED-3 apparatus schematic, with the time-of-flight mass spectrometer (MS-TOF)

chamber in the absence of the molecular beam and are as high as 10^{-4} Torr when the molecular beam is operating. The pressure in the detection chamber is kept at 10^{-2} Torr to avoid condensation on thermoelectrically cooled surfaces. In an effort to minimize scattered light, the laser pulses enter the scattering chamber through a series of baffles attached to the light entrance port and exit through a *Wood's* horn sealed by a quartz window at *Brewster's* angle. Care is taken to avoid any stray electric or magnetic fields that might distort the path of the scattered electrons.

The sample molecules enter the vacuum chamber in a free-jet expansion through a 125- μm diameter needle tip; the sample inlet manifold being mounted on a high-precision *xyz* positioning stage. The needle and inlet tube are wrapped with a resistive heating element to prevent condensation and clogging, while the sample bulb is warmed with heating tapes to provide sufficient vapor pressure of less volatile samples inside the chamber.

3.1.3. *Electron Gun.* In UED-3, the cylindrically symmetric gun consists of a negatively-biased photocathode, a gold extraction mesh, an aperture, and a magnetic focusing lens. The electron gun, powered by a variable high-voltage power supply, is designed to operate at 30 kV (compared to 18 kV in UED-2). The photocathode is back-illuminated in this design: a thin, 450- \AA silver film was deposited on one side of a sapphire window using a home-built metal evaporation chamber. A grounded gold extraction mesh, located 5 mm from the cathode surface, provides a very high extraction field of 6 kV/mm (compared to 2.7 kV/mm in UED-2). The extracted electrons are then sent through a Pt:Ir aperture (150- μm diameter), which assists in cleaning the electron beam profile. In UED-2, a series of electrostatic lenses focused the electron beam by reducing the electron velocity over a region of several centimeters. However, replacing the electrostatic lens by a magnetic lens assembly in UED-3 successfully avoids this velocity reduction so that the electron velocity remains large and constant after the initial extraction, thereby reducing the transit time to the interaction region and concomitantly reducing the broadening of the electron pulse. Temporal characterization of the electron gun *via* a streak experiment is discussed in Sect. 3.2. Two pairs of deflection plates provide *x* and *y* axis control of the electron beam, while a third pair of aluminum plates is used for streak measurements.

3.1.4. *CCD Camera System.* A component critical to the success of UED is the detection system. The electron flux has to be maintained very low in order to keep the temporal resolution ultrafast. Early on, we recognized that all of the scattered electrons must be detected for the experiment to succeed, and we introduced the two-dimensional CCD as a detector in direct electron bombardment mode in UED-1. To increase the longevity and flexibility of the detection system, UED-2 employed two CCDs: a small, direct-bombardment device installed in the scattering chamber for time-zero measurements, and another large, scientific-grade device mounted in a separate chamber at the end of a phosphor scintillator/fiber optic/image intensifier chain for recording diffraction patterns (*Fig. 4*).

In UED-3, we designed an improved low-noise, two-dimensional CCD camera assembly with the same elements as in *Fig. 4*, but without the small CCD. The camera has high detective quantum efficiency and principally comprises a phosphor scintillator (*P-47*), a fiber optic taper, a proximity-focused image intensifier (*Hamamatsu*), and finally the scientific-grade CCD camera (*Photometrics, KAF-1000*). Because the

UED Detection System

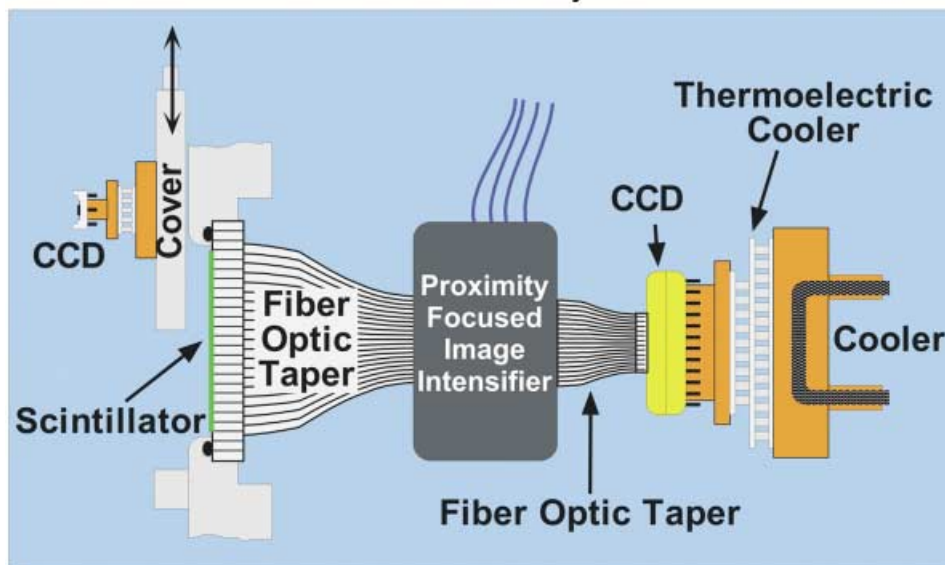


Fig. 4. *Detection system for UED.* Incident electrons either directly bombard a small CCD or strike a phosphor-coated fused fiber-optic window. Light emitted from the phosphor is amplified by an image intensifier and brought to a scientific-grade CCD (see text).

scattering intensity in electron diffraction decays rapidly with increasing scattering angle (usually varying over 6–8 orders of magnitude), we introduced a radially symmetric, variable neutral-density apodizing optical filter coated onto the backside of the scintillator – the rotating sector analog in our digital detection system, albeit with no mechanical moving parts. This filter allows the simultaneous measurement of diffracted intensities varying over 7 orders of magnitude, thereby effectively extending the dynamic range of detected intensities and consequently improving the precision of internuclear distance measurements in comparison with previous generations of UED. To block the scattered light and yet still permit single-electron detection, the phosphor screen is coated with 500-nm of aluminum.

The CCD chip consists of an array of 1024 by 1024 individual pixel elements (compared to 512 by 512 pixels in UED-2), each pixel being 24 μm on a side. The scattered electrons impinge upon a phosphor screen, thereby generating photons that are then transferred *via* a fiber-optic taper to a proximity-focused image intensifier (Fig. 4). The photons are reconverted back to electrons at the photocathode on the front end of the image intensifier; the resulting electron signal is amplified and then reconverted back to photons at the back end of the intensifier. These photons are then transferred *via* a second fiber-optic taper onto the CCD chip.

Experiments showed that a single electron generates 20–30 counts, and saturation occurs above 65535 counts. The response of the CCD is linear over this range. The undiffracted beam, containing 99% of the electron intensity over a small area, is trapped by an aluminum beam stop mounted in front of the phosphor screen, in order

to prevent damage. To enhance low-light sensitivity by reducing dark current, the CCD is cooled to -40°C by a three-stage thermoelectric cooler, which is coupled to a liquid circulation heat exchanger to draw heat away from the thermoelectric cooler. The CCD chip is controlled with a camera electronics unit and a computer-driven digital imaging system (*Roper Scientific, V++*). The analog–digital conversion process operates with 16-bit resolution, and the readout rate is kept at 200 kHz to minimize digital noise. At this rate, a 512×512 pixel image (obtained by operating the CCD in 2×2 binning mode) requires *ca.* 1 s for readout. The images are stored on a computer for subsequent data analysis. A typical experiment involves recording 1000 frames per second (kHz repetition rate) on the CCD over 240 s to give a single image that is readout in 1 s; *ca.* 100 such images are then averaged to produce the diffraction pattern at a specific time delay. The digital nature of our data acquisition permits the use of a variety of powerful image processing techniques that aid in the isolation of molecular diffraction signals, as detailed in [41].

3.2. UED Methodology

The total temporal resolution of UED, Δt_{total} , depends on the durations of the pump pulse ($\Delta t_{\text{p-laser}}$) and electron pulses ($\Delta t_{\text{electron}}$) and on temporal broadening caused by velocity mismatch between photons and electrons (Δt_{VM}) [71]:

$$\Delta t_{\text{total}}^2 = \Delta t_{\text{p-laser}}^2 + \Delta t_{\text{electron}}^2 + \Delta t_{\text{VM}}^2 \quad (17)$$

Eqn. 17 is based on the assumption that the laser and electron beams have Gaussian spatial and temporal profiles and that the density profile of the molecular beam cross-section is Gaussian. The *fwhm* of the pump laser pulse ($\Delta t_{\text{p-laser}}$) is 120 fs, which is smaller than the contributions from the other two terms. Consequently, the laser pulse contribution to the total experimental temporal resolution is relatively small, and this section will focus primarily on the duration of the electron pulse and the impact of velocity mismatch.

3.2.1. *Streaking: Electron Pulse Characterization.* Several different factors contribute to temporal broadening in the formation of short electron pulses, and these factors have been extensively examined in the streak camera literature. The total *streak camera* resolution, Δt_{R} , is often defined as a function of three different pulse-broadening sources [71]:

$$\Delta t_{\text{R}}^2 = \Delta t_{\text{e-laser}}^2 + \Delta t_{\text{D}}^2 + \Delta t_{\text{S}}^2 \quad (18)$$

where $\Delta t_{\text{e-laser}}$ is the temporal duration of the laser pulse, which creates the photoelectrons, Δt_{D} is the broadening of the electron pulse from its generation until it strikes the detector, and Δt_{S} is related to the detector geometry and spatial resolution. *Eqn. 18* is based on the assumption that the electron pulses have a Gaussian temporal distribution. The first term of *Eqn. 18* corresponds to the temporal *fwhm* of the laser pulse, in this case 120 fs. The second term in *Eqn. 18*, Δt_{D} , represents broadening of the electron pulse as it travels from the photocathode to the detector. The broadening of the electron pulse can be classified into three regimes: initial broadening at the

photocathode caused by the angular and energetic spread of the ejected photoelectrons; subsequent broadening of the pulse in the region of high electron density between the photocathode and anode due to space–charge effects; and broadening over the rest of the travel distance mainly due to non-uniform electron velocity distribution. For our current time resolution of 1 ps, the initial temporal broadening and the space–charge effects dominate the pulse broadening.

The initial temporal broadening of the photoelectrons is given by [72]

$$\Delta t_{\text{D(initial)}} = \frac{\sqrt{2m_e \Delta \varepsilon}}{eE_{\text{PC}}} \quad (19)$$

where $\Delta \varepsilon$ is the *fwhm* of the ejected photoelectron energy distribution, e is the electron charge, m_e is the electron mass, and E_{PC} is the electric field near the photocathode. Both E_{PC} and $\Delta \varepsilon$ may be controlled experimentally. The energy distribution, $\Delta \varepsilon$, which is related to the amount of excess energy in the photoemission process, can be minimized by proper selection of the photocathode material (hence its work function) and the incident laser wavelength. We have chosen to work with thin (*ca.* 450 Å) silver photocathodes which have proved durable under our operating conditions and are easy to prepare. With a work function of 3.65 eV reported for a 450-Å Ag film [73], barring thermal effects and surface contamination, the photoelectron energy distribution is expected to be narrow (*ca.* 0.6 eV for a one-photon and *ca.* 2.5 eV for a two-photon emission process [71]); note that the energy distribution of the laser pulse is only ~ 0.1 eV. *Eqn. 19* shows that the initial temporal broadening also depends on the electric field E_{PC} between the photocathode and the extraction mesh. Our present electron gun design sets $E_{\text{PC}} = 6$ kV/mm, which is similar to that used in state-of-the-art streak cameras. Under these conditions, we estimate $\Delta t_{\text{D(initial)}}$ to be *ca.* 350 to 900 fs.

Once the electrons are extracted, the pulse undergoes collimation and deflection until it strikes the detector. From the instant the electrons are generated, electron–electron Coulombic repulsion causes pulse broadening, and the effects of this repulsion on the spatial and temporal characteristics of an electron pulse have been collectively called the space–charge effect. The influence of space–charge effects on temporal broadening can be understood by considering electrons at the front and back of an electron pulse. The front electrons are accelerated forward by repulsion from the electrons behind them, while the trailing electrons are decelerated by the charges in front. The net result is that the entire pulse broadens in all directions over time. Due to the inverse-square dependence of Coulombic repulsion on distance, space–charge effects are very sensitive to the electron density of the pulse and are greatly reduced when the electron density is low. One method for reducing the broadening is to accelerate the electrons to a high velocity within a very short distance; not only does this spread the electron pulse out over a greater distance but it also reduces the time during which the electron pulse may broaden before intersecting the molecular beam or striking the detector. To reach sub-picosecond performance, the electron density must be reduced by limiting the number of electrons per pulse, which means that successful electron diffraction experiments require a high quantum efficiency detector such as a specially designed CCD camera.

The third term in *Eqn. 18*, Δt_s , contains broadening effects due to the detector. This *does not* reflect the temporal response of the detector itself, but rather how the spatial resolution and the position of the detector (with respect to the electron gun) influence streak measurements. When recording electron diffraction patterns, the electrons are not streaked, and, therefore, Δt_s does not apply to the UED experimental time resolution. We must, however, consider Δt_s when conducting streak experiments to measure the electron pulse length.

In the measurement of electron-pulse durations with streaking techniques, a time-dependent electric field is ramped across the first deflector pair such that an electron pulse traveling between the plates experiences a dispersive effect. Very fast rates of voltage change ($\partial V/\partial t$) are required to disperse single picosecond pulses. To synchronize the arrival of the electron pulse with the maximum voltage gradient ($\partial V/\partial t$) at the streaking plates, an optical delay line was constructed to control the firing time of the photoconductive switch. Of the two optical arms, one is directed toward the switch and the other toward the photocathode on the electron gun. The arm leading to the electron gun incorporates a *Michelson* interferometer to generate laser pulse pairs with a well-defined pulse separation Δt_{sp} ; Δt_{sp} is adjusted with a second optical delay. This laser pulse pair generates a pair of electron pulses with the same time separation Δt_{sp} at the photocathode.

After streaking, the two electron pulses are separated by a distance D_{pix} (in pixels) on the CCD detector. The streak velocity, in pixels per ps, is calculated from Δt_{sp} and D_{pix} . Single-shot streak image pairs are typically taken for a wide range of laser intensities, in order to observe the effect of current density on the electron pulse length. By measuring the center position of each electron pulse on the CCD, the streak speed is readily calculated in units of pixels per picosecond. The pulse width of each electron pulse is then calculated by dividing the spatial *fwhm* of the pulse (pix) by the streak speed (pix/s).

A typical set of low-intensity electron pulse pairs obtained in UED-3 is shown in *Fig. 5*. After analyzing such pulse pairs, we obtain a curve that describes the temporal behavior of the electron gun as a function of the number of generated electrons (*Fig. 6*). It is clear from this curve that there is little or no broadening by space-charge effects at low number of electrons. Moreover, *Fig. 6* also highlights the dramatic improvement in the electron gun performance in UED-3 as compared to UED-2 – a 5-ps pulse in UED-2 contained only 3000 electrons, while in UED-3, an electron pulse of the same width contains nearly 100,000 electrons.

3.2.2. Clocking: Zero of Time. In a UED experiment, the time coordinate for a reaction can only be established if there is a point of reference for the relative time delay between the initiation pulse and the electron pulse. This reference point is called time-zero (t_0), the time when both pulses simultaneously intersect in the sample. Careful measurement of laser and electron beam paths can narrow the time-zero window to within 100 ps. Another approach is to rely on the changes in the diffraction pattern of the system under investigation, but this is not an independent means of finding t_0 . More importantly, this method is simply not practical for gas-phase work because of the long integration times required to obtain a single data point.

In the clocking technique developed for UED [30], we use the crossed-beam geometry of the actual diffraction experiment to determine time-zero *via* the ‘lensing effect’. During CF_3I dissociation reaction studies [29], we observed a dramatic change

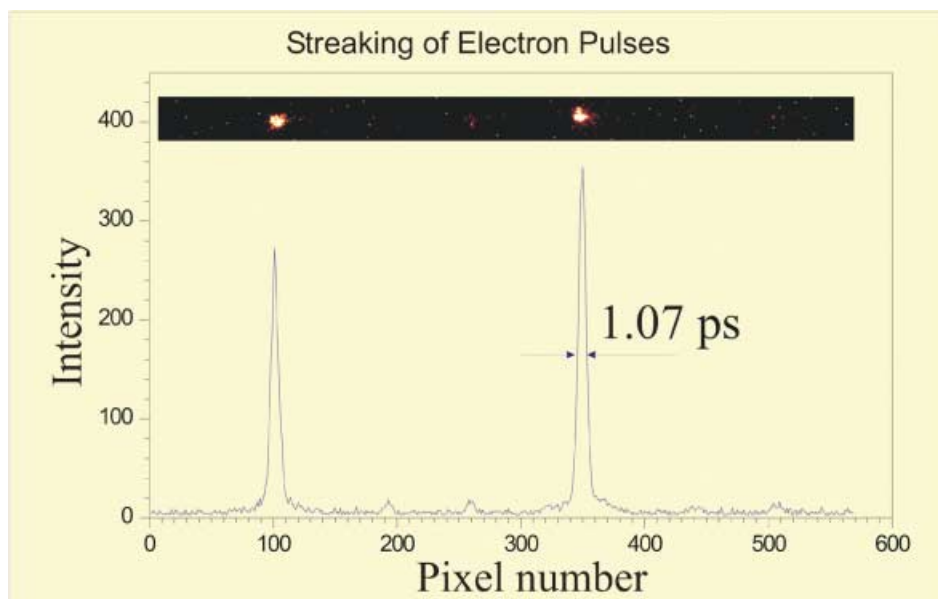


Fig. 5. Results of an in situ streaking experiment showing the ultrafast precision for electron pulse measurement in UED-3. The images of the streaked electron pulses separated by 50 ps are shown above the peaks of their respective profiles.

in the undiffracted electron beam profile when the excitation laser was present. The beam spot intensified along one axis, with a corresponding subtle decrease in the overall width. This effect only occurred when both the excitation laser and the molecular beam were present. The intensified strip was parallel to the laser axis and could be shifted up and down within the beam spot by adjusting the vertical tilt of the excitation laser entrance lens. Defocusing the laser reduced the stripe intensity. We termed this phenomenon photoionization-induced lensing [29]. The effect is analogous to plasma lensing, a technique in which the high-energy charged beams in particle accelerators are focused by passing through a plasma field [74][75].

In our experiment, the pump laser photoionizes a fraction of the molecular beam sample, producing a mixture of positive ions and ejected electrons. The ejected electrons have an excess kinetic energy KE of

$$\text{KE} = nh\nu - \Phi_{\text{IP}} \quad (20)$$

where n is the number of photons involved in the excitation, ν is the photon frequency, and Φ_{IP} is the ionization potential of the molecules. These ejected electrons begin to diffuse with their excess kinetic energy, resulting in net charge redistribution within the plasma. The ions remain more or less stationary on the picosecond time scale, so the net effect is the formation of a cylindrically symmetric charge gradient and a radial electric field about the initiation laser axis that focuses the charged electron beam. With less than 1% ionization, the radial electric field in the interaction region may be as high as

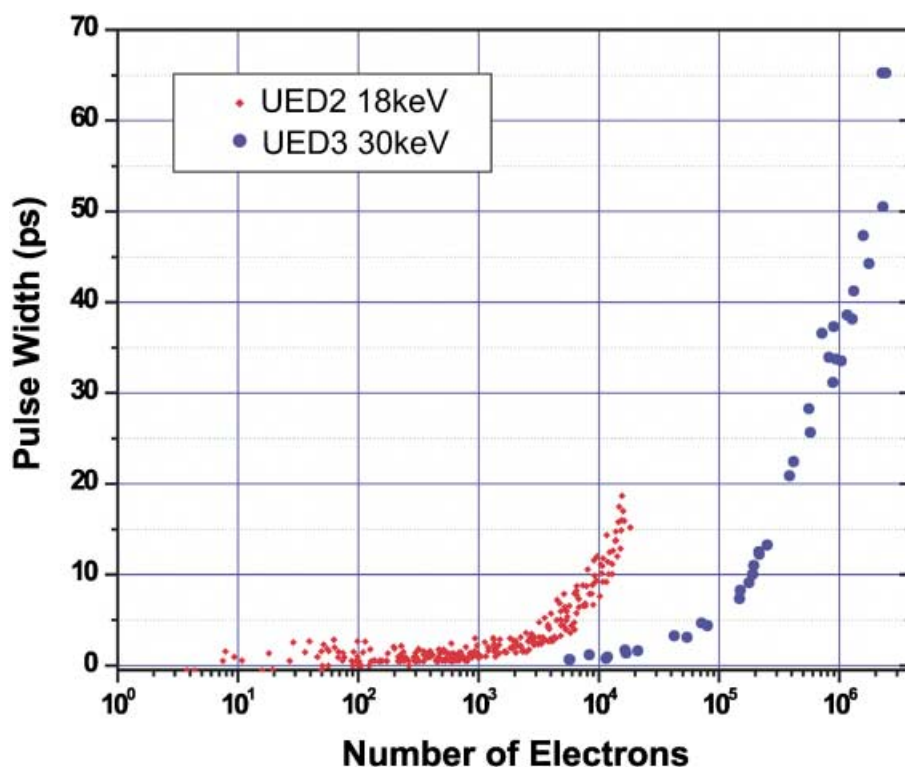


Fig. 6. Measured electron pulse widths as a function of the number of electrons. The blue curve (UED-3) shows more than an order-of-magnitude improvement in the electron gun performance in comparison to the red curve (UED-2).

10 kV/m [71], which is sufficient to perturb the path of the incoming high-energy electron beam, and the effects are seen directly in the beam spot profile.

We exploited this phenomenon to obtain the time-zero for UED experiments. Time-resolved studies of photoionization-induced lensing were conducted on CF_3I gas, which has an ionization energy of 10.23 eV. For a three-photon process with 4.66-eV photons, the excess kinetic energy of the ejected electrons is *ca.* 3.7 eV, which corresponds to the electrons traveling *ca.* 1 μm in 1 ps. Fig. 7 shows the degree of lensing vs. time; the lensing is a maximum when the focused laser and electron pulses are temporally overlapped. The time at which the ellipticity of the electron beam begins to deviate from that of a symmetric profile is defined to be the reaction zero-of-time. The results elucidate t_0 precisely and hence allow a direct clocking of changes in the diffraction experiment with picosecond or shorter resolution.

3.2.3. Temporal and Spatial Overlap: Velocity Mismatch. The velocity of 30-keV electrons is approximately one-third the speed of light. This velocity mismatch causes different molecules across the laser-electron intersection region to experience different time delays between the two pulses. For example, if the laser pulse and the electron pulse copropagate, and if both reach the near edge of the molecular beam at the same

Lensing: The Zero of Time

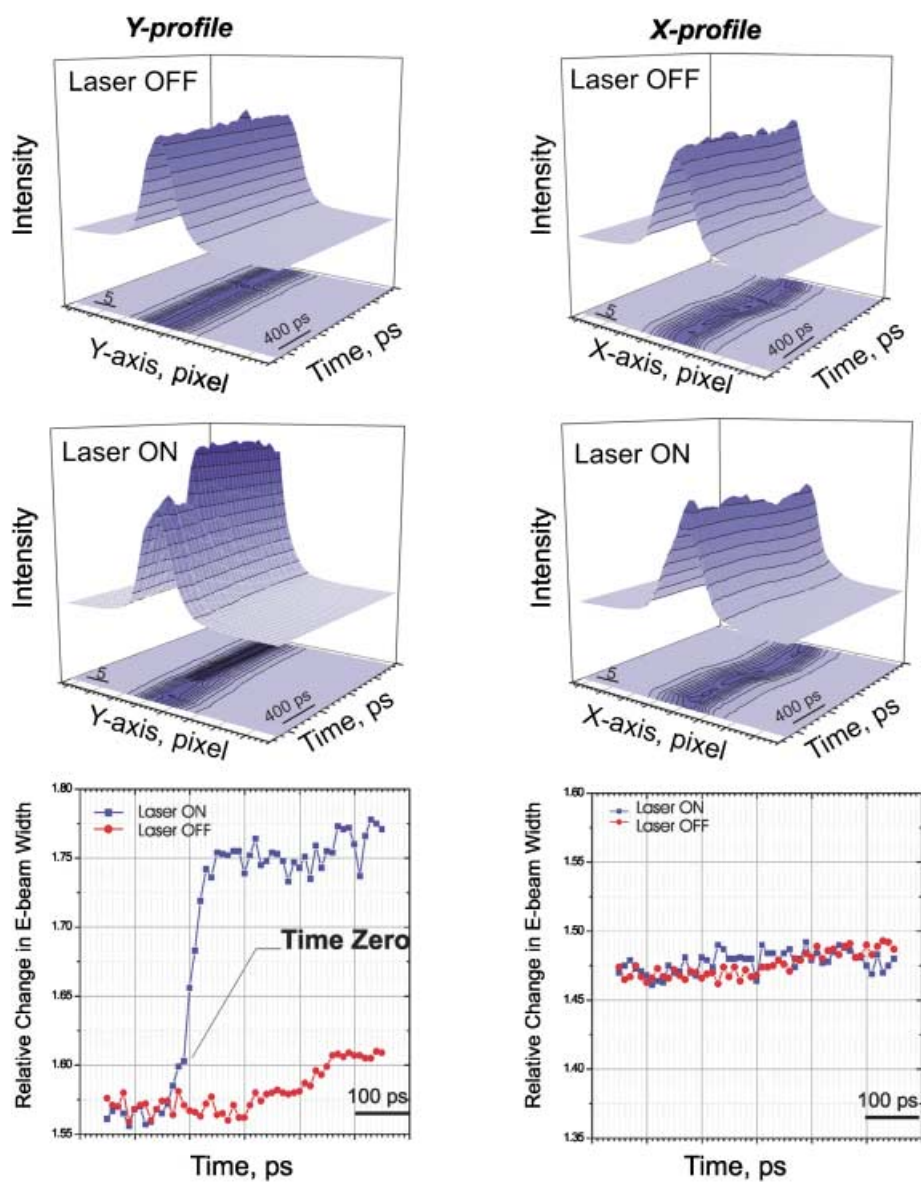


Fig. 7. Photoionization-induced 'lensing' effect for measuring zero-of-time. A molecular beam of CF_3I was used. The left panel shows the vertical profile of the electron beam, while the right panel shows the horizontal profile in the absence (*top*) and the presence (*middle*) of the laser. The *bottom* panel shows the variation of the *fwhm* of the electron beam profile as a function of the relative delay between the laser and electron pulses.

instant, then the electron beam (on account of its lower velocity) will encounter molecules at the farther edge of the sample at much later times after the light pulse has passed through. Since the time required for the electrons to cross the molecular beam sample is on the order of picoseconds, the temporal broadening due to velocity mismatch is a significant contributor to the total experimental resolution. In principle, temporal broadening due to velocity mismatch might be large enough that the total experimental resolution does not improve when shorter electron pulses or shorter laser pulses are introduced. To estimate the importance of velocity mismatch, we constructed a geometrical model to represent the temporal broadening with an analytical function in terms of experimental parameters.

Our theoretical model [27] of velocity mismatch encompasses several factors: 1) the ratio of the photon velocity to the electron velocity, κ ; 2) the spatial *fwhm* of the laser pulse, w_L ; 3) the spatial *fwhm* of the electron pulse, w_e ; 4) the cross-sectional *fwhm* of the molecular beam, w_M ; 5) the angle of intersection θ between the laser pulse and the electron pulse. When the two beams copropagate, the *fwhm* of the temporal broadening is given by

$$\Delta t_{\text{VM}}(\theta = 0) = \frac{w_M(\kappa - 1)}{c} \quad (21)$$

As expected, if the laser and electron pulses have identical velocities ($\kappa = 1$), and are co-propagating ($\theta = 0$), then there is no velocity mismatch. Note that thin molecular samples reduce Δt_{VM} , and there is negligible broadening when the electron velocity approaches the speed of light ($\kappa \rightarrow 1$).

If the spatial width of the laser pulse is sufficiently small relative to w_M

$$w_L \leq w_M \sqrt{\kappa - 1} \quad (22)$$

then the minimum temporal broadening actually occurs at a nonzero angle, θ_{min} , where

$$\theta_{\text{min}} = \arccos\left(\frac{w_L^2 + w_M^2}{\kappa w_M^2}\right) \quad (23)$$

The temporal broadening at this angle is

$$\Delta t_{\text{VM}}(\theta_{\text{min}}) = \frac{w_L}{c} \sqrt{\frac{(\kappa^2 - 1) - \frac{w_L^2}{w_M^2}}{1 + \frac{w_L^2}{w_M^2}}} \approx \frac{w_L}{c} \sqrt{\kappa^2 - 1} \quad (24)$$

which is independent of the spatial width of the electron pulse.

For our UED apparatus, $\kappa \approx 3$ and typical beam *fwhm* values are $w_e = 350 \mu\text{m}$ and $w_L = w_M = 250 \mu\text{m}$. *Fig. 8* displays the dependence of Δt_{VM} on the laser–electron beam intersection angle, and it can be seen that temporal broadening is minimized when the electron and laser beams are nearly perpendicular. In this manner, the overall temporal

resolution of the experiment (which includes contributions from the electron pulse width, the laser pulse width, and the group velocity mismatch) is calculated as a function the electron beam parameters. For an electron beam condition of 300- μm diameter, the overall temporal resolution increases to only 4 ps for a pulse of 3.5 ps. As is readily seen from *Eqn. 24*, velocity mismatch can be further reduced by decreasing the ratio of the beam velocities, κ , which in turn implies higher accelerating voltages to increase the velocity of electrons. A decrease in the laser beam and molecular beam widths and reducing the laser-electron intersection angle from the present 90° to θ_{min} (60°) (*Fig. 8*) will also serve to reduce velocity mismatch.

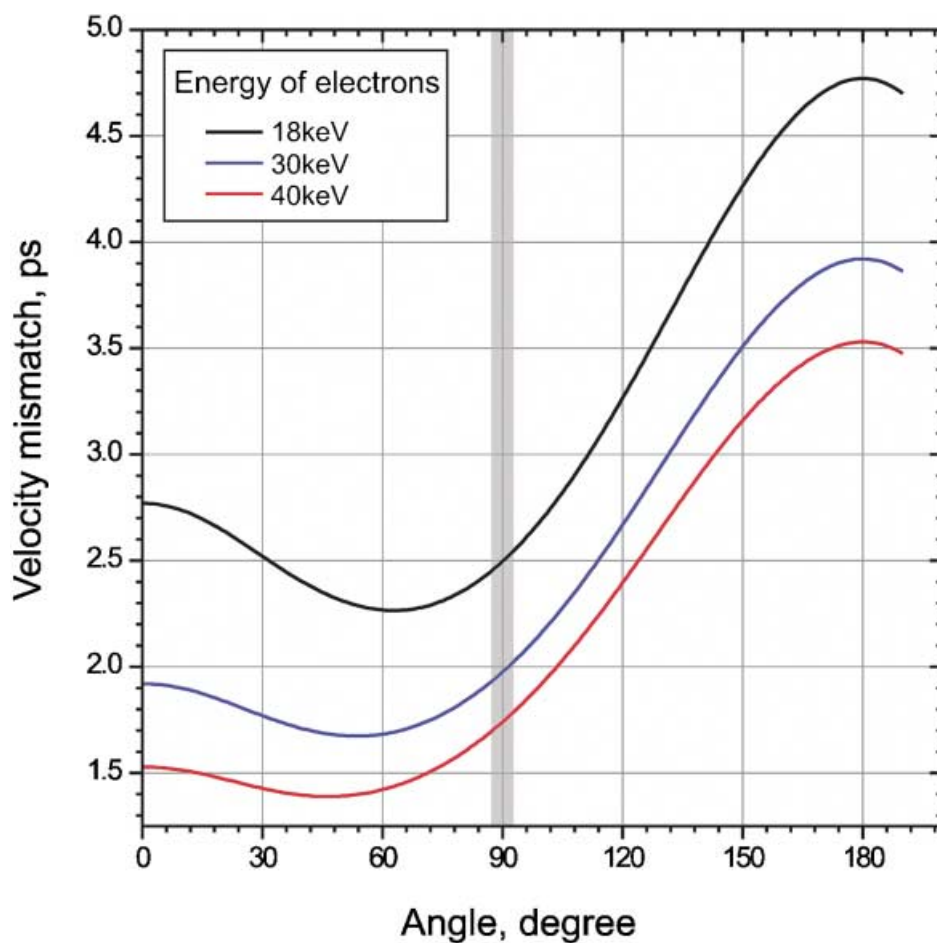


Fig. 8. Angular dependence of the temporal broadening due to velocity mismatch (see text)

4. Scope of Applications of UED

This chapter reviews the temporally and spatially resolved molecular structures, elucidated by UED, in diverse chemical phenomena. These include structures in radiationless transitions [39], structures in non-concerted organic reactions [33][35][41], structures in non-concerted organometallic reactions [31][36], structures of carbene intermediates [30][32], dynamic pseudorotary structures [40], non-equilibrium structures [38], and conformational dynamics on complex energy landscapes [42]. *Fig. 9* shows the scope of UED applications that has been achieved in our laboratory at Caltech.

4.1. Bond Breaking and Bond Making

To illustrate the principles and methodology of UED, we will first discuss a paradigm case of bond breaking and bond making in a prototypical molecule, pyridine [39]. Upon excitation, pyridine can react along several possible reaction pathways (valence isomerization, fragmentation, ring opening) as indicated in *Scheme 1*. As detailed below, UED has been successful not only in identifying the dominant reaction channel among this plethora of possibilities, but also in elucidating the transient structure of the reaction intermediate.

4.1.1. *Ground State of Pyridine.* *Fig. 10* shows the 2D ground-state diffraction image of pyridine. The peaks in the corresponding $f(r)$ curve (*Fig. 11*) directly reflect the covalent C–C and C–N distances occurring at ~ 1.3 Å, the second-nearest neighbor C··C and C··N distances at ~ 2.3 Å, and the third-nearest neighbor C··C and C··N distances at ~ 2.8 Å. The curve is in excellent agreement with previous GED data [76] and with recent quantum-chemical calculations [77].

4.1.2. *Transient Structure of Pyridine.* To resolve the structural changes during the course of the reaction, we collected UED images for a range of time delays from -90 ps to $+185$ ps. The 2D diffraction-difference images (with the image at -90 ps chosen as the reference image) clearly exhibit the emergence of periodic ring patterns (*Fig. 10*), whose intensity becomes more pronounced over time. These rings in the diffraction-difference images directly reflect the changes in the molecular structure from the reference structure at -90 ps. The corresponding 1D difference curves, $\Delta f(t; t_{\text{ref}}; r)$, shown in *Fig. 12* exhibit peaks with both negative and positive amplitudes: the negative peaks (shaded blue) represent the depletion of covalent (~ 1.3 Å region) and second-nearest neighbor (~ 2.5 Å region) distances, whereas positive peaks (shaded red) denote the formation of new internuclear pairs (those, with distances of ~ 1.1 and 1.3 Å and those with distances greater than 3.5 Å).

To discriminate between the various possible reaction channels for pyridine, the UED data was fit to a series of structural models. *Fig. 13* depicts some structures proposed in the literature for the photochemistry of such aromatic molecules: in the gas phase (*Dewar*- and *Hückel*-type isomers and $\text{C}_4\text{H}_4 + \text{HCN}$ fragmentation); liquid phase (*Dewar* isomer, azaprefulvene isomer); matrices (*Dewar* isomer and $\text{C}_4\text{H}_4 + \text{HCN}$ fragmentation), and quantum-chemical calculations (for references, see [39]). *Fig. 14* shows the comparison between the experimental transient-isolated $f(r)$ curves

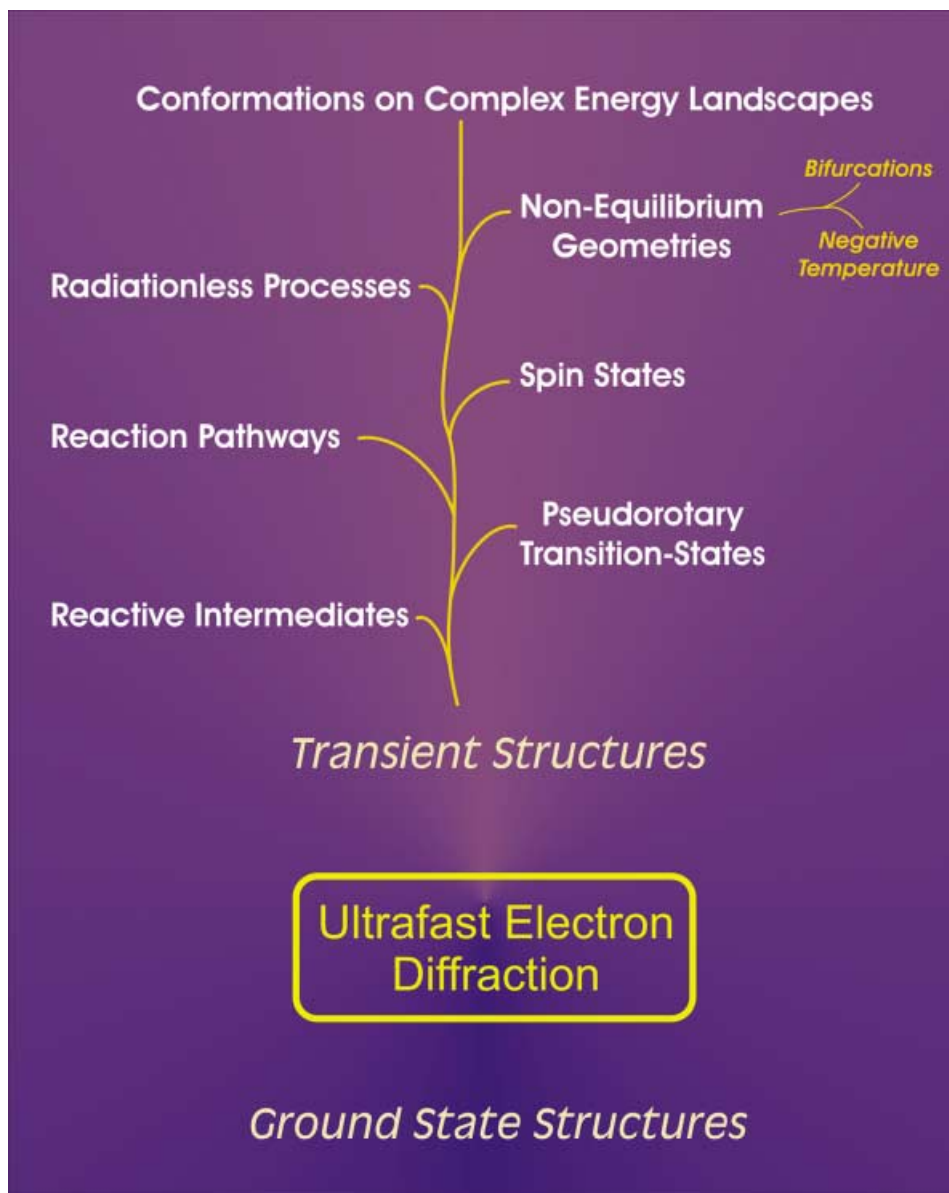
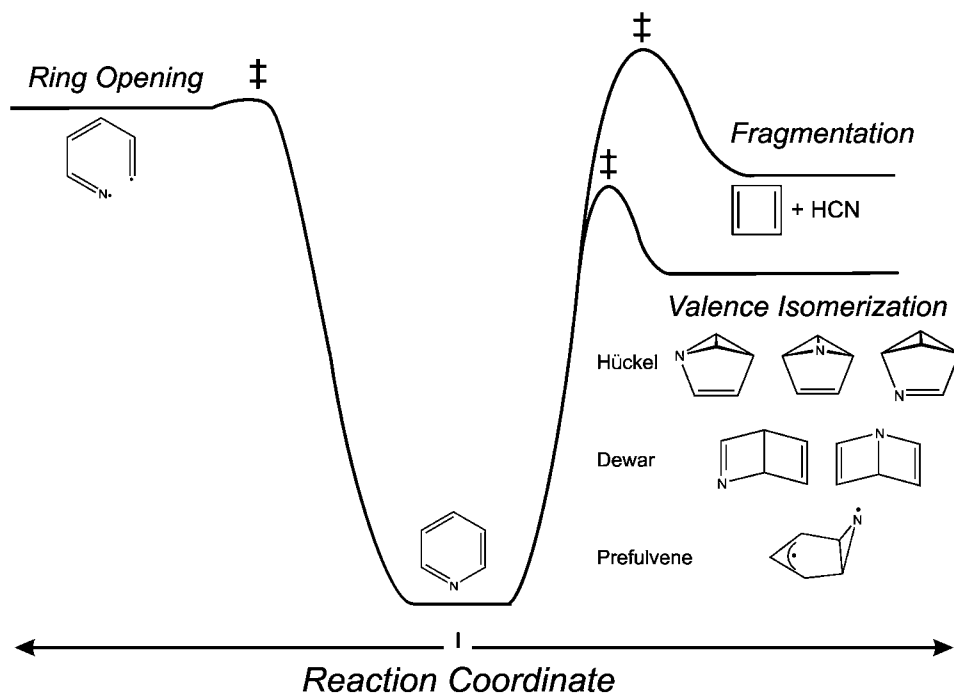


Fig. 9. The scope of phenomena and concepts elucidated by UED via the determination of ground-state and transient molecular structures

averaged over four time slices (from +60 ps to +185 ps) and the corresponding theoretical curves for various trial structures (adjusted for excess internal energy). The poor agreement between theory and experiment for the vibrationally hot *Kekulé*, *Dewar*, *Hückel*, azaprefulvene, and $C_4H_4 + HCN$ fragmentation channels precludes

Scheme 1. *Pyridine Reaction with Multiple Reaction Pathways*



Diffraction Imaging of Reactions in Real Time

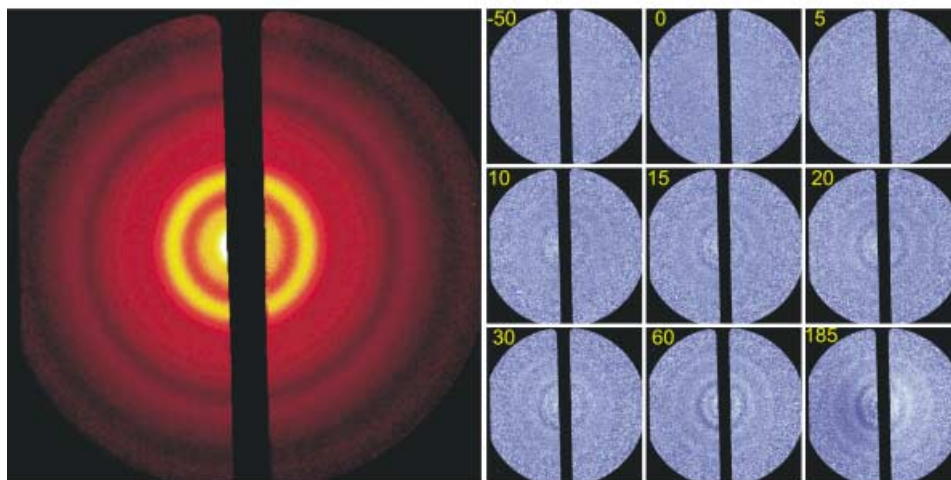


Fig. 10. *UED Images of pyridine.* The left (red) panel shows the ground-state molecular diffraction image, and the right (blue) panel shows the time-resolved 2D diffraction-difference images of pyridine. The labels on the diffraction-difference images indicate the relative time delay in picoseconds.

Pyridine Molecular Structure

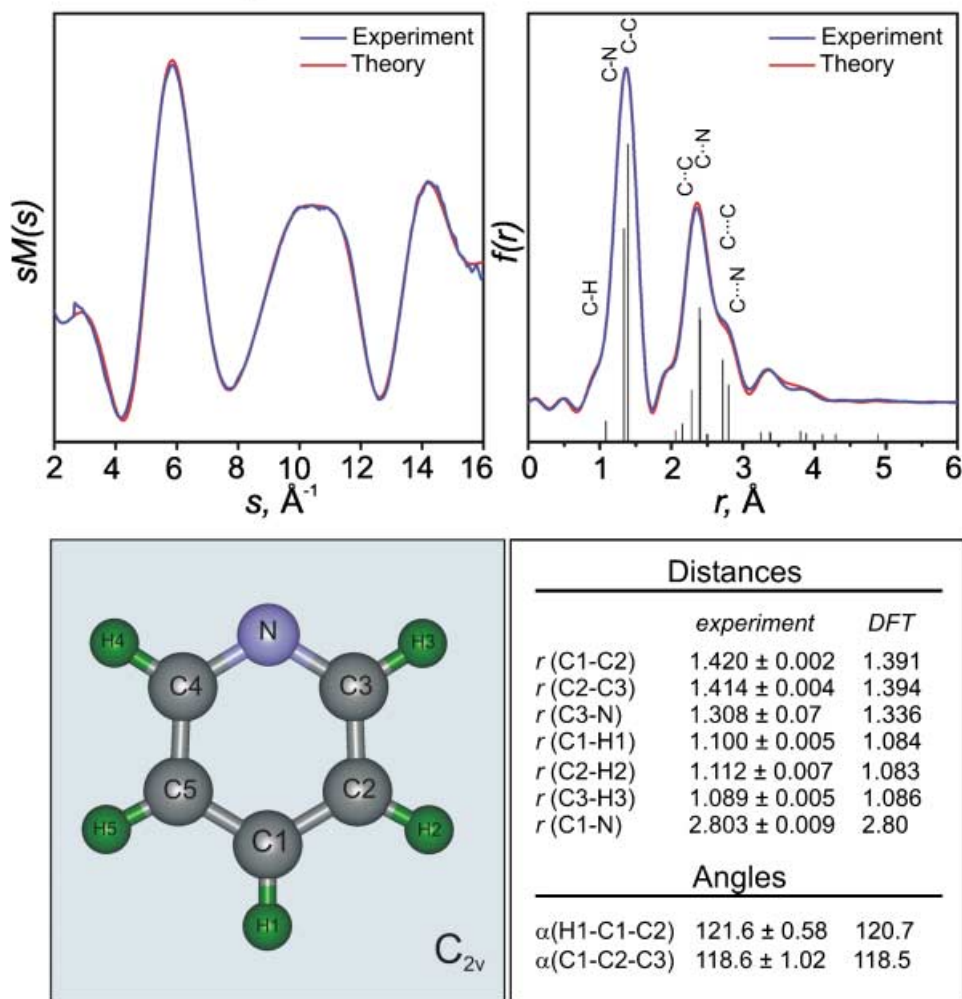
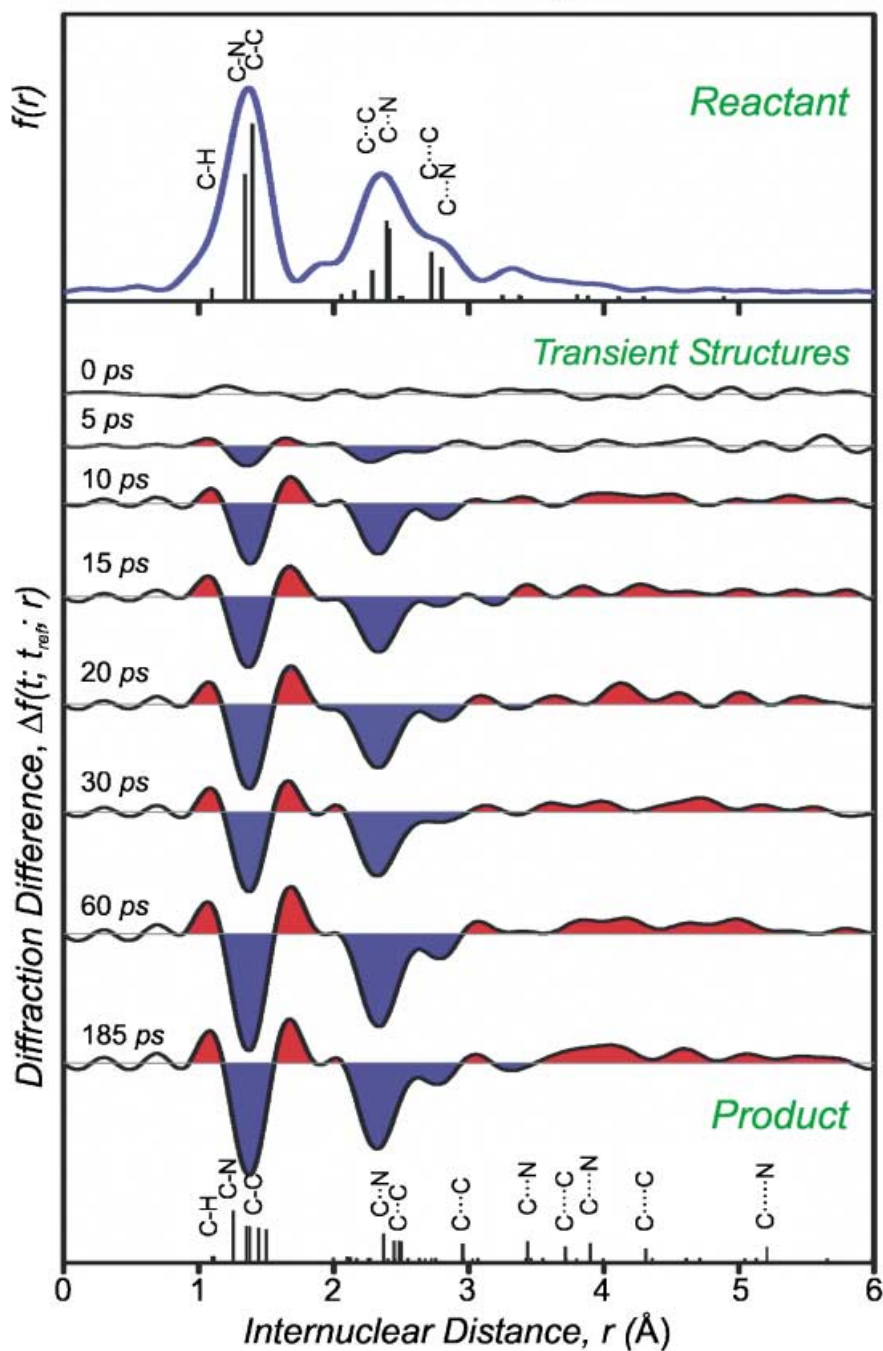


Fig. 11. Refined ground-state structure of pyridine. Comparison between the experimental and refined theoretical $sM(s)$ and $f(r)$ curves is shown, along with the determined bond distances and angles. Distances are in Å, and angles are in degrees. The C(3)–N distance was not independently refined, but derived from other best-fit (refined) distances in the structure.

Fig. 12. UED Structural dynamics. Radial distribution curves are shown for pyridine; parent (top) and $\Delta f(t; t_{\text{ref}}; r)$ curves (bottom). The vertical lines at the bottom indicate the relative contributions from various internuclear pairs, with the height of each line scaling with $(Z_i Z_j)/r_{ij}$ multiplied by the degeneracy (Z is the nuclear charge and r_{ij} is the internuclear distance). The blue highlighted regions represent net depletion of internuclear pairs ('old bonds'), whereas the red highlighted regions correspond to internuclear pairs with increasing population ('new bonds').

UED Structural Dynamics



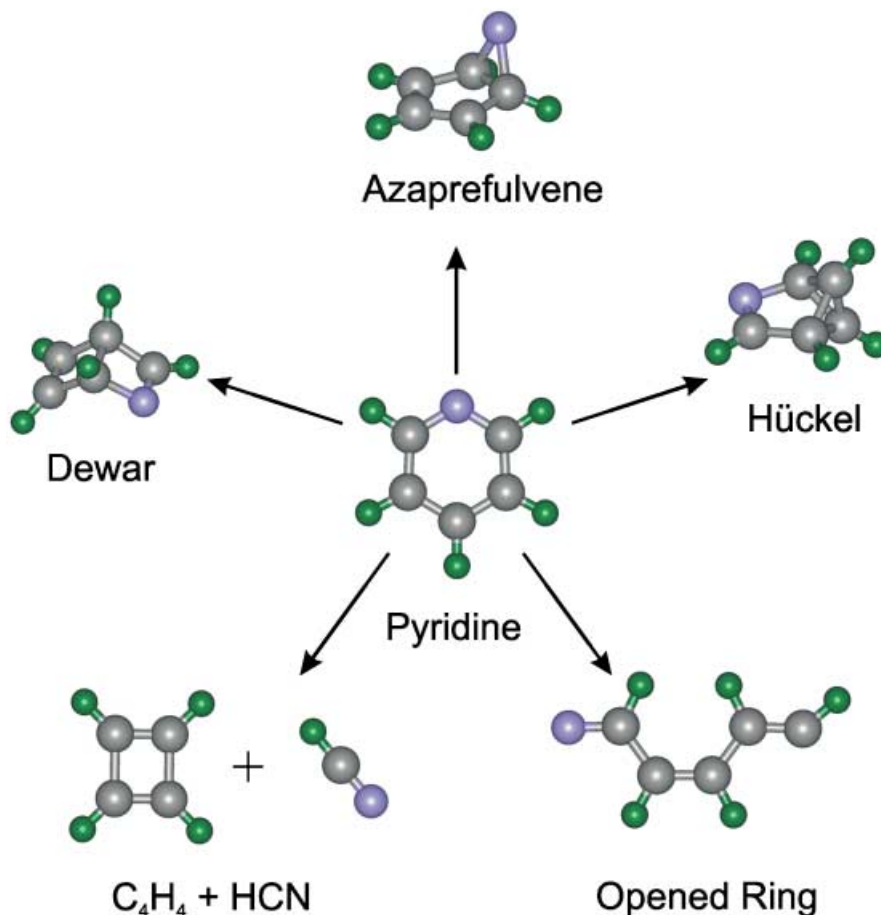


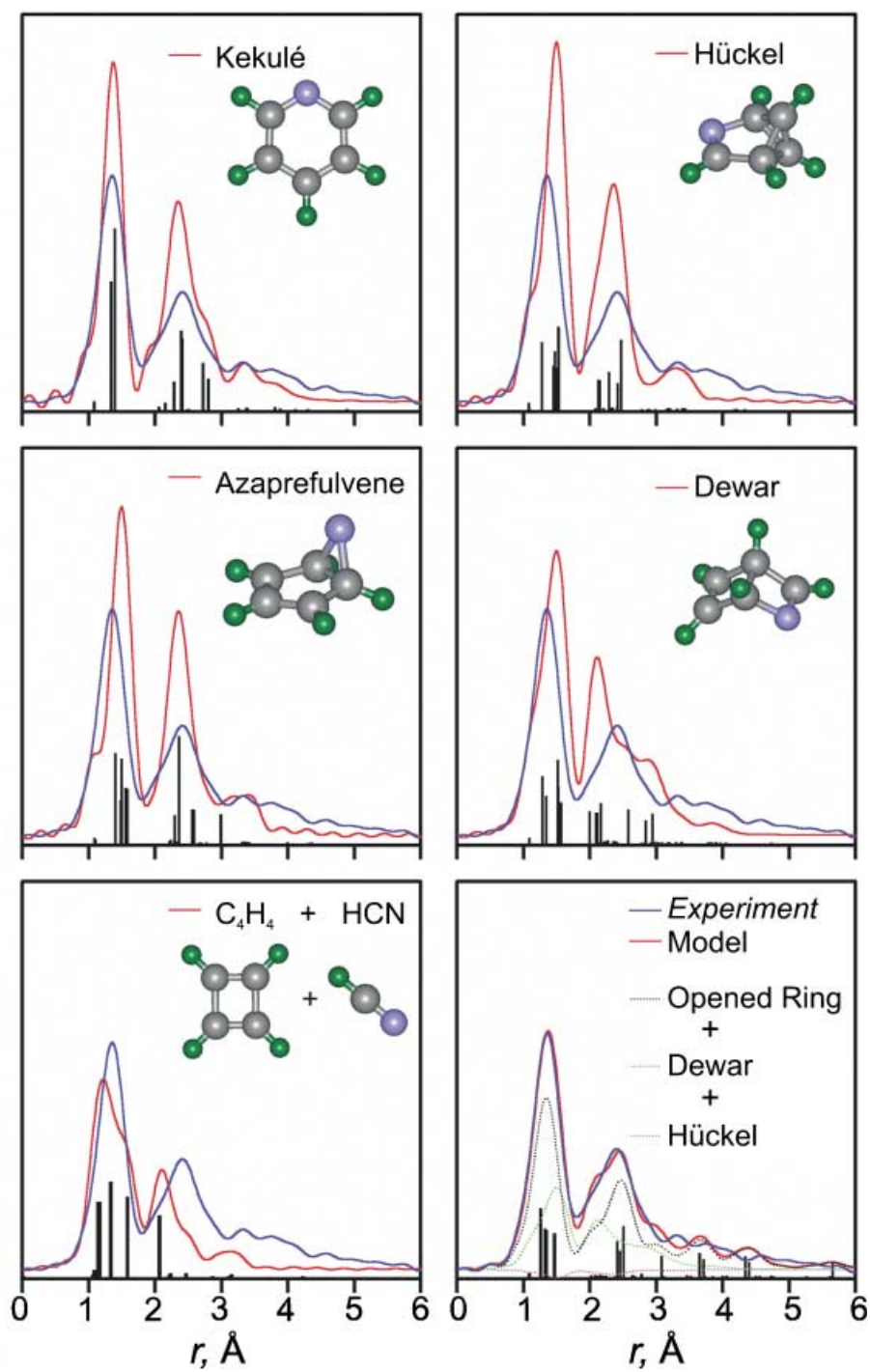
Fig. 13. Possible structures from reaction of pyridine (see Scheme 1)

these structures from being involved in the dominant reaction channel on our time scale. When a mixture of *Dewar*, *Hückel*, and vibrationally ‘cold’ (403 K) ring-opened structures was fit to the experimental $f(r)$ curve, this multi-component fit indicated that ring opening was the major channel, with the isomerization to the *Dewar* structure being the minor one; the contribution of the *Hückel* isomer was vanishingly small.

A superior structural fit was obtained using just the ring-opened structure albeit with increased internal energy, manifested by mean amplitudes of vibration 70–100% higher than those of the cold structure at 403 K. These higher vibrational amplitudes –

Fig. 14. Determination of reaction pathway. Comparisons of the experimental transient-isolated radial distribution $f(r)$ curve (blue) to normalized theoretical $f(r)$ curves (red), predicted for the structures resulting from various possible reaction channels. Discrepancies between theory and experiment are evident for all channels but one: that of the ring-opened structure with minor contributions from the valence isomers (see text).

Radial Distribution Function



reflected as damping and peak broadening in the experimental $f(r)$ curves – could easily result from a non-thermal (non-*Boltzmann*) population in the molecule's vibrational degrees of freedom, as seen below for pericyclic reactions (*Sect. 4.4*). In the presence of such hot ring-opened structures, the relative fractions of the *Dewar* and *Hückel* structures become negligible in a multi-component fit. These results establish that the primary product is a hot ring-opened structure.

Fig. 15 shows the ring-opened structure following least-squares refinement of vibrational amplitudes and internuclear distances, along with the corresponding $sM(s)$ and $f(r)$ curves. The features of this refined structure are consistent with the diffraction-difference curves of *Fig. 12*; for instance, C(1)–N distance of ~ 5.23 Å and C(1)–C(5) distance of ~ 4.33 Å correspond to the emergence of long internuclear separations, and hence the loss of covalent and next-nearest neighbor distances. As shown in *Fig. 15*, the best-fit covalent-bond distances and all but one of the angles are consistent with quantum-chemical calculations performed in this laboratory. The primary exception is one of the skeletal torsional angles, which, with a best-fit value of $\sim 123^\circ$ (instead of 180°), distorts the planarity of the predicted ring-opened structure and places the N-atom $\sim 60^\circ$ above the plane defined by the C-skeleton. Because UED measures the structure obtained for all molecules, this result must reflect the multiple torsional conformations, in concordance with a highly flexible structure.

Next, we obtained the structural evolution of the transient-isolated $f(r)$ curves, as shown in *Fig. 16*. Except for their relative intensities, the shapes of the transient-isolated curves were nearly indistinguishable over time. This indicates that the transient open structure remains nearly unchanged on the time scale of the experiment – only the population changes (see *Eqn. 8*). A least-squares fit of the transient population gave a time constant of 17 ± 1 ps (*Fig. 16*). These results, in conjunction with the difference curves in *Fig. 12*, indicate that, upon excitation, the ultrafast ring opening of pyridine disrupts its aromaticity and the ensuing open structure increases in population with a time constant of ~ 17 ps. For us to observe the dynamics reported here, the reactant structure must change significantly – thus causing the skeletal aromatic C–C distances to change to aliphatic C–C and C=C distances (see *Figs. 11* and *15*).

The above UED observations for pyridine are directly relevant to the so-called 'channel three' non-radiative process observed in many aromatic molecules. Molecules such as benzene and pyridine are known to exhibit a dramatic decrease in their fluorescence quantum yield, with concomitant passage through a rapid non-radiative relaxation process, when prepared with enough vibrational energy in the excited singlet state [78–81]. Several theoretical (see, e.g., [82][83]) and experimental investigations [81][84–87] have addressed this phenomenon since it was first observed in benzene some thirty years ago [88]. In our UED experiment, the excess vibrational energy in $S_1(n, \pi^*)$ is $\sim 2,700$ cm^{-1} – well above the $\sim 1,600$ cm^{-1} threshold for 'channel three' behavior in pyridine.

Historically, various explanations have been invoked to account for the channel three behavior; however, our UED data does not support the following proposed scenarios: *i*) direct $S_1 \rightarrow S_0$ internal conversion, which would land the molecule on the electronic ground-state with a concomitant increase in internal energy, making it vibrationally hot. We do not observe the hot parent structure despite the proven sensitivity of our UED apparatus to hot molecules (see *Sect. 4.4*); *ii*) isomerization-

Refinement of Ring-Opened Pyridine Structure

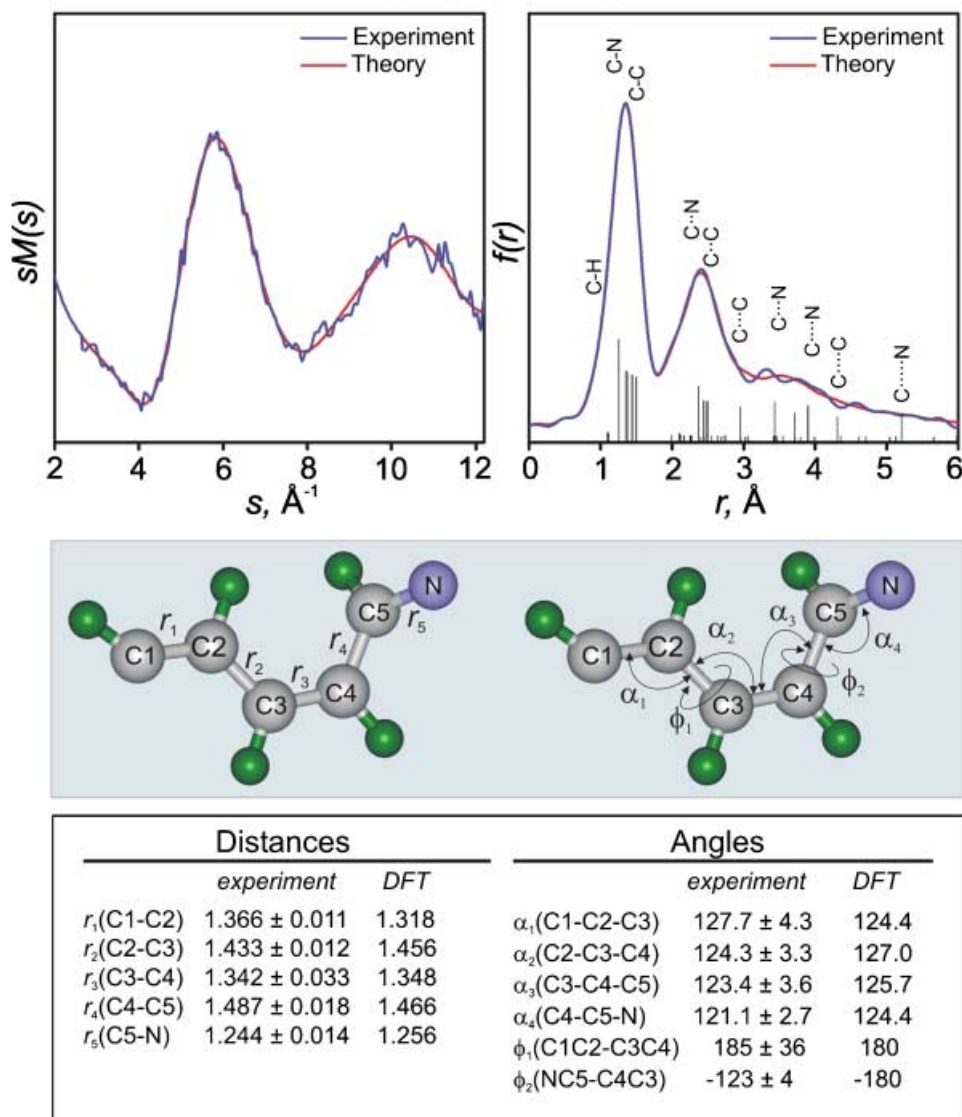


Fig. 15. Refined ring-opened pyridine structure. Shown on top are the experimental diffraction (time-averaged) curves of transients alone (blue) compared to theoretical curves corresponding to the ring-opened structure with mean I values 70–100% larger than those obtained at 403 K (red). The modified molecular scattering $sM(s)$ curves are shown on the left, and the corresponding radial distribution $f(r)$ curves are shown on the right. At the bottom are shown refined structural parameters for the ring-opened product compared to the corresponding values predicted by quantum-chemical calculations. Distances are in Å, and angles are in degrees. Note that, while the quantum calculations are for the equilibrium ring-opened structure, our refined structure accounts also for torsions, which have a low-energy barrier; hence the discrepancy in ϕ_2 .

Structure and Population Changing with Time

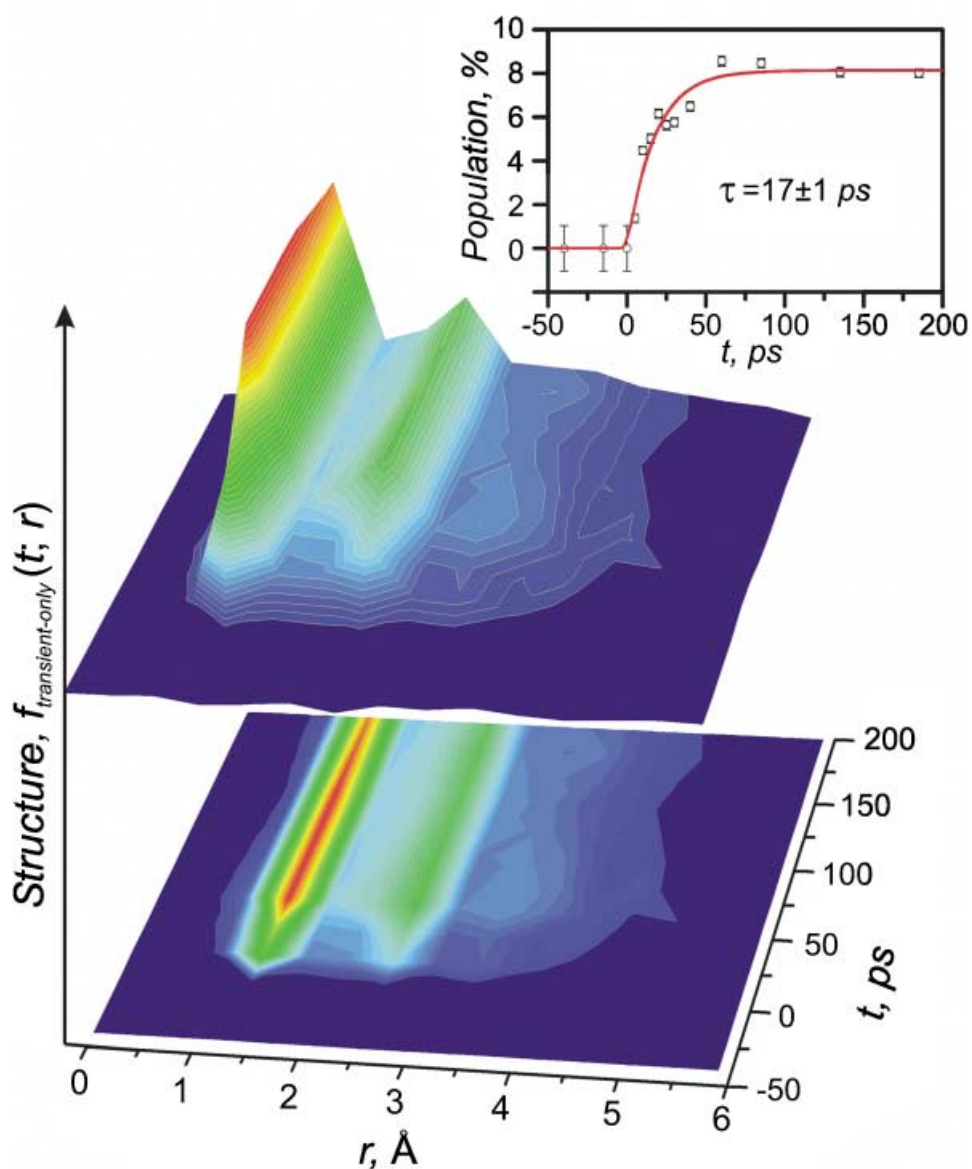


Fig. 16. Pyridine structure and population change with time. The transient-isolated curves show the formation of product structures following excitation. The inset shows the temporal dependence of the product fraction, which fits a single-component rise (*i.e.*, the formation of the ring-opened structure) and yields a time constant of 17 ± 1 ps. The 2D plot indicates the range of internuclear distances (0–6 Å) and their change as a function of time (see text).

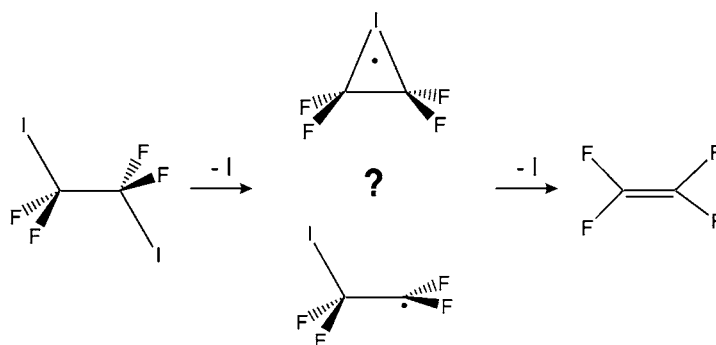
mediated internal conversion (*e.g.*, *via* the *Dewar*, *Hückel*, or *azaprefulvene* structures), which can also be ruled out based on the poor fits to these isomers (*Fig. 14*). Femtochemistry studies of pyridine in the gas [77] and condensed [89] phases have revealed the timescales of the dynamics, but the structures involved were not elucidated, rather assigned based on energetics.

For this paradigm case of pyridine, UED, for the first time, uncovered a previously unknown ring-opened diradical intermediate structure resulting from C–N bond scission – this observed ring-opened structure casts new light on the decades-old puzzle of channel-three behavior occurring in many aromatic molecules. The ring-opened diradical structure was isolated from among a plethora of possibilities for reaction pathways. Through determination of the reactant (*Fig. 11*) and transient (*Fig. 15*) molecular structures, we are able to relate the structural changes in bond distances and angles to the timescale of population changes involved in bond breaking and bond making. Further studies completed in this laboratory on derivatives of pyridine confirm the above mechanism and show a direct correlation between the transient structure and dynamics of radiationless transitions, as detailed elsewhere.

4.2. Reactive Intermediate Structures

For many reactions – even of a single channel – there exist intermediate structures between reactants and products (*Eqn. 7*), and UED can be applied to chart such changes. We chose the prototypical non-concerted elimination reaction of dihaloethanes [33][35][41] to demonstrate the UED methodology of using different electron pulse sequences – different t_{ref} – to isolate the reactant, intermediate, and product structures. The consecutive nature of the C–I bond breakage was first elucidated *via* picosecond photofragment spectroscopy [90] and, subsequently, by femtosecond kinetic-energy resolved time-of-flight (KETOF) mass spectrometry, permitting the state, velocity, and angular evolution of the relevant species to be resolved [91]. Following excitation [91], the first I-atom is lost on the femtosecond timescale to form the transient $\text{C}_2\text{F}_4\text{I}$ radical intermediate (*Scheme 2*). The remaining internal energy, left to redistribute within the vibrational degrees of freedom of the $\text{C}_2\text{F}_4\text{I}$ radicals, was

Scheme 2. Non-Concerted Elimination Reaction of $\text{C}_2\text{F}_4\text{I}_2$ with the Hitherto Unknown Intermediate Structure



enough to induce secondary C–I fragmentation in a majority of the hot intermediates – resulting in the loss of the second I-atom and the formation of the tetrafluoroethylene product on the picosecond timescale. However, the structure of the intermediate was not directly resolved in those experiments.

A comparison of *Scheme 2* with *Eqn. 7* indicates that the relevant chemical species in this reaction are those of reactant ($C_2F_4I_2$), intermediate (C_2F_4I), and product (C_2F_4). The structural dynamics of this reaction will be reflected in their population change as well as change in their structure, manifested in $\sigma_a(t; s)$ of *Eqn. 8*. Moreover, the non-concerted nature of this reaction allows us to isolate different transient species based upon our choice of t_{ref} in the diffraction-difference methodology.

4.2.1. *Ground-State Structures of $C_2F_4I_2$* . The experimental results for the ground-state structures of $C_2F_4I_2$ are shown in *Fig. 17*. The $C_2F_4I_2$ molecule is known to have two conformational minima with respect to torsional rotation about the C–C bond: an *anti* structure with a χ ICCI torsion angle of 180° and C_{2h} symmetry, and a *gauche* structure with χ ICCI $\approx 70^\circ$ and C_2 symmetry. In the study by *Hedberg* and co-workers [92], the experimental structural parameters for $C_2F_4I_2$ were refined under the simplifying assumption that the *anti* and *gauche* conformers possess identical values for the structural parameters, except for the χ ICCI dihedral angle. Correspondingly, identical *anti/gauche* parameter values were used in our analysis, although recent quantum-chemical calculations have suggested that the C–C and C–F distances of the *anti* conformers may be slightly shorter, and the C–I distances slightly longer, than those of the *gauche* conformers [37].

Both ground-state structures were observed in the electron-diffraction data shown in *Fig. 17*; the ratio of these conformers was determined *via* least-squares refinement to be $76:24 \pm 2$ *anti/gauche*. This ratio, which is governed by the sample temperature and the energy difference between the conformers, was in excellent agreement with the previous results obtained by *Hedberg* and co-workers at 120°C [92]. Very good agreement can be seen between $sM^E(-95\text{ ps}; s)$ and $sM^T(-95\text{ ps}; s)$ and in the corresponding experimental and theoretical $f(-95\text{ ps}; r)$ curves in *Fig. 17*. The various interatomic distances of the *anti* and *gauche* $C_2F_4I_2$ structures are indicated at the bottom of *Fig. 17* and can be summarized as follows: the peak at $\sim 1.4\text{ \AA}$ results from covalent C–F and C–C distances; the peak at $\sim 2.2\text{ \AA}$ results from covalent C–I and nonbonded F \cdots F and C \cdots F distances; the peak at $\sim 3\text{ \AA}$ is comprised of nonbonded F \cdots I, C \cdots I, and F \cdots F distances; and the peaks at $\sim 3.8\text{ \AA}$ and $\sim 5.1\text{ \AA}$ correspond to the nonbonded I \cdots I distances for the *gauche* and *anti* conformers, respectively.

4.2.2. *Structural Dynamics of the $C_2F_4I_2$ Reaction*. The time-dependent difference radial distribution curves referenced to -95 ps , $\Delta f^E(t; -95\text{ ps}; r)$, which directly indicate the structural changes occurring over the course of the reaction, are shown in *Fig. 18 (left)*. It is significant to note that the negative peak intensity at $\sim 5.1\text{ \AA}$ in the $\Delta f(r)$ curves remains constant after 5 ps , whereas the peak intensities around $2\text{--}3\text{ \AA}$ continue to increase over a longer time scale. As shown in the figure, the negative peak at $\sim 5.1\text{ \AA}$ results from the loss of the I \cdots I internuclear separation of the *anti* conformer of the parent $C_2F_4I_2$ molecules, while those at $2\text{--}3\text{ \AA}$ result primarily from the depletion of C–I, F \cdots I, and C \cdots I distances. These observations demonstrate the non-concerted nature of the structural changes in the reaction: The first step ($C_2F_4I_2 \rightarrow C_2F_4I + I$) is essentially complete within the 5 ps window – consistent with the sub-

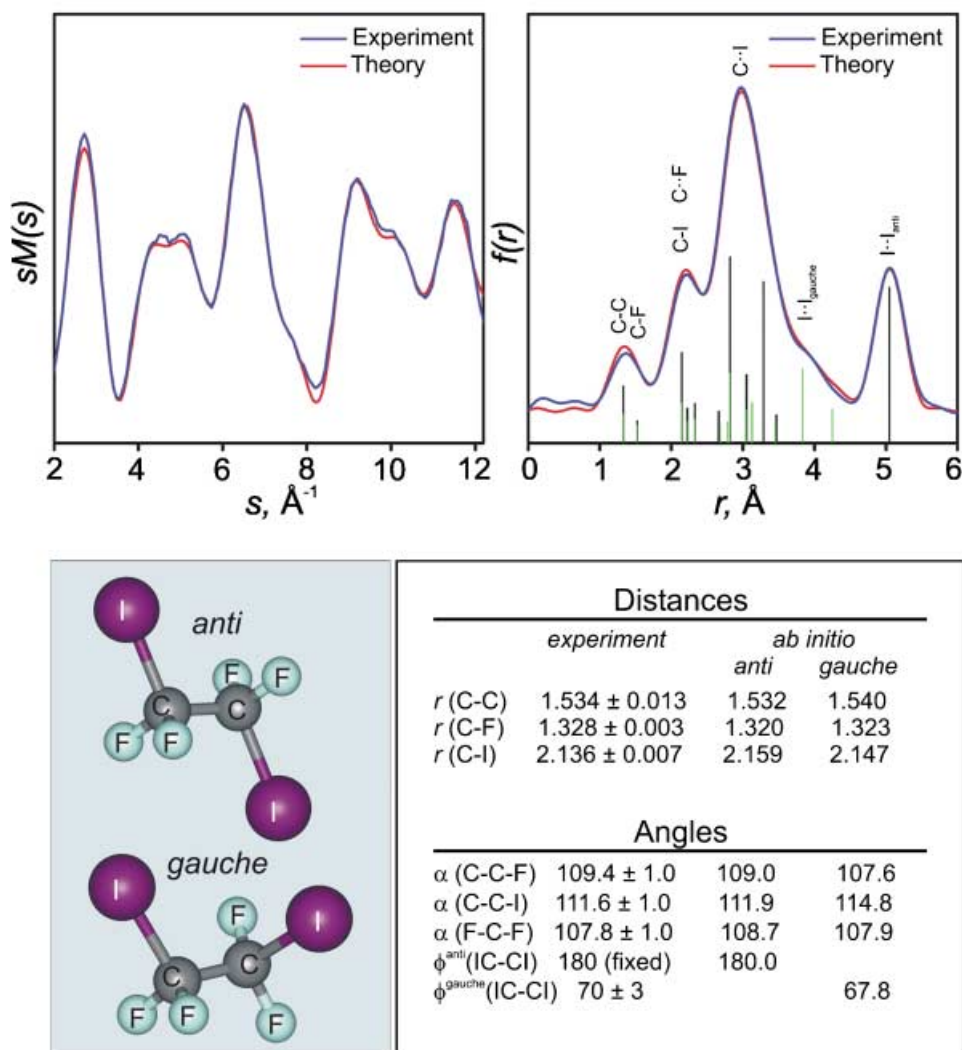
Molecular Structure of $C_2F_4I_2$ 

Fig. 17. Refined ground-state structure of $C_2F_4I_2$. The comparison between the experimental and refined theoretical $sM(s)$ and $f(r)$ curves is shown, along with the determined bond distances and angles for the *anti* and *gauche* conformers. Distances are in Å, and angles are in degrees. The bond distances for the *anti* (black) and *gauche* (green) isomers are indicated by vertical lines at the bottom of the $f(r)$ panel.

picosecond time constant measured by time-of-flight mass spectrometry in this laboratory [91], whereas the second step ($C_2F_4I \rightarrow C_2F_4 + I$) is considerably slower, taking place over tens of picoseconds (see below).

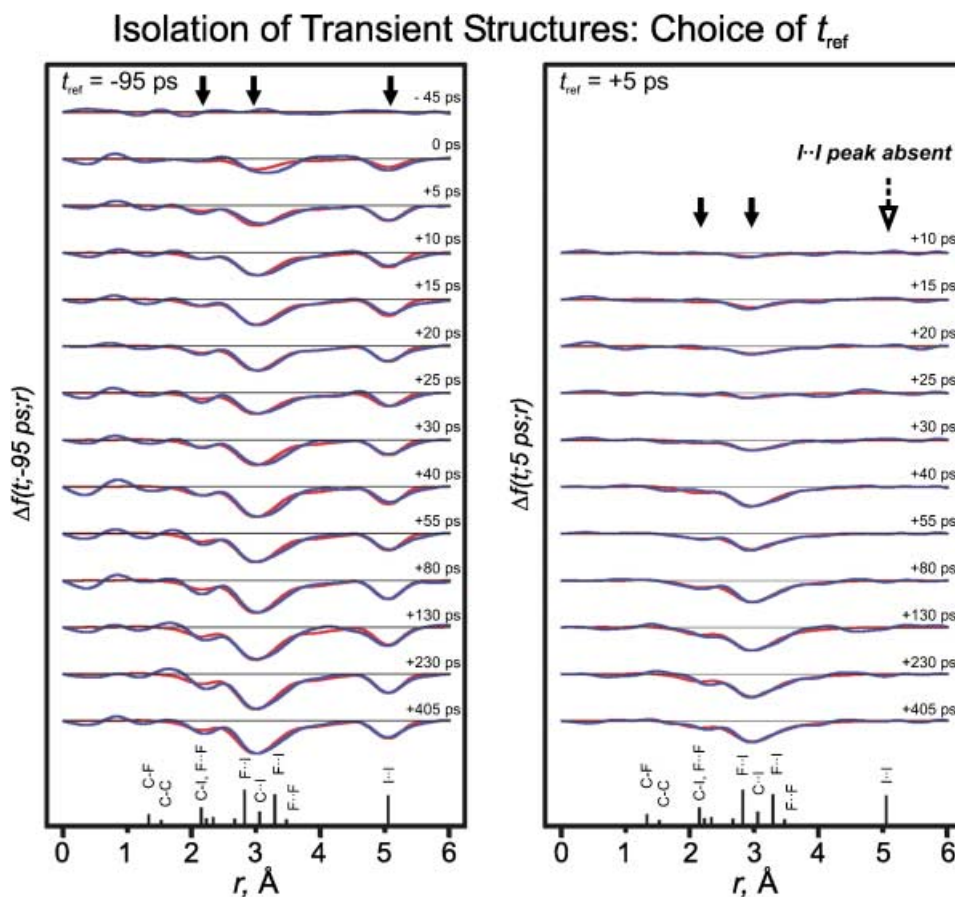


Fig. 18. Isolation of transient species through choice of t_{ref} . Blue are the experimental $\Delta f(t; 95 \text{ ps}; r)$ curves (left) and $\Delta f(t; 5 \text{ ps}; r)$ curves (right) obtained at varying time delays with subsequent Fourier filtering (the Fourier cutoff was 9 \AA); theoretical curves are shown in red. Note that the negative peak at $\sim 5 \text{ \AA}$ is absent in the difference curves referenced to $+5 \text{ ps}$. Internuclear distances of the ground-state *anti* conformer are indicated below the two panels for reference.

The diffraction-difference, referenced at $t_{\text{ref}} = -95 \text{ ps}$, contains the transient structure, the reactant (of similar magnitude), and the product:

$$\Delta sM(t; -95 \text{ ps}; s) = -|\Delta p_{\text{C}_2\text{F}_4\text{I}_2}| \cdot sM(s)_{\text{C}_2\text{F}_4\text{I}_2} + |\Delta p_{\text{C}_2\text{F}_4\text{I}}| \cdot sM(s)_{\text{C}_2\text{F}_4\text{I}} + |\Delta p_{\text{C}_2\text{F}_4}| \cdot sM(s)_{\text{C}_2\text{F}_4} \quad (25)$$

with

$$\Delta p_{\text{C}_2\text{F}_4} + \Delta p_{\text{C}_2\text{F}_4\text{I}} = -\Delta p_{\text{C}_2\text{F}_4\text{I}_2} \quad (26)$$

where Δp is the change in species population – depletion of reactant or rise of intermediate and product. Thus, the fractions of the reactants, intermediates, and products can be determined; for the reaction under consideration, these time-

dependent populations result in an average time constant of 26 ± 7 ps for the depletion of C_2F_4I transient structures (20 ± 5 ps) and formation of C_2F_4 molecules (31 ± 4 ps).

Since the reaction involving the reactant $C_2F_4I_2$ is complete within the first 5 ps, we generated a set of additional diffraction-difference curves with $t_{\text{ref}} = 5$ ps – in order to highlight the structural changes of the reaction intermediate and product only – with no contribution from any other species present. *Fig. 18 (right)* shows the corresponding difference radial distribution curves, $\Delta f^E(t; 5 \text{ ps}; r)$. The $\Delta f(t; 5 \text{ ps}; r)$ signals arise only from the transient C_2F_4I and final product C_2F_4 species, with the depletion of the C_2F_4I radical being evident at C–I, C··I, and F··I separations; note that the populations of other internuclear separations (*e.g.*, C–F, C–C, and F··F) are essentially unchanged. The absence of an I··I component (~ 5.1 Å) in the $\Delta f^E(t; 5 \text{ ps}; r)$ curves clearly shows that we are observing solely the population change of the transient C_2F_4I structures forming C_2F_4 :

$$\Delta sM(t; 5 \text{ ps}; s) = - |\Delta p_{C_2F_4I}| \cdot sM(s)_{C_2F_4I} + |\Delta p_{C_2F_4}| \cdot sM(s)_{C_2F_4} \quad (27)$$

with

$$\Delta p_{C_2F_4} = -\Delta p_{C_2F_4I} \quad (28)$$

Theoretical $\Delta f^T(t; 5 \text{ ps}; s)$ curves (*red* curves in *Fig. 18*) were obtained by a single-parameter fit (the fraction of C_2F_4 species) of the experimental $\Delta sM^E(t; 5 \text{ ps}; s)$ curves. The time-dependent population of C_2F_4 formed after 5 ps yields a time constant of 25 ± 7 ps, in excellent agreement with the above analysis of the $\Delta f(t; -95 \text{ ps}; r)$ curves.

4.2.3. Freezing the Structure of the C_2F_4I Intermediate. The molecular structure of the C_2F_4I radical intermediate was determined from the diffraction-difference curves $\Delta sM(t; 5 \text{ ps}; s)$; both bridged and classical C_2F_4I structures were considered in the fitting of the diffraction data. The symmetrically bridged structure has C_{2v} symmetry, whereas the *anti* and *gauche* conformers of the classical structure have C_s and C_1 symmetry, respectively. *Fig. 19* shows the experimental $\Delta sM^E(\infty; 5 \text{ ps}; s)$ and $\Delta f^E(\infty; 5 \text{ ps}; r)$ curves along with the corresponding theoretical curves produced with quantum-chemical structures. As can be seen from the figure, the theoretical curves for the mixture of classical structures reproduce the experimental data extremely well, whereas the fit provided by the theoretical bridged structure is vastly inferior. Indeed, the $\Delta sM^E(\infty; 5 \text{ ps}; s)$ and $\Delta sM^T(\infty; 5 \text{ ps}; s)$ curves in *Fig. 19* clearly go out of phase for the bridged structure, yielding manifestly different positions for the two prominent negative peaks in the corresponding $\Delta f^E(\infty; 5 \text{ ps}; r)$ and $\Delta f^T(\infty; 5 \text{ ps}; r)$ curves. Thus, we conclude that the structure of the C_2F_4I radical intermediate is, in fact, classical in nature; this quantitative analysis using UED-3 is in general agreement with previous qualitative analysis from UED-2 experiments [33].

A least-squares refinement of the $\Delta sM^E(\infty; 5 \text{ ps}; s)$ data was performed to determine the structural parameters of the C_2F_4I intermediate (*Fig. 20*). The C–I and C–C distances of the C_2F_4I intermediate are longer and shorter, respectively, than those of the reactant, while the C–F' internuclear distance in the radical site (–CF'₂) is shorter than that of the –CF₂I site. These results elucidate the increased C–C and decreased C–I bond order expected from the formation of the transient C_2F_4I structure. Moreover, the $\sphericalangle CCF'$ and $\sphericalangle F'CF'$ angles become larger than the

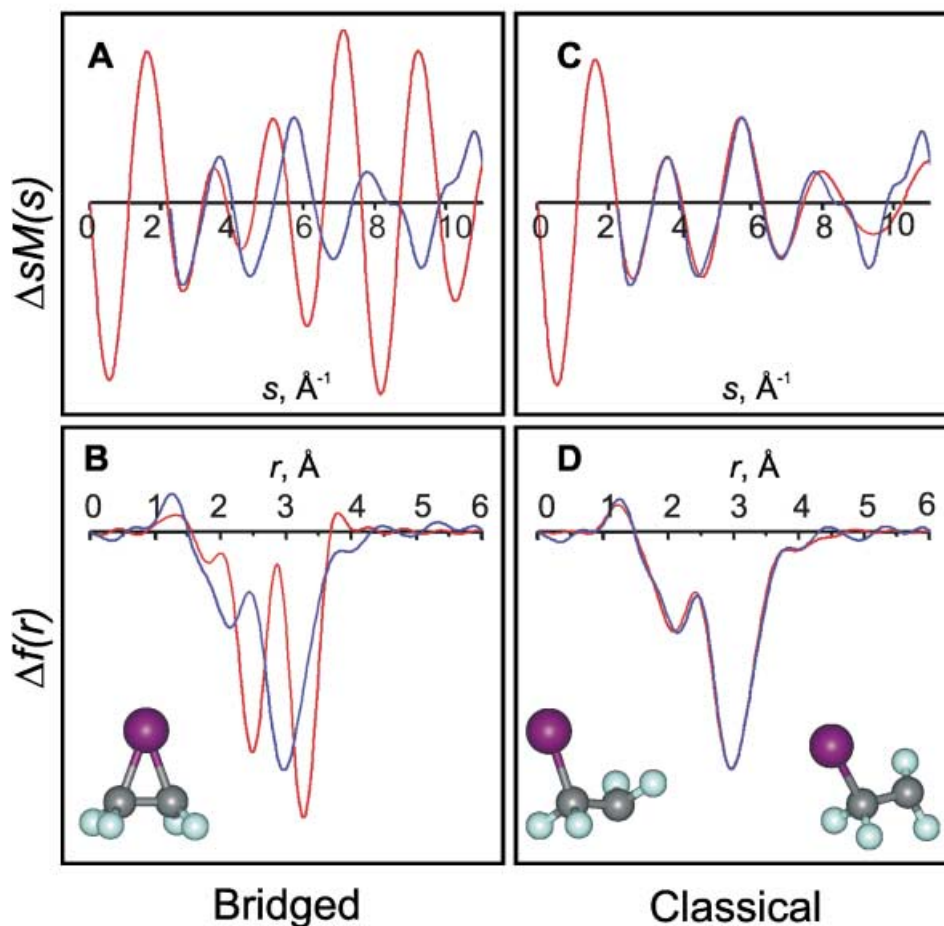
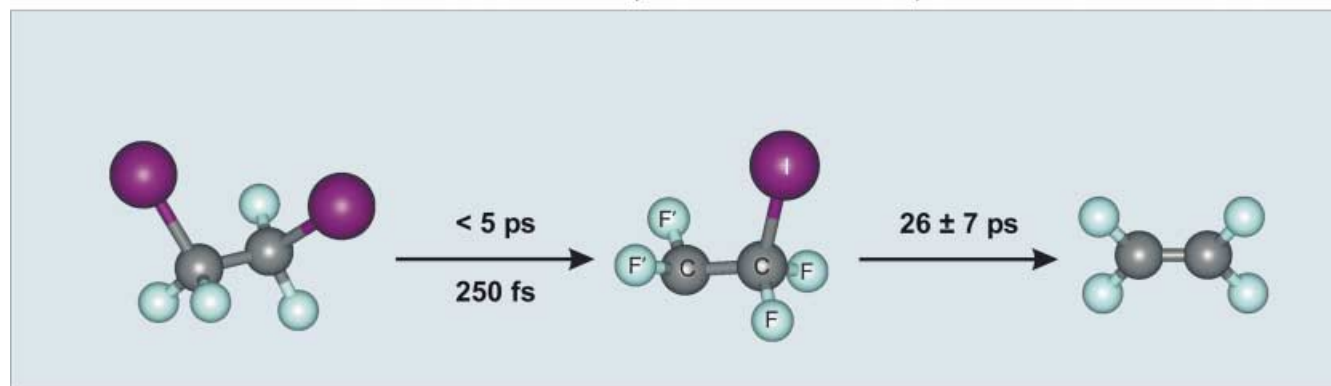
Structure of C_2F_4I Transient Intermediate

Fig. 19. Structural determination of the transient C_2F_4I intermediate. A), B) Comparison of experimental $\Delta sM(\infty; 5 \text{ ps}; s)$ and $\Delta f(\infty; 5 \text{ ps}; r)$ curves (blue) with corresponding theoretical curves (red) obtained via *ab initio* calculations of the bridged structure for C_2F_4I . C), D) Comparison of experimental $\Delta sM(\infty; 5 \text{ ps}; s)$ and $\Delta f(\infty; 5 \text{ ps}; r)$ curves with theoretical curves obtained using the *ab initio* classical (*anti* and *gauche*) C_2F_4I structures.

corresponding angles of the reactant (by $\sim 9^\circ$ and $\sim 12^\circ$, resp.), suggesting that the radical center ($-CF'_2$) of the C_2F_4I intermediate relaxes following loss of the first I-atom.

The above results are vital in describing the role of dynamics in the retention of stereochemistry in such reactions. In the chemistry of halogen elimination reactions, products are usually formed under stereochemical control with respect to the final positions of the functional groups about the newly formed double bond [93–95]. The origin of this well-known behavior has been hypothesized to lie in the geometry of the

Structures of Reactant, Intermediate, and Product



Distances			
	<i>experiment</i>	<i>ab initio</i>	
		<i>anti</i>	<i>gauche</i>
$r(\text{C-C})$	1.534 ± 0.013	1.532	1.540
$r(\text{C-F})$	1.328 ± 0.003	1.320	1.323
$r(\text{C-I})$	2.136 ± 0.007	2.159	2.147

Angles			
	<i>experiment</i>	<i>anti</i>	<i>gauche</i>
$\alpha(\text{C-C-F})$	109.4 ± 1.0	109.0	107.6
$\alpha(\text{C-C-I})$	111.6 ± 1.0	111.9	114.8
$\alpha(\text{F-C-F})$	107.8 ± 1.0	108.7	107.9
$\phi^{\text{anti}}(\text{IC-Cl})$	180 (fixed)	180.0	
$\phi^{\text{gauche}}(\text{IC-Cl})$	70 ± 3		67.8

Distances			
	<i>Experiment</i>	<i>ab initio</i>	
		<i>anti</i>	<i>gauche</i>
$r(\text{C-C})$	1.478 ± 0.049	1.503	1.508
$r(\text{C-F})$	1.340 ± 0.037	1.322	1.327, 1.323
$r(\text{C-I})$	2.153 ± 0.013	2.164	2.149
$r(\text{C-F}')$	1.277 ± 0.027	1.304	1.309, 1.307

Distances		
	<i>Experiment</i>	<i>DFT</i>
$r(\text{C-C})$	1.311 ± 0.021	1.306
$r(\text{C-F})$	1.319 ± 0.006	1.312

Angles		
	<i>Experiment</i>	<i>DFT</i>
$\alpha(\text{C-C-F})$	123.8 ± 0.6	123.8

Fig. 20. Complete structural determination of the $\text{C}_2\text{F}_4\text{I}_2$ elimination reaction. The bond distances and angles for all three species are shown, along with the *ab initio* and DFT values for comparison. Distances are in Å, and angles are in degrees. Note that the C–C bond distance becomes progressively shorter from reactant through intermediate to product, thus reflecting the change in bond order from a single bond to a double bond. Also, note the change in bond angles of $\text{C}_2\text{F}_4\text{I}$, which reflects relaxation of structure (see text). For the ground-state structural parameters, see [37] and [92]; for the product, see [168].

reaction intermediate. For example, quantum-chemical calculations [34] have shown that CH_2BrCH_2 and CH_2ICH_2 radicals should form stable, symmetrically ‘bridged’ structures. If so, this will be consistent with the *Skell* hypothesis for the origin of stereochemical control in such systems [96][97]. In a symmetrically bridged structure, the primary halide (*i.e.*, I or Br) is shared equally between the two $-\text{CR}_2$ moieties, whereas, in a ‘classical’ structure, the primary halide would reside predominantly on one $-\text{CR}_2$ moiety [97]. A bridged structure would, thus, prevent rotation about the C–C bond, thereby maintaining the functional group positions in the final product.

In all of these reactions, the question remains: is the stereochemistry and product formation controlled by the structure of the intermediate or by the relative timescales of elimination *vs.* rotation? The UED results indicate that dynamical effects play a role in the retention of configuration in such reactions; if the time for the second C–X bond breakage is shorter than that of rotation around the C–C bond, configuration will be retained even in reactions involving classical $\text{C}_2\text{R}_4\text{X}$ structures. Our measured reaction time (25 ± 7 ps) for this process and the determined *classical* structure of the intermediate indicate that the retention of configuration is controlled by the dynamical timescale of the reaction, relative to the timescale of rotations – electronic structural changes are not necessarily the key for retention of configuration.

4.3. Transition-State Pseudorotary Structures

Even for larger and more complex structures, UED can determine the reaction pathway, and elucidate the nature of the product structure at energies above the reaction barrier. UED studies on (cyclopentadienyl)cobaltdicarbonyl ($\text{CpCo}(\text{CO})_2$; *Scheme 3*) have provided the structure of the reactant, as well as the product cyclopentadienyl (Cp) radical – the structure is that of the *transition state* between the compressed (dienylic) and the elongated (allylic) conformations of Cp, but with longer bond distances and elevated mean amplitudes of vibration, thus reflecting the dynamics of the pseudorotary surface [40].

4.3.1. *Ground State of $\text{CpCo}(\text{CO})_2$.* *Fig. 21* shows the $sM(s)$ and the $f(r)$ curves for the parent $\text{CpCo}(\text{CO})_2$ molecule. The ground-state structural parameters, obtained after least-squares refinement, are also shown (along with the results of our DFT calculations). Our refinement gives Co–C_{ring} distances of 1.93 and 2.26 Å for the shortest and longest distances, respectively; the average value of all five Co–C_{ring} distances is ~ 2.09 Å. The DFT values vary from 2.09 to 2.15 Å (average value of ~ 2.13 Å). In the GED experiment by *Beagley et al.* [98], it was assumed that the $\text{CpCo}(\text{CO})_2$ had five-fold symmetry for the ring and two-fold symmetry as a whole, and a single value (2.12 Å) was reported for all Co–C_{ring} bonds in the conventional GED analysis. Our best-fit analysis and electronic structure calculations shown above indicate that the Co–C_{ring} distances are more consistent with X-ray crystallographic data; from one report [99], the Co–C_{ring} bonds are given as 2.01 to 2.23 Å (average value of 2.09 Å) and from another report [100] the Co–C_{ring} bonds vary from 2.06 to 2.11 Å (average value of 2.08 Å). The Co–C_{carbonyl} distance determined by UED is within one standard deviation of the GED data and shorter than the theoretically determined value by 0.067 Å.

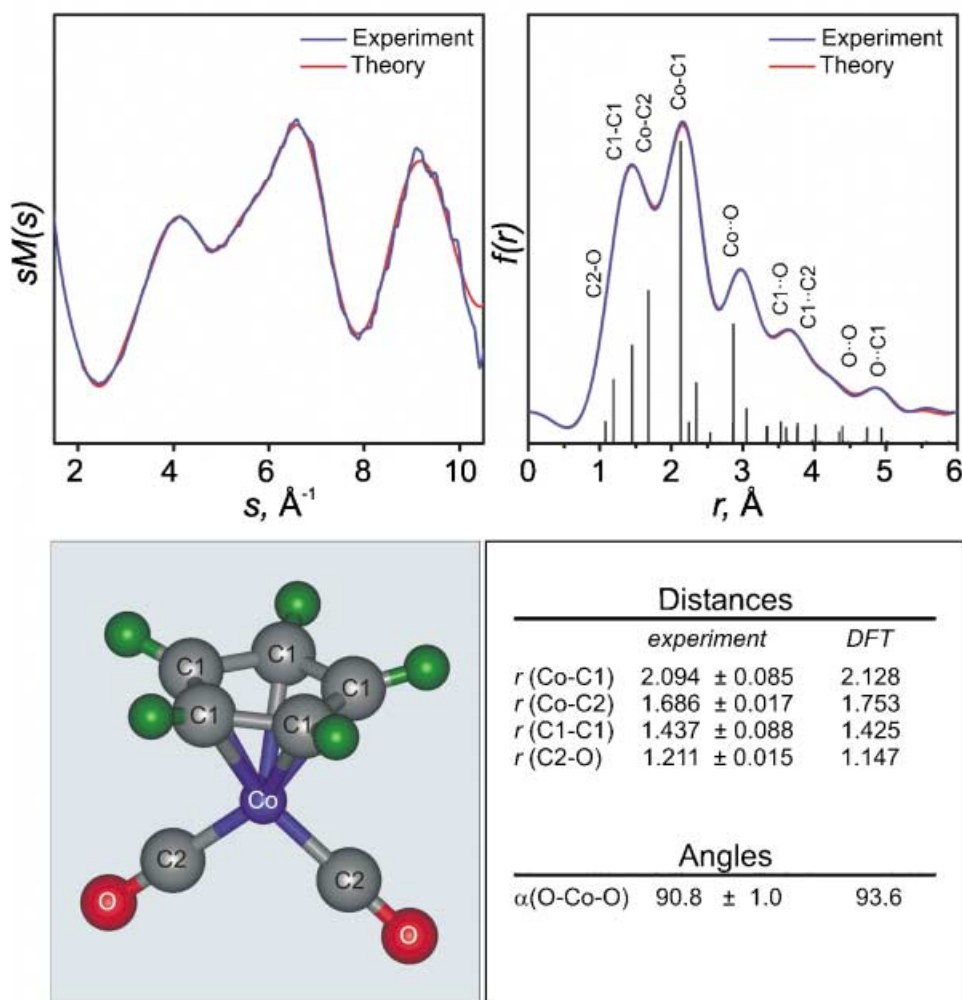
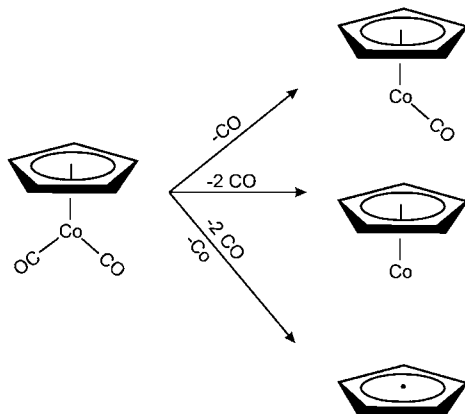
Molecular Structure of $\text{CpCo}(\text{CO})_2$ 

Fig. 21. Refined ground-state structure of $\text{CpCo}(\text{CO})_2$. The comparison between the experimental and refined theoretical $sM(s)$ and $f(r)$ curves is shown, along with the determined bond distances and angles. Distances are in Å, and angles are in degrees.

The C–C bonds within the Cp ligand take values from 1.41 to 1.46 Å and the average value (1.44 Å) is consistent with the only $\text{C}_{\text{ring}}-\text{C}_{\text{ring}}$ bond distance (1.45 Å) supplied by GED of the parent [98]. Finally, the $\text{C}_{\text{carbonyl}}-\text{O}$ bond length ($1.211 \pm .015$ Å) is also consistent with the GED data (1.191 ± 0.004 Å) and longer by 0.064 Å than that predicted by theory. Fig. 21 shows the very good agreement between the experimental data and our refined theoretical model.

4.3.2. *Transient Structures of Cp.* As depicted in *Scheme 3*, there are three possible reaction channels involving the loss of one or both CO moieties and the Co-center. We consider the diffraction-difference curves in order to establish which reaction channel(s) is (are) dominant. *Fig. 22* shows the comparison between the data and theory for these three possible products. For a starting point, the structural parameters of these different species were obtained from our own DFT calculations and also from the literature [101]. It is clear from *Fig. 22* that Cp is the main product, and that the other reaction product structures are nearly absent. A fit including all three structures was also performed by floating the fraction of each species while keeping their structural parameters fixed at the values obtained from quantum-chemical calculations, and Cp is overwhelmingly favored.

Scheme 3. $[\text{CpCo}(\text{CO})_2]$ Fragmentation Reaction with Many Possible Products



Careful examination of the $\Delta f(r)$ curve (*Fig. 22*) reveals rich details of the structural change occurring due to the depletion of $\text{CpCo}(\text{CO})_2$ and the formation of Cp. The first distinct peak centered at $\sim 2 \text{ \AA}$ indicates the depletion of $\text{Co}-\text{C}_{\text{carbonyl}}$ and $\text{Co}-\text{C}_{\text{ring}}$ bonds, and the second peak centered just below 3 \AA indicates the depletion of the $\text{C}_{\text{carbonyl}} \cdots \text{C}_{\text{ring}}$ and $\text{Co} \cdots \text{O}$ distances. The third peak centered at $\sim 3.5 \text{ \AA}$ indicates the depletion of the $\text{C}_{\text{ring}} \cdots \text{C}_{\text{carbonyl}}$ and $\text{C}_{\text{ring}} \cdots \text{O}$ distances, and the last shoulder indicates the depletion of $\text{O} \cdots \text{C}$ and $\text{O} \cdots \text{O}$ distances. The first peak corresponding to the $\text{Co}-\text{C}_{\text{carbonyl}}$ and $\text{Co}-\text{C}_{\text{ring}}$ separations clearly shows that the Cp ring and the CO groups have been separated from the Co-center. A least-squares fit of the Cp structural parameters was performed on the difference curve, and the result is shown in *Fig. 23*. The transient-only curve (*Fig. 23*) shows two dominant peaks: one for the C–C bonds at $\sim 1.4 \text{ \AA}$ and the other for the indirect $\text{C} \cdots \text{C}$ distances at $\sim 2.3 \text{ \AA}$. The final refined structures of Cp obtained from the diffraction-difference and transient-only curves were identical.

Cp, a classic ligand, has long played an important role in different areas of chemistry, both theoretically [102–105] and experimentally [106–109]. Cp is an orbitally degenerate doublet radical subject to a *Jahn–Teller* distortion into a pair of C_{2v} -symmetric conformers joined by a pseudorotary surface. Quantum-chemical theory

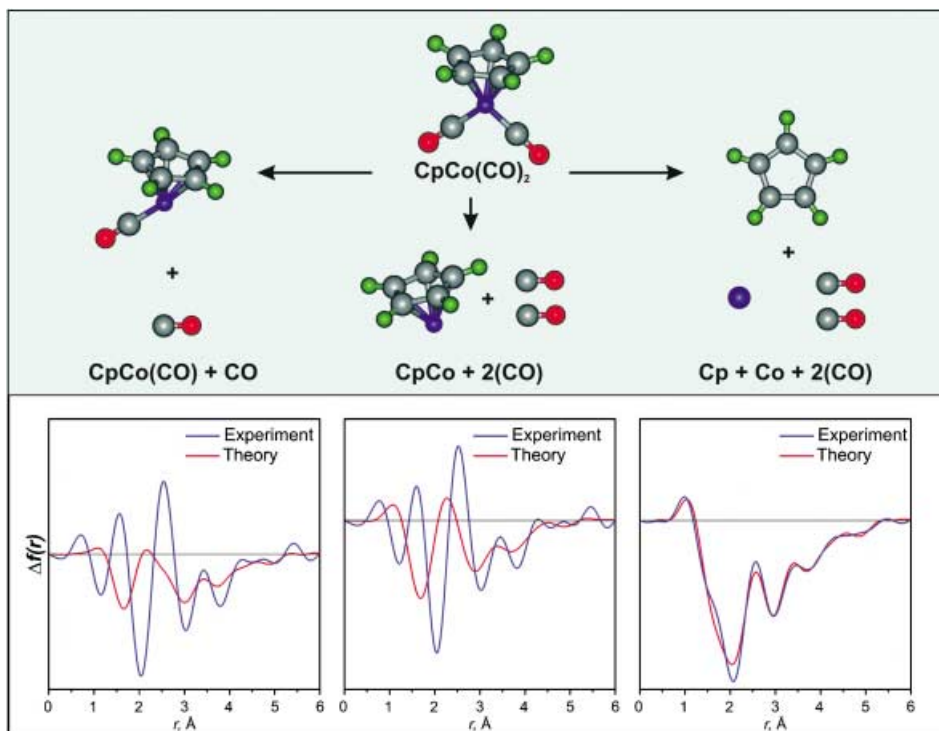


Fig. 22. *Identification of reaction pathway.* The comparison between the experimental diffraction-difference $f(r)$ curves and the theoretical fits is shown for the three possible reaction channels. Clearly, the Cp reaction channel is in very good agreement with the experimental data. However, the Cp curve was approximated by a half and half mixture of *elongated* and *compressed Jahn–Teller* isomers; a vastly superior fit is obtained after structural refinement (see Fig. 23 and text).

predicts that the *Jahn–Teller* distortion from the D_{5h} structure stabilizes Cp by 3.5 kcal/mol [103]. The distorted, lower-energy ring assumes either a compressed (dienylic) or an elongated (allylic) conformation, which are nearly energetically degenerate (within 0.05 kcal/mol) [103]. Structural deviation from D_{5h} symmetry is large with some previously equal bond lengths now being different by as much as 0.1 Å. However, due to the near energetic degeneracy of the two isomers, Cp exists in a dynamic state of pseudorotation.

To examine the nature of these dynamic structures, we initially used a 50:50 mixture of the *elongated* and *compressed Jahn–Teller* isomers to fit the diffraction-difference data. However, our least-squares refinement yielded unsatisfactory results for a mixture composed of two ‘static structures’. Instead, the fit equilibrium bond lengths strayed significantly from the theoretically determined *Jahn–Teller* structures, indicating the participation of an array of dynamic structures. This *stretched* ring of D_{5h} symmetry (a regular pentagon) and the large error bars (± 0.2 Å for some of the C–C bonds) resulting from the refinement of a 50:50 mixture suggested that an alternative, more satisfactory dynamic model was needed to fit the data. With this in mind, we used

Refined Structure of Pseudorotary Cp Radical

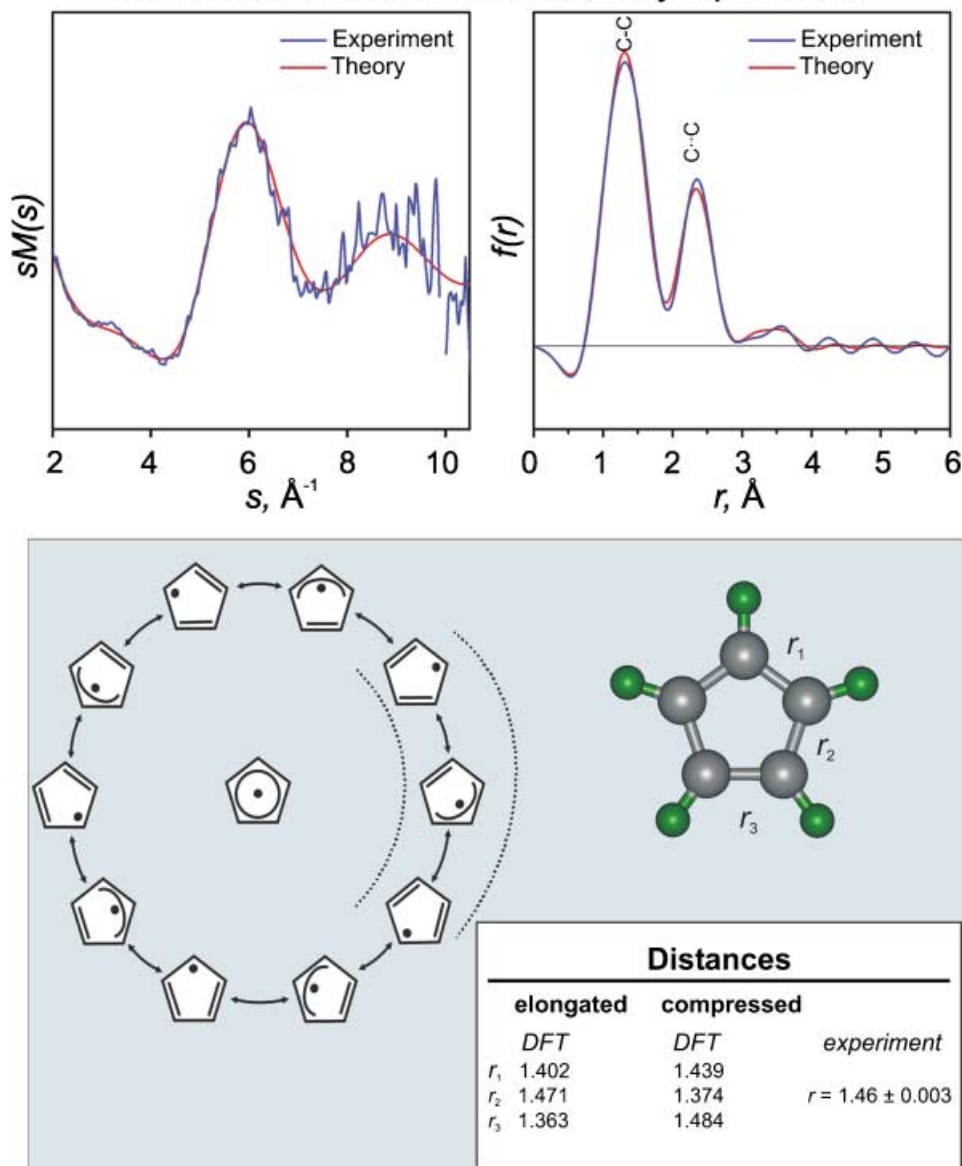


Fig. 23. Refined transition-state pseudorotary structure of Cp. The top panel shows the comparison between theory and experiment for the transient-only $sM(s)$ and $f(r)$ curves of the D_{5h} Cp structure at 2600 K. The bottom panel shows the refined Cp structure along with the determined bond distances in Å. The bottom panel also shows a schematic representation of pseudorotation in the Cp radical. In the center is the D_{5h} transition state 3.5 kcal/mol above the circular pseudorotary surface connecting the elongated and compressed *Jahn–Teller* isomers of Cp. The transition states along the circular path are estimated to be elevated by energies ranging from zero to ca. 2 kcal/mol [107]. The dotted circles indicate two of the many other possible paths.

the regular pentagonal structure to represent the dynamics of all conformational change. The DFT electronic structure of D_{5h} -Cp was then used as the starting condition for the refinement. The best fit of our data was obtained when the C–C bond of the D_{5h} ring was 1.46 ± 0.003 Å. DFT gave 1.42 Å, which is consistent with the results from rotationally resolved laser-induced fluorescence spectroscopy [108]. The DFT calculations refer to the bond distance of 1.42 Å of the D_{5h} -symmetric transition state, and we attribute the observed 0.04 Å extension of the equilibrium bond length to the pseudorotary transition-state dynamics about the Cp ring.

A refinement of the molecular temperature, based on the mean amplitudes of vibration of the bonds, was also performed [40], and our best-fit temperature of the D_{5h} -symmetric product was 2600 ± 150 K. This apparent high temperature is a consequence of the highly entropic phase space, which results from the many vibrations involved in the dynamic transformations of the structures. Thus, the long bonds of the refined Cp structure and the high vibrational temperature elucidate the dynamic nature of pseudorotation in this species. An active pseudorotary state involves many bonds changing lengths as the molecule constantly converts between elongated and compressed isomers. The rapid movement of Cp through these pathways at high internal energy is represented by a hot and enlarged D_{5h} -symmetric transition-state structure as shown in *Fig. 23*.

4.4. Non-Equilibrium Structures

Studies of molecular structures at or near their equilibrium configurations have long provided information on their geometry in terms of bond distances and angles. Far-from-equilibrium structures are relatively unknown – especially for complex systems – and generally, neither their dynamics nor their average geometries can be extrapolated from equilibrium values. For such non-equilibrium structures, vibrational amplitudes and bond distances play a central role in phenomena such as energy redistribution and chemical reactivity. Before considering specific examples of non-equilibrium structural determination, it would be instructive to discuss some key concepts underlying structures at equilibrium and those far-from-equilibrium.

4.4.1. *Concepts of Equilibrium vs. Non-Equilibrium Structures.* In this discussion, we will classify molecular structures into the following four cases: *a*) Equilibrium, *Boltzmann* distribution (Type I) – Cold Ground State; *b*) Equilibrium, *Boltzmann* distribution (Type II) – Hot Ground State; *c*) Non-equilibrium, non-*Boltzmann* distribution (Type I) – Inverted population, ‘negative temperature’; and *d*) Non-equilibrium, non-*Boltzmann* distribution (Type II) – Bifurcation of internuclear distances. Differences between diffraction patterns of structures at equilibrium and those far-from-equilibrium can be understood by first considering the case of a single bond (*Fig. 24*). The diffraction of structures far from equilibrium manifests itself as *i*) increased damping of the oscillating molecular scattering signal; and *ii*) apparent shifts in internuclear distance(s). As seen in *Fig. 24*, simple thermal heating of the molecule results in nearly the same average internuclear distance, but its vibrational amplitude increases with temperature. This elevated l value can be readily observed as enhanced damping of $sM(s)$; the relevant dependence is given, from *Eqn. 4*, by

$$sM(s) \propto \exp\left(-\frac{1}{2}l^2s^2\right) \cdot \frac{\sin(sr)}{r} \quad (29)$$

This damping is mirrored as broadened peaks in the $f(r)$ curve because of its *Fourier* (sine) transform relation to $sM(s)$. The damping reflects thermal averaging over the vibrational states in a *Boltzmann* distribution, given in the harmonic diatomic limit (l_h) as [46]

$$l_h^2 = \frac{h}{8\pi^2\mu\nu} \coth\left(\frac{h\nu}{2kT}\right), \quad (30)$$

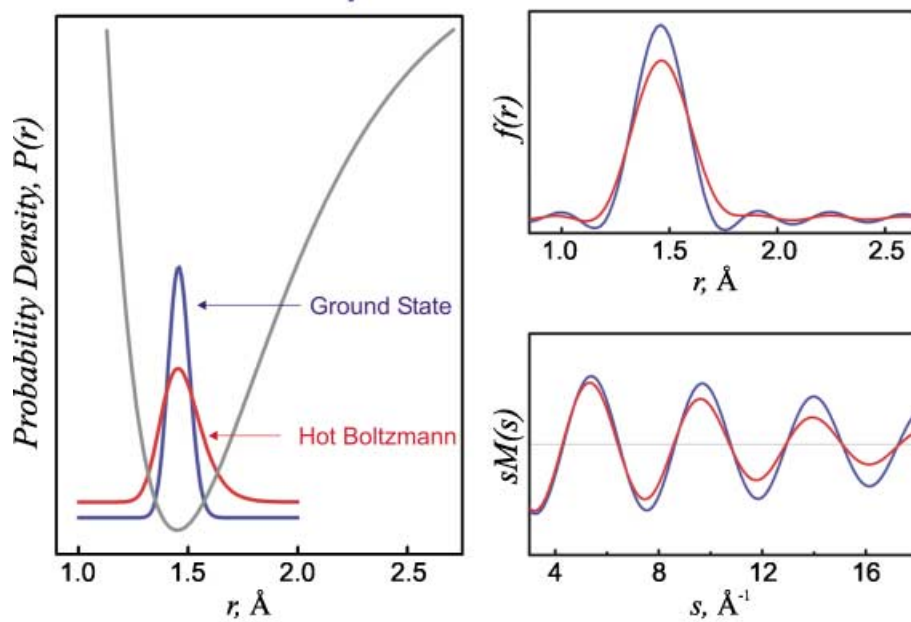
where μ is the reduced mass, ν is the vibrational frequency, k is the *Boltzmann* constant, and T is the vibrational temperature. In the limit of high energy, l_h scales as the square root of the vibrational temperature. In contrast to this thermal (*Boltzmann*) limit where the structures are near equilibrium, structures far from equilibrium would result if the system were created with inverted (non-*Boltzmann*) distributions.

Fig. 24 shows our calculations for the case where wave packets are produced with Gaussian energy distributions at different mean energies, which, in turn, give rise to the corresponding probability densities in the long-time limit. Significantly inverted populations would lead to a clear bifurcation of the internuclear density, inducing splitting and shifting of peaks in the $f(r)$ curve. However, in the case where these non-*Boltzmann* populations occur at relatively low energies in the potential well, the density bifurcation becomes narrower, and the $f(r)$ curve may not display shifted peaks, but would exhibit increased damping – thus mimicking *Boltzmann* distributions albeit with exceptionally high l values. These concepts of enhanced damping and shifted bond distances, shown here for a molecule with a single bond far from equilibrium, are directly relevant to complex molecular structures where energy redistribution may or may not be complete, and where certain bonds determine the reaction coordinate.

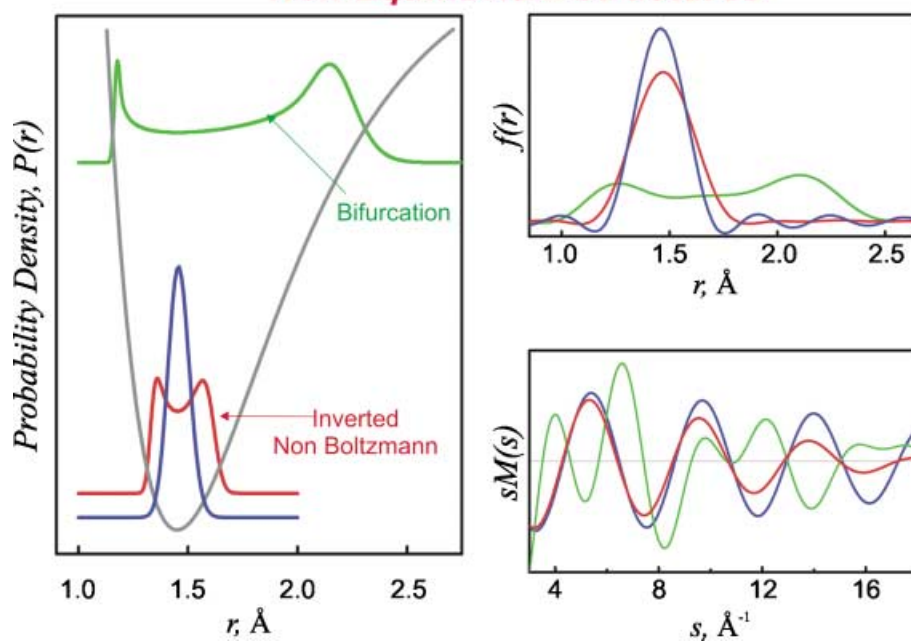
In what follows, we discuss the UED determination of non-equilibrium structures of types I and II. UED Studies of transient structures for three cyclic hydrocarbons at high internal energies reveal markedly different structural behavior [38][42]. For cyclohepta-1,3,5-triene (CHT), excitation results in the formation of hot ground-state structures (*Scheme 4*) with bond distances similar to those of the initial structure (non-equilibrium, Type I). In contrast, cyclohexa-1,3-diene (CHD) undergoes a ring-opening reaction (*Scheme 5*) to form hexa-1,3,5-triene (HT), while cycloocta-1,3,5-triene (COT3) opens the ring (*Scheme 6*) to form octa-1,3,5,7-tetraene (OT) – both in their far-from-equilibrium states, as manifested by an inverted population in the

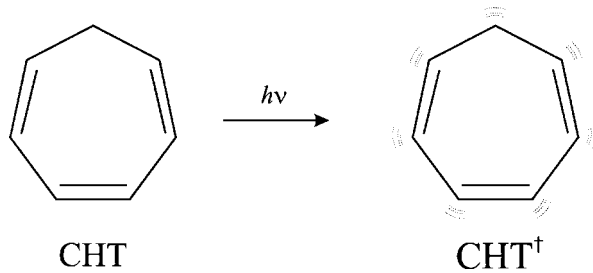
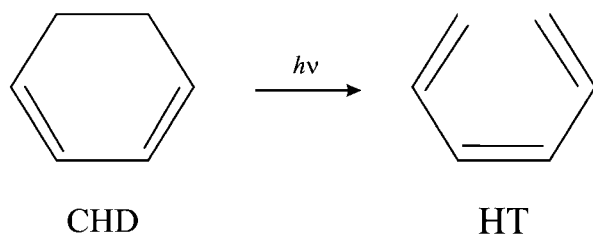
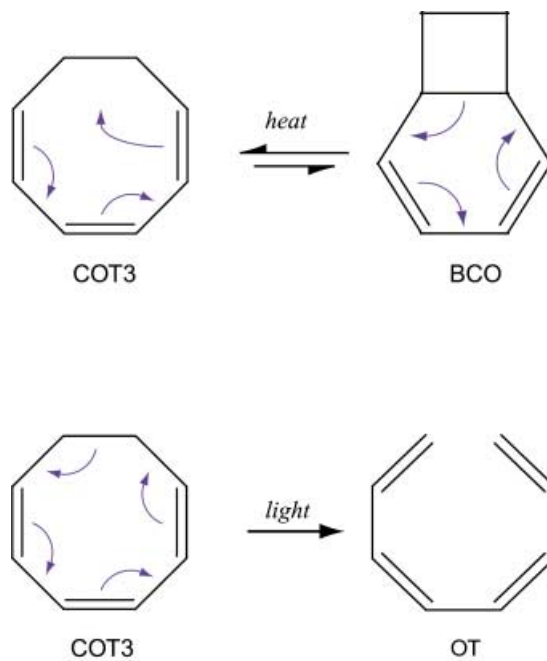
Fig. 24. Calculated diffraction curves for a single bond in two regimes: equilibrium structure and non-equilibrium structure. Shown on the left are probability densities of the single bond distance, and on the right are the resulting $sM(s)$ and $f(r)$ curves. *Top:* Thermal (*Boltzmann*) vibrational population at ground-state (*blue*) and at a much higher temperature (*red*). Increased temperature results in broadening of the $f(r)$ curve and damping of the $sM(s)$ curve. *Bottom:* Inverted (non-*Boltzmann*) vibrational populations modeled with Gaussian distributions. Low-lying inverted populations (*red*) will cause broadening of the $f(r)$ curve and damping of the $sM(s)$ curve similar to the *Boltzmann* case above. Higher-lying populations (*green*) can lead to outright bifurcation of the internuclear density and significant changes in the frequency components of the $sM(s)$ scattering signal.

Equilibrium Structures



Non-Equilibrium Structures



Scheme 4. *Nonradiative Decay of Excited Cyclohepta-1,3,5-triene (CHT) to 'Vibrationally Hot' Ground State*Scheme 5. *Ring Opening of Cyclohexa-1,3-diene (CHD) to Form Hexa-1,3,5-triene (HT)*Scheme 6. *Thermal and Light-Mediated Reactions of Cycloocta-1,3,5-triene (COT3)*

torsional degrees of freedom and by highly elevated vibrational amplitudes (non-equilibrium, Type II).

4.4.2. *Ground-State Structures of CHT, CHD, and COT3.* Fig. 25 shows the ground-state diffraction images for CHT, CHD, and COT3, and their corresponding $f(r)$ curves. Differences between the ring patterns of the three species are evident even in the 2D images, demonstrating the high sensitivity and resolution of our third-generation UED apparatus. Moreover, these three systems have no heavy atoms, and the diffraction, which is from only C- and H-atoms, is sensitive to the increased complexity of these three structures.

The major peaks in the $f(r)$ curves reflect relative populations of various C–C distances in these complex molecules. In CHT, for example, covalent C–C distances occur at ~ 1.4 Å, second-nearest neighbor at ~ 2.5 Å, and third-nearest neighbor at ~ 3.0 Å. The $f(r)$ curve for CHD (with one less C-atom in the ring) clearly shows much lower density of third-nearest neighbor C \cdots C distances compared to CHT, in good agreement with results obtained with conventional electron diffraction [110][111]. Fig. 26 shows the refined ground-state structures of CHT and CHD, along with the best-fit bond distances and angles, together with theoretical predictions.

4.4.3. *Thermal Cope Rearrangement of COT3.* In the case of COT3, two species – COT3 and bicyclo[4.2.0]octa-2,4-diene (BCO) – co-exist in the ground-state, and it has been shown [112] that above 100 °C, both species rapidly interconvert thermally by an electrocyclic Cope rearrangement (Scheme 6). Both structures of COT3 and BCO are observed in our diffraction data (Fig. 25). A series of least-squares refinements were performed on the relative fractions of COT3 and BCO structures, and we obtained a global minimum with a 73.3:26.7 COT/BCO ratio at 433 K, surprisingly in good agreement with the ratio predicted by the results of chromatographic analysis (78.8:21.2) [112]. The DFT-derived COT3 structure as a starting point also gave a good fit with the experiment; an even better fit was obtained through further (partial) refinement of the COT3 structural parameters (Fig. 26), as evidenced by the reduced residual $sM(s)$ curve (not shown).

The peaks in the radial distribution curve $f(r)$ (Fig. 25) show contributions from both ground-state structures, with covalent C–H and C–C distances at ~ 1.1 and ~ 1.4 Å, second nearest-neighbor C \cdots H and C \cdots C distances at ~ 2.2 and ~ 2.6 Å, and third and fourth nearest-neighbor distances at ~ 2.7 to 5 Å, respectively. From the molecular structure obtained for COT3 (Fig. 26), we conclude that the overall conformation of COT3 is ‘twist-boat’ with C_1 symmetry. The isolated molecular structure of COT3, determined by UED for the first time, represents the basis for comparison with solution-phase NMR conformational studies [113], as well as the theoretical predictions from our laboratory and those previously reported in the literature [113][114] (for details, see [42]).

4.4.4. *Structural Dynamics of CHT.* Upon excitation, CHT undergoes an ultrafast hydrogen shift [115–118], but with subsequent reformation of CHT at high internal energy (Scheme 4). Except for their relative intensities, all the transient-only $sM(t; s)$ curves were nearly indistinguishable indicating that the structure of hot CHT remains unchanged within our time resolution. Fig. 27 shows the experimental $sM(s)$ curve averaged from 75 to 400 ps, along with theoretical curves with the same internuclear distances as those of the initial structure, but with varying l values. It is evident that the

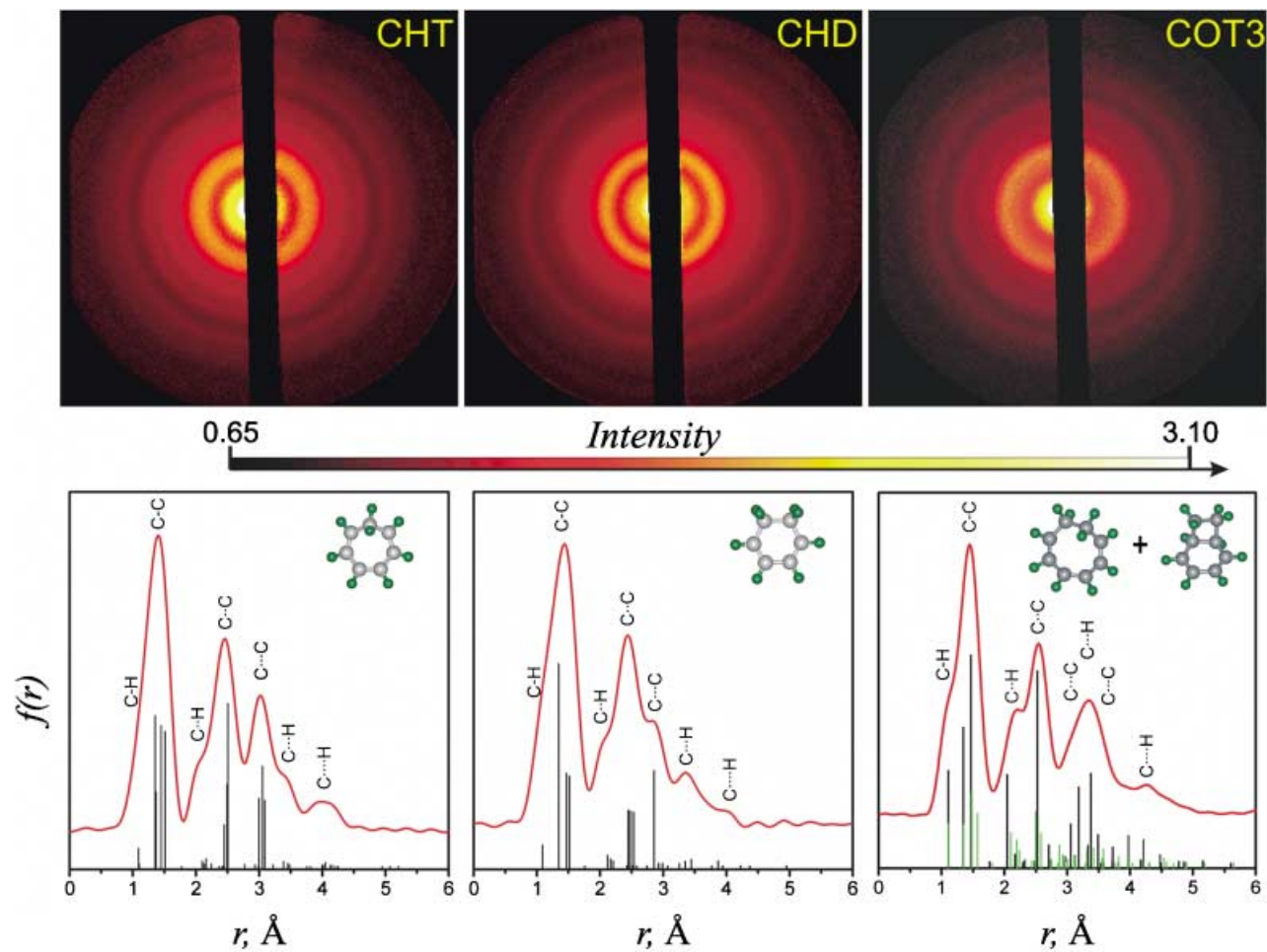


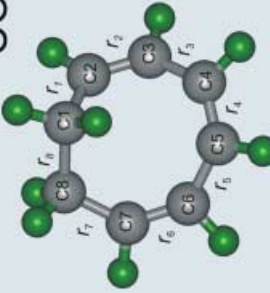
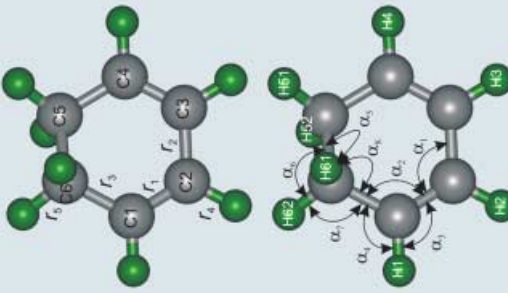
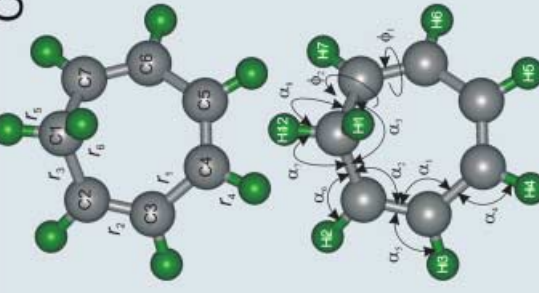
Fig. 25. Observed ground-state diffraction images and corresponding $f(r)$ curves for CHT, CHD, and COT3. The major bond distances (covalent C–C, second nearest-neighbor C··C, and third nearest-neighbor C···C) are shown above the corresponding $f(r)$ peaks. In the case of COT3, there are two structures that are in thermal equilibrium in the ground state (see text).

experimental curve is significantly more damped than the theoretical curve (for the initial structure) at 403 K, thus establishing the ‘hotness’ of product CHT. If the initially deposited energy (107 kcal/mol) were equipartitioned among the CHT modes [119] with a *Boltzmann* distribution within their vibrational levels (see *Fig. 24*), the molecule would have an internal temperature of *ca.* 2200 K (per mode). However, the poor fit of this thermalized model with our experimental data precludes *Boltzmann* vibrational distributions.

A far better agreement is obtained between experiment and theory with l values whose mean is nearly three times that at equilibrium, indicating a non-*Boltzmann* distribution in the vibrational levels. This dramatic increase in the vibrational amplitudes compared to those resulting from a *Boltzmann* assumption suggests that the hot (product) structure can be characterized by a ‘negative temperature’, wherein the upper vibrational levels have higher population than the lower levels. Note the similarity in frequency components between the theoretical $sM(s)$ curve for the equilibrium structure (at 403 K) and the experimental curve (*Fig. 27*), indicating that internuclear distances (in the product) are similar to those at equilibrium – in turn, implying nearly complete energy redistribution. Thus, the near-equilibrium distances in hot CHT and the elevated mean amplitudes of vibration represent a type-I non-equilibrium (non-*Boltzmann*) structure, as per the classification detailed above. For fragment diatomic molecules, the diffraction signature of non-*Boltzmann* distributions has been reported by *Ischenko et al.* [120].

Previous ultrafast spectroscopic studies of the CHT reaction (see, *e.g.*, [116]) have suggested that conical intersections are responsible for the ultrafast formation of product in tens to hundreds of femtoseconds. However, our structural dynamics studies indicate that the hot structure forms on a timescale of ~ 16 ps (*cf. Fig. 30*). This longer timescale suggests that the dynamics in the region towards the final product is different from the initial dynamics of the parent, and that avoided crossing, energy redistribution, and longer-lived trajectories [121] on the excited surface must be considered for understanding the population change with time. This is not surprising as other studies on the femtosecond timescale (see, *e.g.*, [122][123]) have shown the existence of a distribution of femtosecond and picosecond trajectories as molecules traverse a complex energy landscape. If all trajectories were on the femtosecond timescale, and we were merely observing picosecond energy redistribution, our $sM(s)$ curves would have revealed structural changes as a function of time. It should be noted that UED probes the changes of *all* nuclear coordinates, and, therefore, the dynamics reported here are directly relevant to global structural changes in the molecule. In contrast, spectroscopic studies reported for the gas phase (femtoseconds) [116] and condensed phase (picoseconds) [124] monitor state populations. The roles of the solvent and intramolecular relaxation must be disentangled before direct comparisons can be made with our results of the isolated reaction dynamics.

4.4.5. *Structural Dynamics of CHD.* In reactive systems, where bonds are broken and formed, the partitioning of energy may result in its localization in certain bonds associated with the reaction coordinate. Indeed, we observed incomplete energy partitioning even up to 400 ps in hot HT, formed by the ultrafast ring opening of CHD [125–128] (*Scheme 5*). *Fig. 28* shows the evolution of $f(r)$ curves for the ring-opening reaction of CHD. The transient-only HT diffraction curves were significantly damped

COT3	CHD	CHT
 <p>Distances</p> <ul style="list-style-type: none"> $r_1(\text{C1-C2}) = 1.464 \pm 0.040$ (1.502) $r_2(\text{C2-C3}) = 1.321 \pm 0.025$ (1.339) $r_3(\text{C3-C4}) = 1.483 \pm 0.077$ (1.458) $r_4(\text{C4-C5}) = 1.367 \pm 0.055$ (1.348) $r_5(\text{C5-C6}) = r_5 + 0.0087$ (1.467) $r_6(\text{C6-C7}) = r_2 + 0.0048$ (1.344) $r_7(\text{C7-C8}) = r_1 + 0.0005$ (1.503) $r_8(\text{C8-C1}) = 1.518$ (1.537) $r(\text{C-H})^{\text{sp}^3} = 1.072 \pm 0.033$ (1.096) $r(\text{C-H})^{\text{sp}^2} = 1.113 \pm 0.018$ (1.088) <p>Angles</p> <ul style="list-style-type: none"> $\alpha_1(\text{C1-C2-C3}) = 129.2 \pm 5.3$ (125.2) $\alpha_2(\text{C2-C3-C4}) = 122.8 \pm 2.1$ (125.6) $\alpha_3(\text{C3-C4-C5}) = 128.2 \pm 7.5$ (128.3) $\alpha_4(\text{C4-C5-C6}) = 133.5 \pm 9.8$ (131.7) $\alpha_5(\text{C5-C6-C7}) = 132.0 \pm 10$ (134.8) $\alpha_6(\text{C6-C7-C8}) = 134.1 \pm 6.8$ (132.6) $\alpha_7(\text{C7-C8-C1}) = 117.6$ (116.5) $\alpha_8(\text{C8-C1-C2}) = 119.1$ (113.5) $\phi_1(\text{C1C2-C3C4}) = 20 \pm 22$ (2.3) $\phi_2(\text{C2C3-C4C5}) = 37 \pm 39$ (39.8) $\phi_3(\text{C3C4-C5C6}) = 3 \pm 41$ (6.9) $\phi_4(\text{C4C5-C6C7}) = -36 \pm 15$ (-39.3) $\phi_5(\text{C5C6-C7C8}) = -17 \pm 48$ (-4.9) $\phi_6(\text{C6C7-C8C1}) = 27$ (1.6) 	 <p>Distances</p> <ul style="list-style-type: none"> $r_1(\text{C1-C2}) = 1.310 \pm 0.002$ (1.342) $r_2(\text{C2-C3}) = 1.445 \pm 0.010$ (1.468) $r_3(\text{C1-C6}) = 1.525 \pm 0.053$ (1.512) $r_4(\text{C2-H2}) = 1.032 \pm 0.003$ (1.087) $r_5(\text{C6-H62}) = 1.134 \pm 0.004$ (1.095) <p>Angles</p> <ul style="list-style-type: none"> $\alpha_1(\text{C1-C2-C3}) = 120.0 \pm 1.1$ (120.7) $\alpha_2(\text{C2-C1-C6}) = 120.7 \pm 0.7$ (120.4) $\alpha_3(\text{H1-C1-C2}) = 123.0 \pm 4.5$ (120.8) $\alpha_4(\text{H1-C1-C6}) = 120.0 \pm 7.8$ (118.7) $\alpha_5(\text{C5-C6-H61}) = 106.6 \pm 11.1$ (103.3) $\alpha_6(\text{C5-C6-H62}) = 113.9 \pm 7.3$ (113.6) $\alpha_7(\text{C1-C6-H62}) = 110.5 \pm 9.1$ (110.9) $\alpha_8(\text{C1-C6-H61}) = 107.3 \pm 4.7$ (108.3) 	 <p>Distances</p> <ul style="list-style-type: none"> $r_1(\text{C3-C4}) = 1.429 \pm 0.009$ (1.47) $r_2(\text{C2-C3}) = 1.382 \pm 0.008$ (1.34) $r_3(\text{C1-C2}) = 1.523 \pm 0.004$ (1.52) $r_4(\text{C4-H4}) = 1.095 \pm 0.012$ (1.089) $r_5(\text{C1-H12}) = 1.104 \pm 0.113$ (1.093) $r_6(\text{C1-H1}) = 1.117 \pm 0.080$ (1.098) <p>Angles</p> <ul style="list-style-type: none"> $\alpha_1(\text{C2-C3-C4}) = 122.5 \pm 3.0$ (125.6) $\alpha_2(\text{C1-C2-C3}) = 119.6 \pm 2.3$ (122.0) $\alpha_3(\text{C2-C1-C7}) = 117.0 \pm 1.7$ (108.2) $\alpha_4(\text{C3-C4-H4}) = 122.6 \pm 2.7$ (116.4) $\alpha_5(\text{C2-C3-H3}) = 116.6 \pm 5.9$ (117.8) $\alpha_6(\text{C1-C2-H2}) = 113.1 \pm 8.8$ (118.5) $\alpha_7(\text{C2-C1-H12}) = 101.8 \pm 9.4$ (110.3) $\alpha_8(\text{C7-C1-H12}) = 111.3 \pm 8.3$ (98.4)

Non-Equilibrium CHT Structure

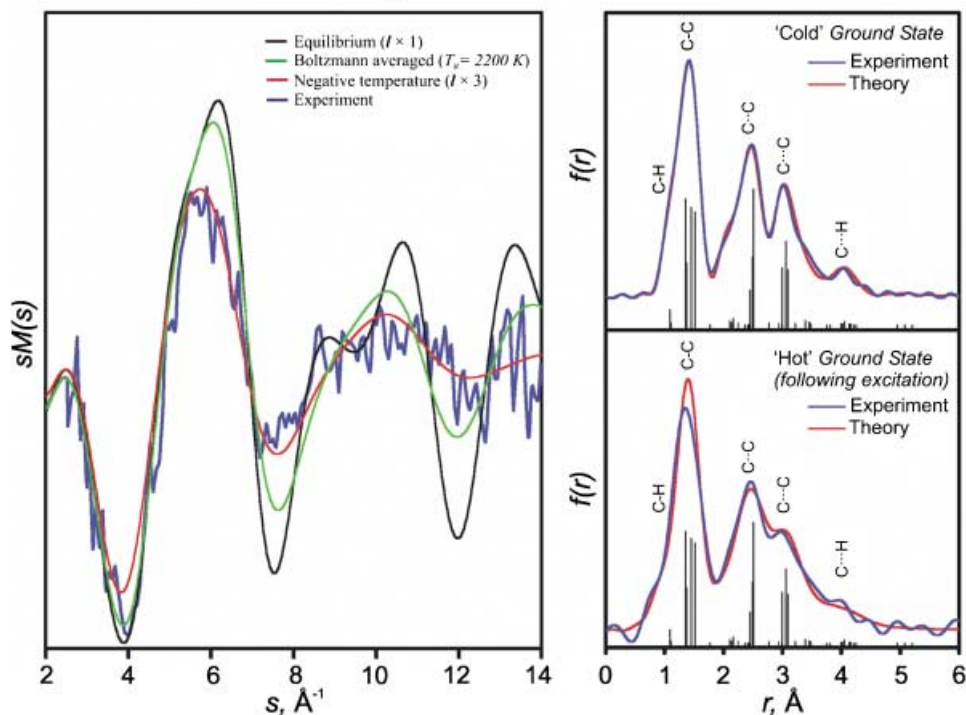


Fig. 27. Non-equilibrium 'negative temperature' in CHT. The left panel shows the transient-only $sM(s)$ curves, and the right panel shows the influence of high vibrational temperature on the ground-state and transient-only $f(r)$ curves. Left: The (blue) experimental curve averaged from 75 to 400 ps is shown, along with corresponding theoretical curves for the equilibrium structure at 403 K (black), the Boltzmann-averaged structure at ca. 2,200 K (green), and a non-Boltzmann structure with a mean l value nearly three times that at 403 K (red). For details of structural analysis, see text. Right: The $f(r)$ curves for the initial structure at 403 K (top) and the hot CHT structure at a negative temperature (bottom). Note the significant broadening of the $f(r)$ peaks in the hot structure compared to the cold ground state; only l was adjusted.

at all time points (manifested as peak broadening in the $f(t; r)$ curves), indicating the vibrationally hot nature of the product structure; however unlike CHT, new peaks appear in $f(r)$. Shown below the experimental data in Fig. 28 are theoretical $f(r)$ curves for three hot conformers of HT (labeled cZc , cZt , and tZt with respect to the conformation of torsion angles about the C–C single bonds). Close inspection of the experimental $f(t; r)$ curves reveals greater similarity to the theoretical cZc curve than to

- ← Fig. 26. Refined ground-state structures of CHT, CHD, and COT3. The refined bond distances and angles for the three systems are shown, along with the DFT values indicated in parentheses. Distances are in Å, and angles are in degrees. Note that some uncertainties of the COT3 fit are somewhat larger than the instrumental limit of ~ 0.01 Å for ground-state structures, due to correlation effects among fitting parameters in the twist-boat structure. For COT3, note that r_5 , r_6 , and r_7 were not fit, but were obtained using the dependency predicted by DFT; also r_8 , α_7 , α_8 , and ϕ_6 were not independently refined, but were derived from other best-fit parameters.

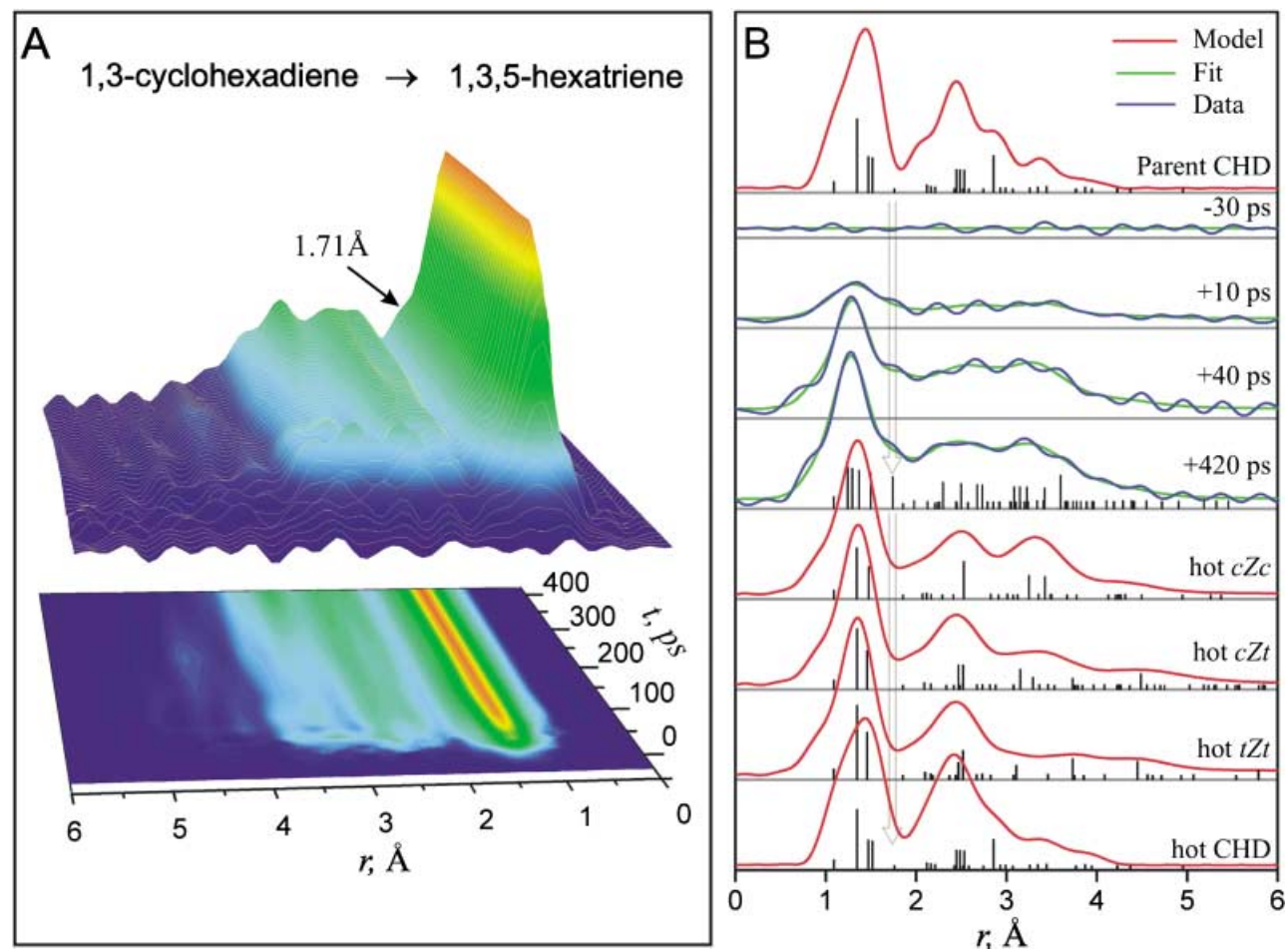


Fig. 28. Time-resolved formation of hot HT structures after the ring opening of CHD. *A*) Fourier-filtered $f(t; r)$ curves showing product evolution; note the shoulder at ~ 1.7 Å. *B*) *Top*: DFT $f(r)$ curve (red) for the CHD parent structure at 403 K. *Middle*: comparison of selected experimental transient-only $f(t; r)$ curves (blue) with corresponding structural fits (green). *Bottom*: DFT $f(r)$ curves (red) for the three HT conformers (extrapolated to 2,100 K) and for hot CHD (extrapolated to 2,400 K) shown for comparison. The vertical arrows indicate the peak at ~ 1.7 Å, which is present in all experimental curves, but which is absent in the DFT $f(r)$ curves of the three HT conformers.

that of the lower-energy *tZt* conformer. Furthermore, an anomalous peak at ~ 1.7 Å can be seen as a shoulder in all the experimental $f(t; r)$ curves; the presence of this peak – which is ~ 0.2 Å away from expected equilibrium C–C distances – was found to be reproducible in repeated diffraction experiments.

Monte Carlo least-squares refinement of the structural parameters yielded a HT molecular structure that showed no *tZt* character, but consistently manifested a configuration intermediate between *cZc* and *cZt* – far removed from a thermally equilibrated conformer distribution of *ca.* 41% *tZt*, *ca.* 45% *cZt*, and *ca.* 14% *cZc* at 2100 K (estimated from *ab initio* calculations of the conformer energies). Moreover, the ~ 1.7 -Å peak observed in the $f(t; r)$ curves was assigned to one C–C single bond in HT – a highly non-equilibrium value for a C–C internuclear separation. This remarkable departure from the predicted equilibrium conformation, together with the unusual C–C bond length, confirms the far-from-equilibrium (non-equilibrium, type II) nature of the HT structure. The refined HT structure, along with the bond distances and angles, are shown in *Fig. 29*.

The hot HT structure is formed with a time constant of ~ 32 ps (*Fig. 30*) and remains virtually unchanged over the course of the experiment (400 ps). The persistence of this far-from-equilibrium structure indicates that unlike CHT, energy partitioning within HT is slow with respect to both the rate of product formation and the timescale of the UED experiment. The existence of a *cZc*-like conformation clearly indicates an inverted population on the potential-energy surface (projected along the coordinate of torsional motion), with significant density at the classical turning points. Moreover, the ~ 1.7 -Å distance assigned to a C–C bond would require *ca.* 15 kcal/mol of the available *ca.* 90 kcal/mol to be deposited in that C–C bond (assuming a simple *Morse* oscillator model) – providing further evidence for an inequitable partitioning of energy. Note that if energy partitioning were indeed complete, then each of the 36 modes in HT would have *ca.* 2.5 kcal/mol.

Co-existence of the two structural features – an inverted torsional conformation and a stretched C–C bond – over time strongly suggests a long-lived, low-frequency hybrid motion comprised of both torsion and asymmetric stretching of the C-skeleton. Conceptually, one may picture that as the molecule oscillates between the turning points of the potential well, the stretched C–C distance is shifted continuously from one C–C bond to another and at the turning points, the torsional energy is partially stored in the C–C bond stretch. That this far-from-equilibrium structure lasts for over 400 ps suggests a bottleneck in energy transfer from the inferred hybrid motion to other (higher-frequency) modes, after the initial energy deposition. This energy localization could result from a mismatch in the frequencies of the coherent modes compared to all other modes (at these high internal energies). It is interesting to note here that torsional modes of this type have been isolated in dynamical calculations of polypeptides [129]; we shall discuss below another case (COT3) relevant to this behavior.

Ultrafast spectroscopic studies of the CHD ring-opening reaction have suggested contrasting timescales for the formation of the HT product – tens to hundreds of femtoseconds [126–128] and 6 ± 1 ps [125]. The presence of two simultaneously active conical intersections has been invoked to rationalize the femtosecond timescales [130]. As with CHT discussed above, our structural investigations reiterate the importance of

Refined Ring-Opened Structure of HT

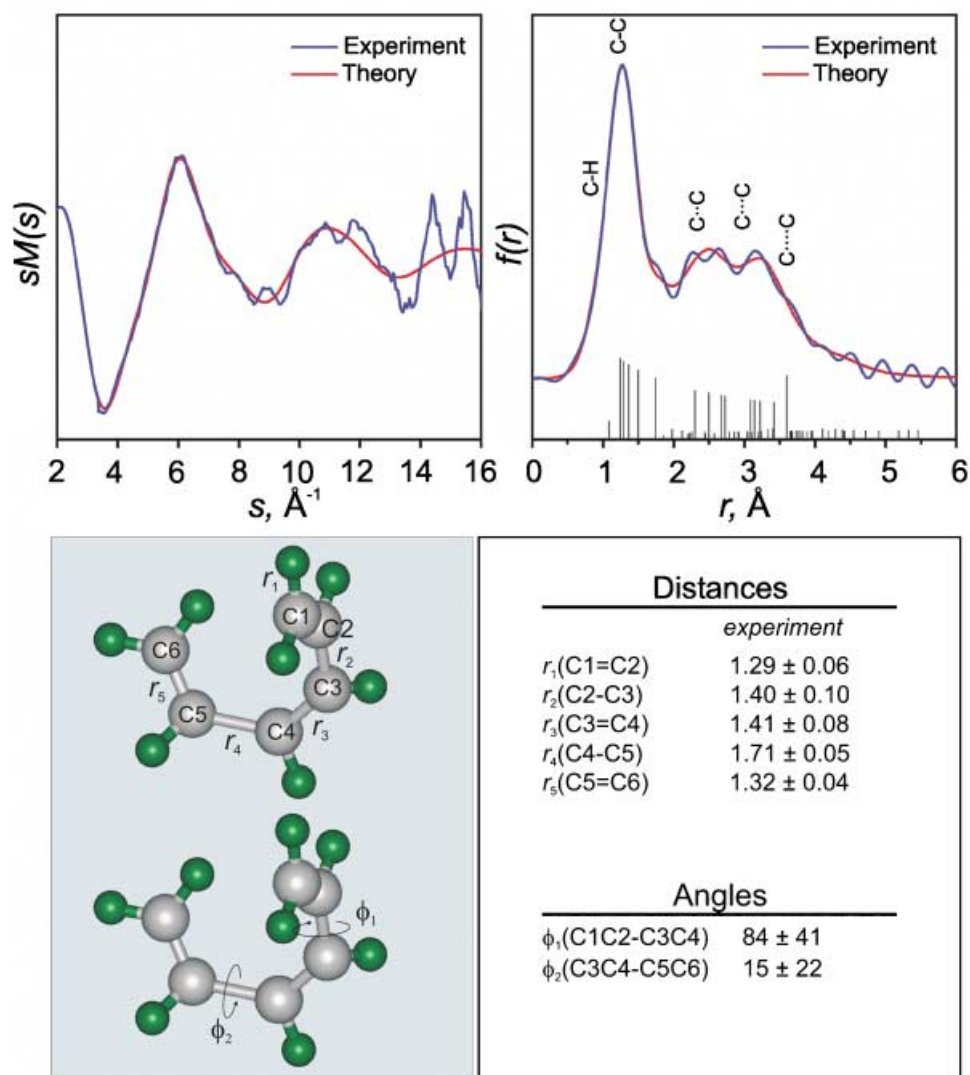


Fig. 29. Structure refinement of ring-opened HT structure. Shown on top are the experimental $sM(s)$ and $f(r)$ curves, along with the best-fit theoretical curves. At the bottom is shown the refined HT structure, with its corresponding structural parameters. Distances are in Å, and angles are in degrees. The structural parameters were obtained by averaging over the Monte Carlo search results over all time points. The standard deviations represent the spread of the minimum basin in configuration space. Note the elongated (~ 1.7 Å) C(4)–C(5) bond distance in the non-equilibrium transient HT structure.

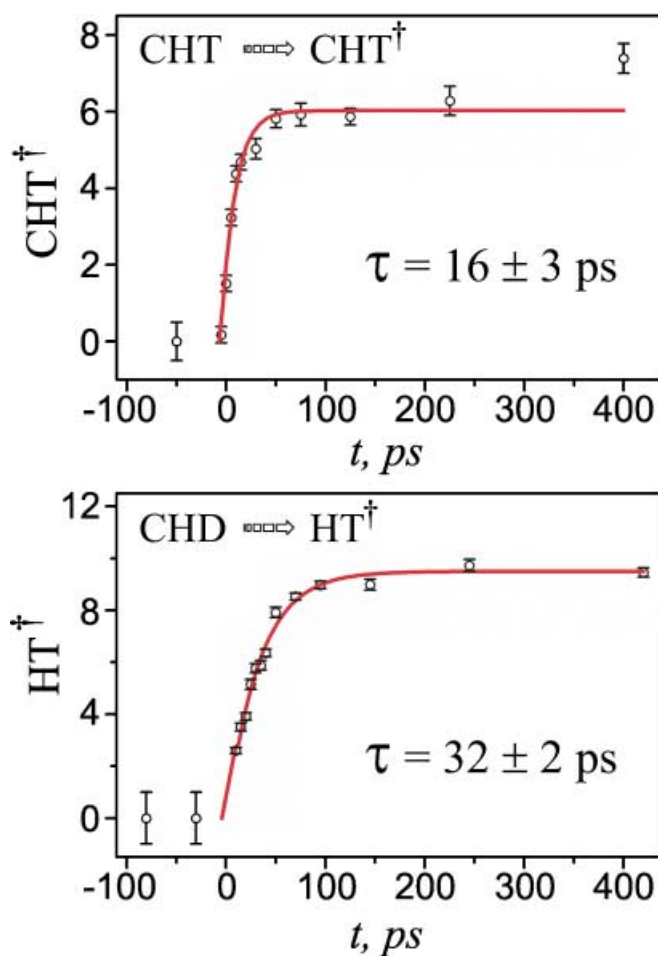


Fig. 30. Evolution of transient structure populations in CHT and CHD. The time constant for the structural change in CHD is twice that in CHT.

long-lived (ps) trajectories in the formation of transient structures. It is interesting to note that, while we found virtually no contribution from hot CHD in the HT product (despite our sensitivity to hot 'parent' structures in CHT), static condensed-phase experiments have reported a 60:40 branching ratio for the CHD reformation/ring-opening pathways. This near-absence of hot parent structures, along with the long time observed by UED for ring opening, signifies the crucial role played by the solvent in redirecting the fate of the reaction. For instance, the increased steric hindrance to ring opening in the solvent may favor the reformation of CHD over ring opening. Moreover, the solvent can induce slight perturbations in the relative positions of the potential-energy surfaces, which can dramatically alter the timescales [121] for reaction in the condensed phase, especially if it involves open structures with conformational changes.

4.4.6. *Structural Dynamics of COT3*. COT3 represented a particularly challenging system to study *via* UED for a variety of reasons, including the number of different structures potentially involved, the lack of symmetry in most of these structures, the large number of atoms in each species, and the complex landscapes of the transient species. In this case, COT3 undergoes electrocyclic ring opening to form OT, as shown in *Scheme 6* (for details, see [42]).

The experimental $\Delta sM(s)$ and $\Delta f(r)$ curves for COT3 at +150 ps (with reference to –100 ps) are shown in *Fig. 31*. We considered all structures at the internal energy possible (up to 100 kcal/mol) of the parents (COT3 and BCO) and of transient OT; and found the best agreement when the reaction path is that of ring opening to vibrationally hot OT. In contrast, our fits with the hot ‘parent’ structures (1,3,5-COT3, 1,3,6-COT3, and BCO) were poor. As in the case of pyridine described above, ring opening is evident upon inspection of the data $\Delta f(r)$ curves shown in *Fig. 31 (bottom)* – the negative peaks correspond to the net *loss* of internuclear density (*i.e.*, the loss of covalent ~ 1.5 Å and second ~ 2.6 Å, third ~ 3.2 Å, and fourth nearest-neighbor distances in the parent structures), whereas the positive peaks correspond to a net *gain* in internuclear density (*e.g.*, the formation of new bond pairs at distances greater than 4 Å). Such a diffraction signature is consistent with ring-opening processes that form more extended structures in the transient species.

The high sensitivity of the experiment allowed the examination of the different conformations of transient OT structures (*Fig. 32*) in the UED analysis, and the higher-energy *gauche* structure, so-called *tcGct*, was found to be the best fit. If equilibrium structures were the only ones present at the *Boltzmann* temperature of *ca.* 1900 K (determined by the internal energy), the lower-energy *anti* structures (*tcAct* and *tcAcc*) would be the dominant one(s) (*ca.* 70%), contrary to our findings. Also, the CC and CH vibrational amplitudes for the refined *gauche* structure are increased by an average of ~ 3.1 and ~ 2.3 times the ambient temperature values (at 433 K), corresponding to a $\sim 40\%$ increase over what would be expected for a thermally equilibrated distribution of the excess internal energy over the vibrational degrees of freedom.

To determine the nature of the conformational landscape and to obtain the ensemble-averaged OT structure, we performed a Monte-Carlo/least-squares refinement of the three C–C bonds and the corresponding dihedral angles. Our search in configuration space began at the all-folded OT (*ccGcc*) structure, freeing the parameters to change ± 0.25 Å for the C–C bonds and $\pm 180^\circ$ for the dihedral angles. Further least-squares refinements were applied to the local minimum structures and the results of these fits are very good, as shown in *Fig. 32*.

The successful determination of these complex structures with multiple conformations was finally confirmed from the transient-only curves. *Fig. 32, A*, shows the comparison of the experimental and theoretical $f(r)$ of these transient-only curves, obtained using the structural parameters of the first minimum of the Monte-Carlo/least-squares refinements. *Fig. 32, B*, shows the structures of five selected minima superimposed for comparison, as well as a table summarizing the values of the refined parameters. The structures of all minima clearly show considerable *gauche tcGct/ccGct* character and not the *anti* equilibrium OT structures, indicating an inverted (non-*Boltzmann*) torsional distribution. The non-*Boltzmann* behavior is also revealed in the disparities of the torsional motions and in the corresponding C–C distances. We found

Ring Opening Reaction of COT3

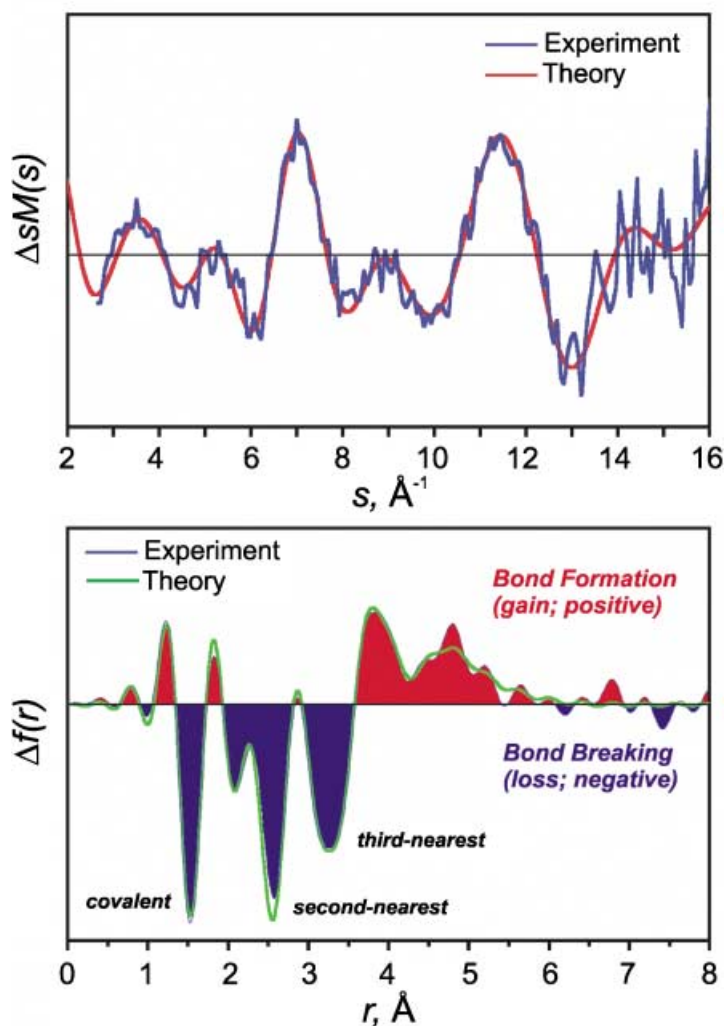
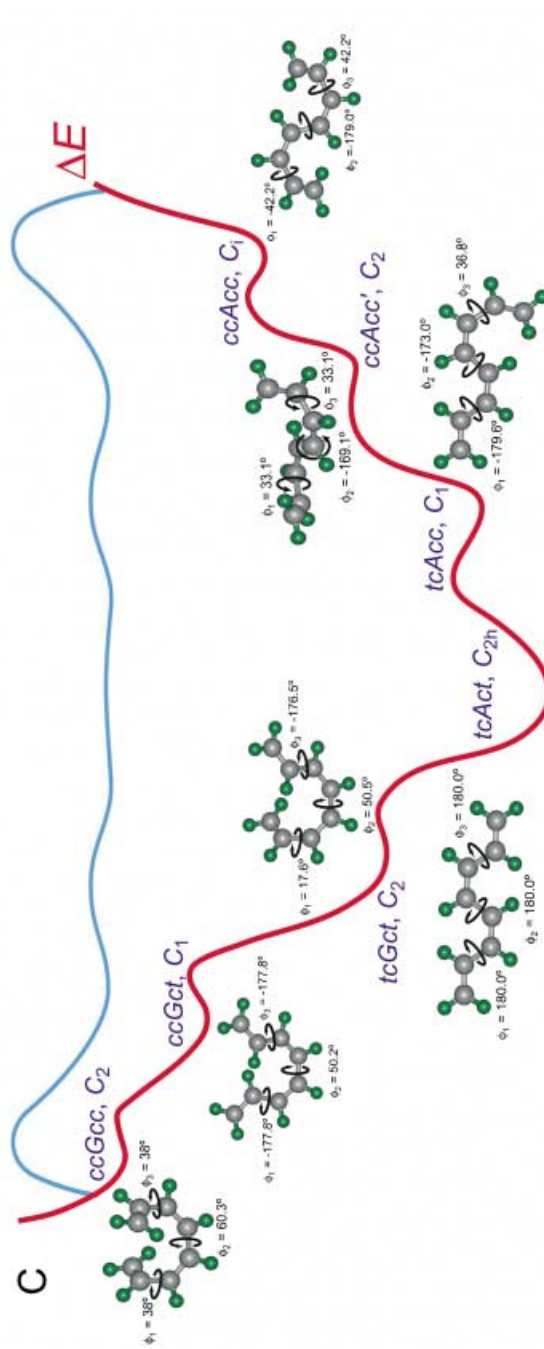
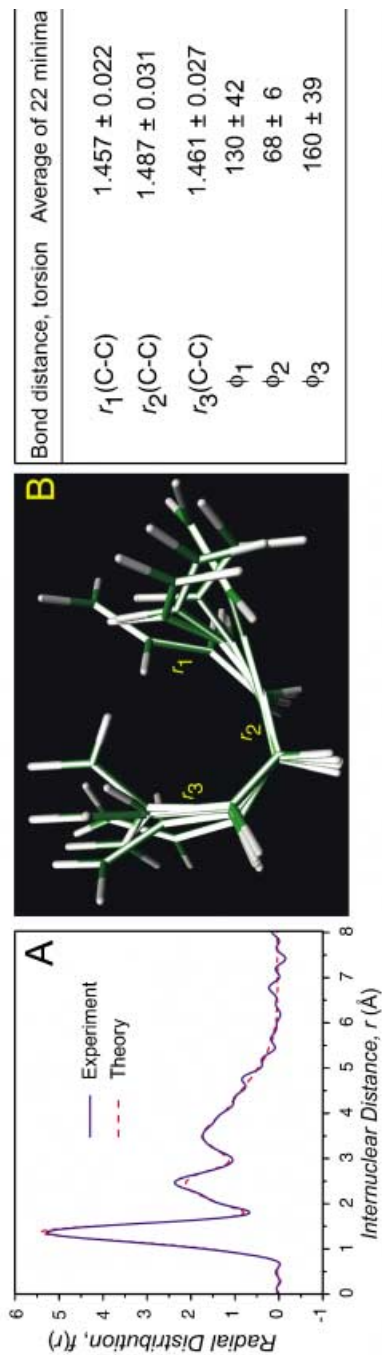


Fig. 31. COT3 Difference curves. Top: Comparison of experimental $\Delta sM(s)$ curve (blue) obtained at +150 ps with the corresponding theoretical curve (red) obtained using the structural parameters of the first minimum of the Monte-Carlo/least-squares refinements of *gauche* OT. Bottom: Corresponding experimental $\Delta f(r)$ curve (blue); the blue highlighted regions represent net depletion – bond breaking – of internuclear pairs, whereas the red regions correspond to net gain – bond-formation – of internuclear pairs.

that the two terminal torsions (ϕ_1, ϕ_3) in the side groups of OT have broad distributions ($\pm 40^\circ$); in contrast, the torsion at the central C–C bond (ϕ_2), which establishes the *gauche* character of OT, is rather confined ($\pm 6^\circ$). Correspondingly, the central C–C bond distance (r_2) was found to be lengthened to $\sim 1.487 \text{ \AA}$, while all the rest C–C bonds remain at (near) equilibrium distances.

Complex Energy Landscape of Transient OT Conformations



These far-from-equilibrium OT structures reflect large-amplitude torsional motions comprised of ϕ_1 , ϕ_3 , and r_2 , which persist for long times, and which are not in thermal equilibrium with the rest of molecular motions, indicating a bottleneck in energy redistribution between these very-low-frequency modes and the surrounding thermal bath modes. These discoveries have ramifications in the studies of macromolecular dynamics since torsional modes of this type could be important in the first steps of protein folding [129]. Unlike the timescale of a single bond (fs), the longer times involved in these torsions (tens to hundreds of picoseconds) render them significant for the biological function of macromolecules.

The UED studies on CHT, CHD, and COT3 reviewed here highlight the capability of UED to capture molecular structures in non-equilibrium configurations. While non-thermal effects have been previously reported, UED has, for the first time, directly isolated and determined such far-from-equilibrium structures – in terms of both vibrational amplitudes and bond distances – in isolated complex molecules. The structural dynamics of these complex hydrocarbons underscore the importance of the following issues: *i*) the critical influence of structural changes on energy redistribution and on persistence of certain bond motions; *ii*) the nature of the nascent structure(s) born *en route* to the final product and the associated coherent dynamics; and *iii*) the direct relevance of structural changes associated with bond breaking and making in understanding the disparities of measured timescales for state population dynamics in the condensed phase.

4.5. From Carbenes to Organometallics

We end this chapter with two more applications, spanning a small reactive carbene, CF_2 , and a large organometallic intermediate, $\text{Fe}(\text{CO})_4$.

4.5.1. *Carbenes*. UED Studies elucidated the difluorocarbene (CF_2) structure resulting from the dissociation of difluorodiiodomethane (CF_2I_2) [32]. The experimental and theoretical $f(r)$ curve for the ground-state CF_2I_2 and the $\Delta f(r)$ curves at different delay times are shown in Fig. 33. The refined ground-state structure of the reactant CF_2I_2 is also shown; agreement between UED results and those of conventional GED [131] is very good, considering the relatively lower flux of our electron pulses in UED-2. There is no temporal evolution after +12 ps. Since no CF_2I

← Fig. 32. *Transient-only structures of OT*. A) Comparison of theoretical (red) and experimental (blue) transient-only $f(r)$ curves for the diffraction signal at +150 ps; the theoretical curve was obtained using the structural parameters of the first minimum of the Monte-Carlo/least-squares refinements. The standard deviations represent the spread of the minimum basin in configuration space. B) Overlaid skeletal structures for the five selected minima obtained from the Monte-Carlo/least-squares refinement. Corresponding values for the six structural parameters are summarized in the table on the right. C) Equilibrium (*cis,cis*) OT conformer structures obtained *via* DFT, including symmetries and values for single-bond torsional angles. The energy landscape is schematically shown. The nomenclature convention used in the figure corresponds to the OT torsional degrees of freedom as follows: positions 1, 3, and 5 in a given name correspond to torsion around single bonds, whereas positions 2 and 4 correspond to torsion around double bonds (and hence are always 'c' for 'cis' in the conformers of *cis,cis*-OT). Positions 1 and 5 may be denoted 't' (for *trans*) or 'c' (or 'cis'); however, the use of 'A' (*Anti*) and 'G' (*Gauche*) was deemed more appropriate for position 3. The energetics are given in [42].

radical was detected even at the time zero, the estimated bond breakage time for both I-atoms of the CF_2I_2 reactant is less than 4 ps at 307 nm. To determine the transient CF_2 structural parameters, the CF_2I_2 structural parameters were kept fixed at the values obtained in conventional GED [131]. The best-fit internuclear distances C–F and F \cdots F in CF_2 are shown in Fig. 33.

The structure of CF_2 radical has been studied both theoretically and experimentally [132–138]. The equilibrium geometry of both ground state (X^1A_1) and the first excited state (3B_1) of CF_2 , which lies *ca.* 2.42 eV above the ground state, were measured with microwave spectrum [133], UV absorption spectroscopy [132], and laser-induced fluorescence spectroscopy [134]. The internuclear distances C–F and F \cdots F for these two states were determined to be 1.30 and 2.06 Å ($\angle\text{FCF} = 104.9^\circ$) for ground state [132], and 1.325 and 2.29 Å ($\angle\text{FCF} = 119.4^\circ$) for the first excited state [134], respectively. These values are also supported by *ab initio* calculations [134–138]. The internuclear distances of the CF_2 radical (1.30 and 2.06 Å) determined by UED suggest that the CF_2 radicals are in the ground state, following the breakage of the two C–I bonds.

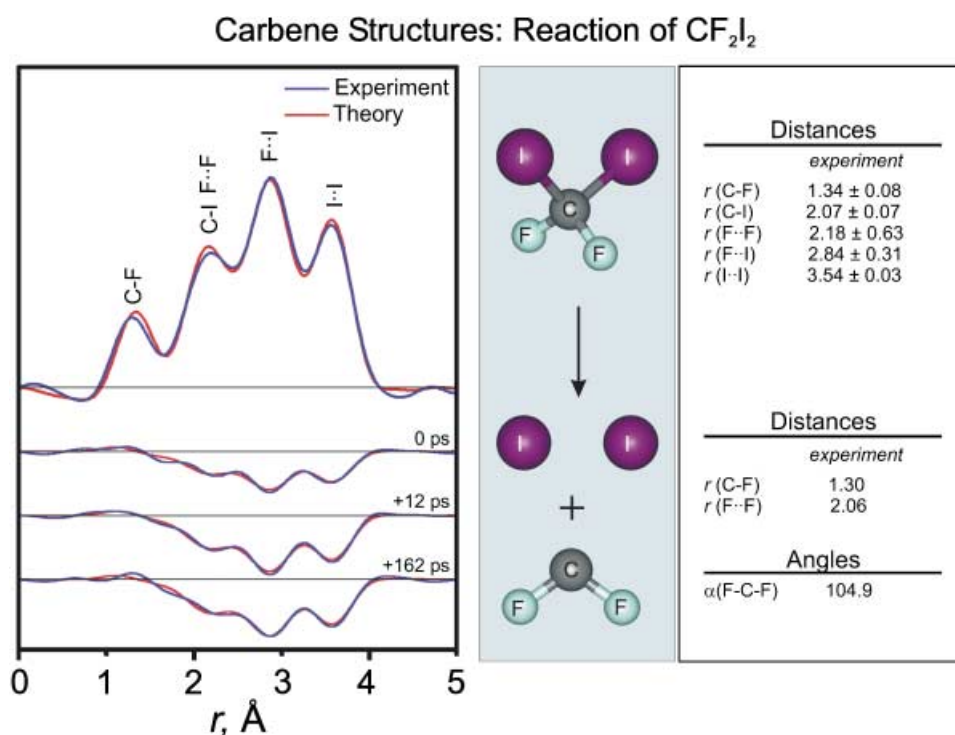


Fig. 33. Structural determination of CF_2 . The left panel shows the experimental and theoretical curves for CF_2I_2 elimination reaction. The curves reflect the loss of internuclear separations in the region of the C–I and I \cdots I bond distances. The right panel shows the refined structures for the parent (CF_2I_2) and product (CF_2), along with the corresponding bond distances and angles. Distances are in Å, and angles are in degrees.

4.5.2. *Organometallics*. In Sect. 4.3, we discussed the structures involved in the $\text{CpCo}(\text{CO})_2$ reaction and, here, we consider the $\text{Fe}(\text{CO})_5$ reaction. Among transition-metal carbonyls, $\text{Fe}(\text{CO})_5$ is one of the most extensively studied molecular systems. Having five CO ligands, a $\text{Fe}(\text{CO})_5$ molecule can dissociate into five different products ($\text{Fe}(\text{CO})_x$, $x = 4, 3, 2, 1, 0$) depending on the excitation wavelength. In these reactions, $\text{Fe}(\text{CO})_4$ is the primary intermediate and serves as a ‘doorway’ molecule for various subsequent reactions [139][140], such as decomposition, recombination with the CO ligand, and coordination with solvent molecules. Elucidating the nature of $\text{Fe}(\text{CO})_4$, including its electronic states and the corresponding molecular geometry, is important for understanding the role of intermediates in the photolysis of transition metal carbonyls.

The UED experiments on $\text{Fe}(\text{CO})_5$ were performed using UED-2 [36]. Fig. 34 shows the experimental $f(r)$ curve at -20 ps and the corresponding theoretical curve with the structural parameters from static gas-phase electron-diffraction study [141]. Our refined ground-state structure of $\text{Fe}(\text{CO})_5$ is also shown, with the Fe–C(axial) distance ~ 1.81 Å, Fe–C(equatorial) ~ 1.82 Å and C–O ~ 1.15 Å – in good agreement with GED values of 1.807, 1.827, and 1.152 Å, respectively. We also observed the strong density of Fe \cdots O pairs at ~ 3.3 Å.

With two-photon excitation at 620 nm, only $\text{Fe}(\text{CO})_4$ (both $^1\text{A}_1$ and $^3\text{B}_2$ states) and $\text{Fe}(\text{CO})_3$ ($^3\text{A}_2$ state only) are energetically possible in the fragmentation reaction of $\text{Fe}(\text{CO})_5$. A fit with these three possible products was performed by floating the fraction of each species, and by using the structural parameters obtained from *ab initio* calculations [142]. The fraction of the singlet $\text{Fe}(\text{CO})_4$, derived from ground-state $\text{Fe}(\text{CO})_5$, was $14 \pm 1\%$, while the combined fraction of the triplet $\text{Fe}(\text{CO})_4$ and triplet $\text{Fe}(\text{CO})_3$ was less than 1%, indicating that the singlet $\text{Fe}(\text{CO})_4$ is the primary product, and the formation of other species is negligible. To trace other possible secondary photofragments, a fit including triplet $\text{Fe}(\text{CO})_2$, triplet $\text{Fe}(\text{CO})$, and Fe was also performed by floating the fraction of each species while keeping their structural parameters fixed at the values obtained from *ab initio* calculations [142]. The resulting total fraction of $\text{Fe}(\text{CO})_2$, $\text{Fe}(\text{CO})$, and Fe was less than 1%, confirming that these secondary products are negligible.

Fig. 35 shows the comparison between the UED data fits with $\text{Fe}(\text{CO})_4$ for the two different reaction pathways. The $\text{Fe}(\text{CO})_4$ structure in the $^1\text{A}_1$ state is very similar to that of $\text{Fe}(\text{CO})_5$ with one equatorial CO removed, while the structure of $\text{Fe}(\text{CO})_4$ in the $^3\text{B}_2$ state is significantly distorted. The C–Fe–C angles of the $^3\text{B}_2$ state are smaller and the Fe–C distances are longer than those of $\text{Fe}(\text{CO})_5$. As shown in Fig. 35, the fit for the $^3\text{B}_2$ state is clearly inferior to that of the $^1\text{A}_1$ state, which gives a good agreement between the experiment and theory. Therefore, $\text{Fe}(\text{CO})_4$ is formed in its singlet excited state, $^1\text{A}_1$, rather than the ground state, $^3\text{B}_2$, at the excitation used. The $^1\text{A}_1$ state $\text{Fe}(\text{CO})_4$ may eventually convert into the $^3\text{B}_2$ state through intersystem crossing, thereby providing a more efficient route for the formation of the $^3\text{A}_2$ state $\text{Fe}(\text{CO})_3$.

A closer examination of the $\Delta f(+200$ ps; -180 ps; $r)$ curve [36] reveals rich details of the structural changes due to the depletion of $\text{Fe}(\text{CO})_5$ and formation of $\text{Fe}(\text{CO})_4$. The two main peaks centered at ~ 2 and ~ 3 Å, respectively, indicate the depletion of the Fe–C and Fe \cdots O internuclear contributions due to the liberation of CO. The shoulders beyond 3.5 Å are due to the reduction of other internuclear contributions,

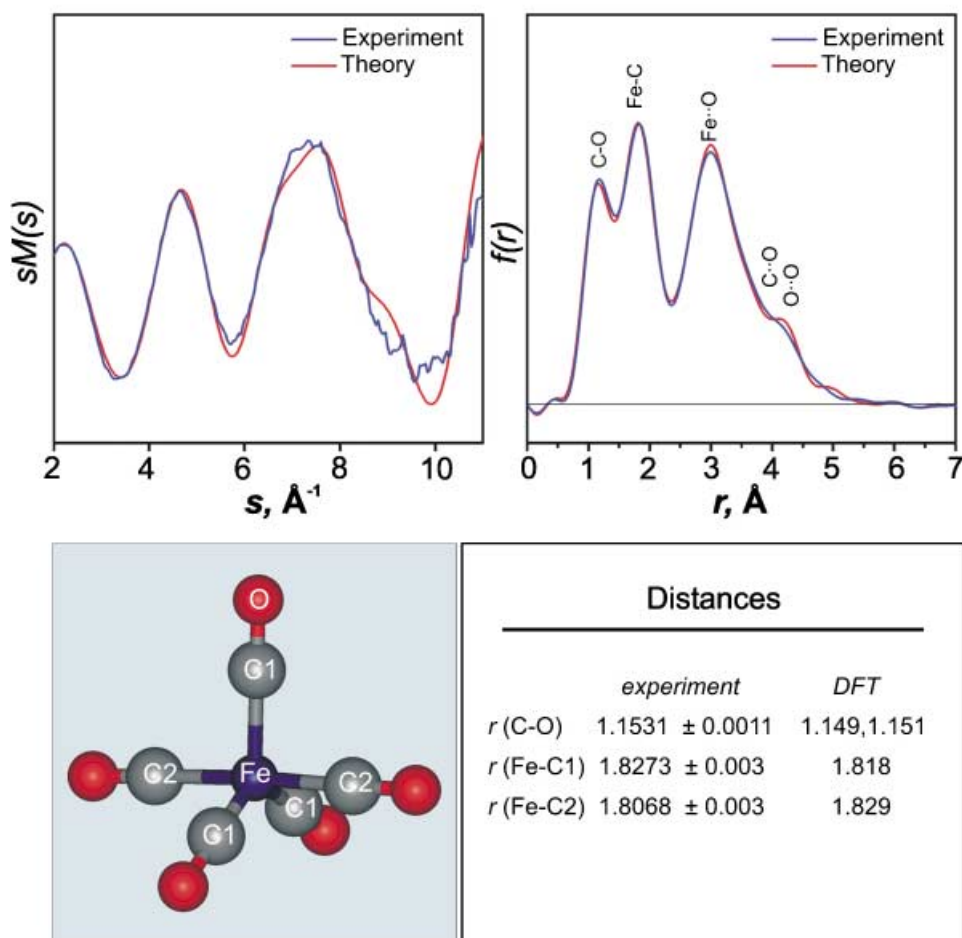
Molecular Structure of $\text{Fe}(\text{CO})_5$ 

Fig. 34. Refined ground-state structure of $\text{Fe}(\text{CO})_5$. Comparison of experimental curve (blue) with corresponding theoretical calculations (red) for the ground state of the parent $\text{Fe}(\text{CO})_5$. The experimental structural parameters shown are from GED data [141], along with the DFT values. Distances are in \AA , and angles are in degrees.

$\text{C}\cdots\text{O}$ and $\text{O}\cdots\text{O}$, in the liberation process. The small peak for the $\text{C}-\text{O}$ bond at $\sim 1.12 \text{\AA}$ is negative because the liberated CO ligand has a shorter bond distance than that of the bound ligand ($\sim 1.15 \text{\AA}$), but the negative amplitude of the peak is small because the change (from 1.15 to 1.12 \AA) is minute, causing the positive and negative contributions to nearly cancel out.

The structure of $\text{Fe}(\text{CO})_4$ obtained from our UED experiment was further refined by limiting the fit to a single product and floating all the independent structural parameters. The best-fit bond distances and angles are given in Fig. 35; the error bars

Refinement of Structure and Its Spin State

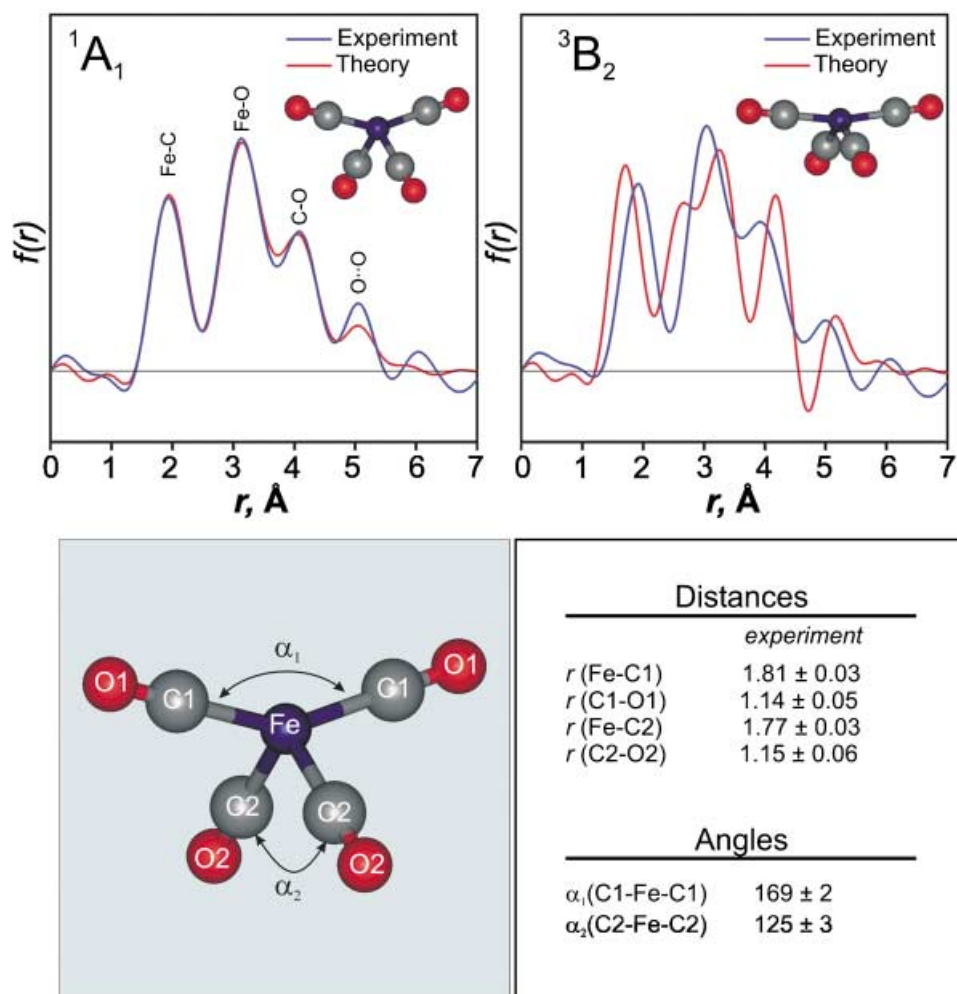


Fig. 35. Identification of spin state and refined transient structure of $Fe(CO)_4$. Top: Comparison of experimental $-\Delta f(+200 \text{ ps}; -180 \text{ ps}; r)$ curves (blue) with corresponding theoretical calculations (red) obtained via *ab initio* structures of the 1A_1 state (left) and the 3B_2 state (right). The structures of the 1A_1 and 3B_2 electronic states for the intermediate $Fe(CO)_4$ species are also shown. Bottom: The refined *singlet* $Fe(CO)_4$ structure along with the corresponding best-fit bond distances and angles. Distances are in Å, and angles are in degrees.

represent one standard deviation and do not account for systematic errors. The structure determined here is globally consistent with *ab initio* calculations [142] for the 1A_1 state.

Many spectroscopic and theoretical studies have concluded that the structure is that of the triplet channel (see, e.g., [143–146]). *Poliakoff* and *Turner* [147] in their matrix-

isolated studies of $\text{Fe}(\text{CO})_4$ found a species other than the triplet ground-state and tentatively assigned the species to be in the singlet state. Their careful analysis of IR intensities led them to obtain $173.5 \pm 1^\circ$ and $125 \pm 2.5^\circ$ for C–Fe–C angles, which are remarkably close to our experimental UED values obtained for the isolated species. *Trushin et al.* [148] in the gas-phase concluded that $\text{Fe}(\text{CO})_5$ dissociates into the singlet $\text{Fe}(\text{CO})_4$ state. Thus, the identification of the reaction pathway and the determination of the structure of the isolated intermediate (with its spin state) are vital to any conclusion regarding the mechanism of these complex organometallic reactions [149].

Coherence in UED Patterns

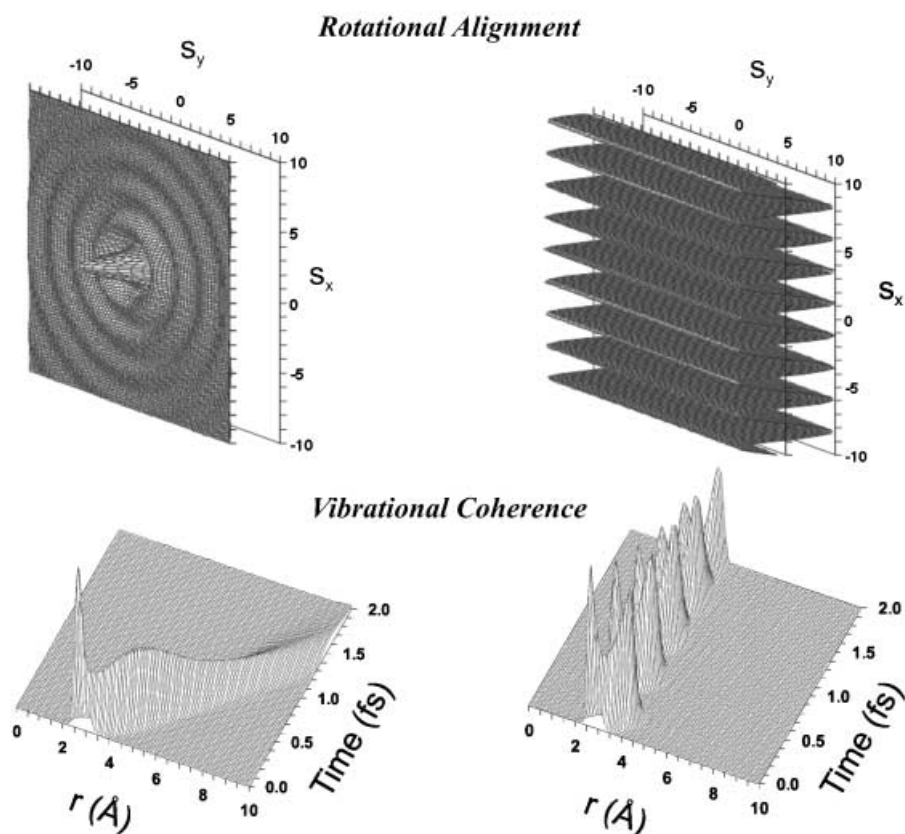


Fig. 36. *Coherence in UED patterns.* *Top:* Rotational alignment effects. *Left:* $sM(s)$ pattern of an isotropic sample of molecular iodine. *Right:* $sM(s)$ pattern of molecular iodine with total spatial (perpendicular) alignment. The amplitude of the interference fringes is approximately an order of magnitude larger than that from an isotropic sample, (see [28]). *Bottom:* Vibrational coherence effects. *Left:* $f(r)$ curve of B-state iodine excited *above* the dissociation energy. The hump at 400 fs appears because the wave packet slows down as it climbs the outer potential wall before dissociation. *Right:* $f(r)$ curve of B-state iodine excited *below* the dissociation energy. The peak intensity at the inner and outer turning points decreases as a function of time, which shows that the classical wave packet is spreading and approaching a static distribution (see [25][28]).

5. The Future of Ultrafast Electron Diffraction

In 1937, *Davisson* and *Thomson* received the Nobel Prize ‘for their experimental discoveries of the diffraction of electrons by crystals’. Earlier in the century, X-ray diffraction from crystals had been discovered; but, for gases, it was *Debye* and co-workers [21][150] who showed that X-ray scattering patterns are rich with structural information, despite the randomness in the position and orientation of the gaseous molecular samples. Over the past 70 years, ever since the pioneering work of *Mark* and *Wierl* [20], gas phase *continuous-beam* electron diffraction has become a powerful tool for studying the *static* nature of molecular structures. Within just five years of the first GED experiment, *Brockway* [45] listed in his review the structures of 44 inorganic and 103 organic molecules determined by GED. Since then, thousands of *static* molecular structures have been reported in the literature [46]. Aided by advances in instrumentation, theoretical insights, and computational analysis procedures, the field has witnessed several stages of evolution – the visual method, the sector-microphotometer method, and now, the ultrafast imaging of transient structures, as noted by *Jerome Karle* [151]. The central theme in ultrafast electron diffraction (UED) is the elucidation of the structural dynamics of *transient* molecular entities.

Reaching the spatiotemporal resolution on the atomic scale is the driving force behind the development of UED, the subject of this review. The current state-of-the-art in resolutions and sensitivity of UED (0.01 Å, 1 ps, and 1%, resp.), together with the theoretical advances made, make possible the freezing of transient structures, leading to studies of diverse molecular phenomena hitherto not accessible to other techniques (see *Fig. 9* and *Chapt. 4*). Of particular significance is the ability to observe evolution of structures on complex energy landscapes, including those far from equilibrium and with no heavy atoms.

On the ultrashort timescale, both the rotational and vibrational motions of molecules are coherent; a degree of order is imposed on the otherwise isotropic sample at equilibrium. It is, therefore, necessary to consider the structural changes, both in this regime of coherent dynamics, and when coherence is subsequently lost. The current time resolution allows us to determine both the *structure* and the *population* of transient intermediates at each instant in time. It is also possible to exploit the coherent motion of atoms to observe new structural features as revealed by our theoretical studies on the impact of rotational and vibrational coherences on the scattering pattern [28]. It has been shown that an additional dimension of imaging can be achieved at times when coherence is induced or recovered – in a sense, *Debye’s* ring pattern begins to approach the diffraction from a crystalline sample. The X-ray crystallography method of using different crystal orientations to map out the structure of the unit-cell can be imitated in UED by exciting different orientations (*Fig. 36*) [28][152]. Furthermore, vibrational coherence studies provide a map of the potential energy surface, as illustrated in *Fig. 36* for a diatomic molecule.

The first three generations of UED have been devoted to studies of isolated, complex structures. Currently, in this laboratory, a major step forward in the evolution of UED is the development of the fourth-generation apparatus (UED-4) designed for diffraction studies of surfaces and macromolecules on the ultrafast timescale, thus opening up the world of the condensed phase, and biology. With the electron-pulse

sequencing of the diffraction-difference method, the six-orders-of-magnitude higher cross-section of electron scattering (compared to X-rays) and the development of femtosecond pulsed-electron sources [153–156], the technique is poised to reach single molecule studies of complex structures [157–159].

In December 1999, *Philip Ball* of *Nature* observed [160], ‘*Diffraction on the ‘molecular’ timescale of femtoseconds is an infant discipline which promises wonders once perfected, but which is capable right now of only the crudest of impressionistic sketches: blurred images of lattice dynamics, showing evidence of rapid change but without a single molecule (let alone an atom) in focus. The static photography of the Braggs has yet to produce its first movie.*’ UED has not only succeeded in bringing isolated molecules into sharp focus but has also captured the crucial ‘freeze frames’ in these movies. As noted by several colleagues [149][161–167], the recent triumphs of UED have generated much excitement for the burgeoning field of ‘structural dynamics’.

Acknowledgements

We gratefully acknowledge the generous support of the *National Science Foundation* for building the new generations of UED. Partial support was provided by the *Air Force Office of Scientific Research*. *A. H. Z.* and the co-authors (listed below in parentheses) would also like to acknowledge colleagues in our laboratory at Caltech whose contributions over the years have been instrumental in the successful evolution of UED from its infancy to the current state-of-the-art. In chronological order, they are: *J. Charles Williamson, Marcos Dantus, Scott B. Kim, Hans Frey, Hyotcherl Ihee, Jianming Cao, Udo M. Gomez, (Vladimir A. Lobastov), (Ramesh Srinivasan), Boyd M. Goodson, (Chong-Yu Ruan), Jonathan S. Feenstra, Franco Vigliotti, Songye Chen, Sang Tae Park, and Shoujun Xu* – the published contributions have been listed in the references. We wish to also thank the late Prof. *Verner Schomaker*, late Prof. *John D. Ewbank*, Prof. *Hani Elsayed-Ali*, and Prof. *István Hargittai* for sharing with us over the years their experience of electron diffraction; and late Prof. *Alexander Prokhorov* and Prof. *Mikhail Schelev* for the collaboration on femtosecond electron sources.

REFERENCES

- [1] ‘The Chemical Bond: Structure and Dynamics’, Ed. A. H. Zewail, Academic Press, San Diego, California, 1992.
- [2] B. Kojic-Prodic, J. Kroon, *Croat. Chem. Acta* **2001**, *74*, 1.
- [3] A. H. Zewail, in ‘Les Prix Nobel: The Nobel Prizes 1999’, Ed. T. Frängsmyr, Almqvist & Wiksell, Stockholm, 2000, p. 103.
- [4] ‘Femtochemistry: Ultrafast Dynamics of the Chemical Bond’, Ed. A. H. Zewail, World Scientific, Singapore, 1994.
- [5] ‘Femtosecond Chemistry’, Eds. J. Manz, L. Wöste, VCH, Weinheim, 1995.
- [6] ‘Femtochemistry: Ultrafast Chemical and Physical Processes in Molecular Systems’, Ed. M. Chergui, World Scientific, Singapore, 1996.
- [7] ‘Femtochemistry and Femtobiology: Ultrafast Reaction Dynamics at Atomic-Scale Resolution’, Ed. V. Sundström, Imperial College Press, London, 1997.
- [8] ‘Femtochemistry’, Eds. F. C. De Schryver, S. De Feyter, G. Schweitzer, Wiley-VCH, Weinheim, 2001.
- [9] ‘Femtochemistry and Femtobiology: Ultrafast Dynamics in Molecular Science’, Eds. A. Douhal, J. Santamaria, World Scientific, Singapore, 2002.
- [10] M. T. Zanni, R. M. Hochstrasser, *Curr. Opin. Struct. Biol.* **2001**, *11*, 516.
- [11] S. Mukamel, ‘Principles of Nonlinear Optical Spectroscopy’, Oxford University Press, New York, 1995.
- [12] J.-C. Gauthier, A. Rousse, *J. Phys. IV* **2002**, *12*, 59.
- [13] C. W. Siders, A. Cavalleri, *Science* **2003**, *300*, 591.

- [14] A. Rousse, C. Rischel, J.-C. Gauthier, *Rev. Mod. Phys.* **2001**, 73, 17.
- [15] L. X. Chen, W. J. H. Jäger, G. Jennings, D. J. Gosztola, A. Munkholm, J. P. Hessler, *Science* **2001**, 292, 262.
- [16] D. A. Ouilanov, I. V. Tomov, A. S. Dvornikov, P. M. Rentzepis, *Proc. Natl. Acad. Sci. U.S.A.* **2002**, 99, 12556.
- [17] F. Ráksi, K. R. Wilson, Z. Jiang, A. Ikhlef, C. Y. Côté, J.-C. Kieffer, *J. Chem. Phys.* **1996**, 104, 6066.
- [18] M. Saes, C. Bressler, R. Abela, D. Grolimind, S. L. Johnson, P. A. Heimann, M. Chergui, *Phys. Rev. Lett.* **2003**, 90, 0474031.
- [19] I. Hargittai, in 'Stereochemical Applications of Gas-Phase Electron Diffraction, Part. A: The Electron Diffraction Technique', Ed. I. Hargittai, M. Hargittai, VCH, New York, 1988, p. 1.
- [20] H. Mark, R. Wierl, *Naturwissenschaften* **1930**, 18, 205.
- [21] P. Debye, L. Bewilogua, F. Ehrhardt, *Phys. Z.* **1929**, 30, 84.
- [22] A. Klug, in 'Les Prix Nobel: The Nobel Prizes 1982', Ed. W. Odelberg, Almqvist & Wiksell, Stockholm, 1983, p. 93.
- [23] R. Henderson, *Q. Rev. Biophys.* **1995**, 28, 171.
- [24] A. H. Zewail, *Faraday Discuss.* **1991**, 91, 207.
- [25] J. C. Williamson, A. H. Zewail, *Proc. Natl. Acad. Sci. U.S.A.* **1991**, 88, 5021.
- [26] J. C. Williamson, M. Dantus, S. B. Kim, A. H. Zewail, *Chem. Phys. Lett.* **1992**, 196, 529.
- [27] J. C. Williamson, A. H. Zewail, *Chem. Phys. Lett.* **1993**, 209, 10.
- [28] J. C. Williamson, A. H. Zewail, *J. Phys. Chem.* **1994**, 98, 2766.
- [29] M. Dantus, S. B. Kim, J. C. Williamson, A. H. Zewail, *J. Phys. Chem.* **1994**, 98, 2782.
- [30] J. C. Williamson, J. Cao, H. Ihee, H. Frey, A. H. Zewail, *Nature* **1997**, 386, 159.
- [31] H. Ihee, J. Cao, A. H. Zewail, *Chem. Phys. Lett.* **1997**, 281, 10.
- [32] J. Cao, H. Ihee, A. H. Zewail, *Chem. Phys. Lett.* **1998**, 290, 1.
- [33] J. Cao, H. Ihee, A. H. Zewail, *Proc. Natl. Acad. Sci. U.S.A.* **1999**, 96, 338.
- [34] H. Ihee, A. H. Zewail, W. A. Goddard III, *J. Phys. Chem. A* **1999**, 103, 6638.
- [35] H. Ihee, V. A. Lobastov, U. Gomez, B. M. Goodson, R. Srinivasan, C.-Y. Ruan, A. H. Zewail, *Science* **2001**, 291, 458.
- [36] H. Ihee, J. Cao, A. H. Zewail, *Angew. Chem., Int. Ed.* **2001**, 40, 1532.
- [37] H. Ihee, J. Kua, W. A. Goddard III, A. H. Zewail, *J. Phys. Chem. A* **2001**, 105, 3623.
- [38] C.-Y. Ruan, V. A. Lobastov, R. Srinivasan, B. M. Goodson, H. Ihee, A. H. Zewail, *Proc. Natl. Acad. Sci. U.S.A.* **2001**, 98, 7117.
- [39] V. A. Lobastov, R. Srinivasan, B. M. Goodson, C.-Y. Ruan, J. S. Feenstra, A. H. Zewail, *J. Phys. Chem. A* **2001**, 105, 11159.
- [40] H. Ihee, J. S. Feenstra, J. Cao, A. H. Zewail, *Chem. Phys. Lett.* **2002**, 353, 325.
- [41] H. Ihee, B. M. Goodson, R. Srinivasan, V. Lobastov, A. H. Zewail, *J. Phys. Chem. A* **2002**, 106, 4087.
- [42] B. M. Goodson, C.-Y. Ruan, V. A. Lobastov, R. Srinivasan, A. H. Zewail, *Chem. Phys. Lett.* **2003**, 374, 417.
- [43] C. J. Davisson, L. H. Germer, *Phys. Rev.* **1927**, 30, 705.
- [44] G. P. Thomson, A. Reid, *Nature* **1927**, 119, 890.
- [45] L. O. Brockway, *Rev. Mod. Phys.* **1936**, 8, 231.
- [46] 'Stereochemical Applications of Gas-Phase Electron Diffraction', Eds. I. Hargittai, M. Hargittai, VCH, New York, 1988.
- [47] 'Fifty Years of Electron Diffraction', Ed. P. Goodman, D. Reidel Publishing, Dordrecht, 1981.
- [48] V. S. Mastryukov, *Vib. Spectra Struct.* **2000**, 24, 85.
- [49] L. Pauling, L. O. Brockway, *J. Am. Chem. Soc.* **1935**, 57, 2684.
- [50] F. Trendelenburg, *Naturwissenschaften* **1933**, 21, 173.
- [51] C. Finbak, *Avh. Norsk Vidensk.-Akad. Oslo* **1937**, 13.
- [52] P. P. Debye, *Phys. Z.* **1939**, 66, 404.
- [53] M. Fink, R. A. Bonham, *Rev. Sci. Instrum.* **1970**, 41, 389.
- [54] R. A. Bonham, M. Fink, 'High Energy Electron Scattering', Van Nostrand Reinhold, New York, 1974.
- [55] M. Fink, P. G. Moore, D. Gregory, *J. Chem. Phys.* **1979**, 71, 5227.
- [56] J. D. Ewbank, L. Schäfer, D. W. Paul, O. J. Benston, J. C. Lennox, *Rev. Sci. Instrum.* **1984**, 55, 1598.
- [57] A. A. Ischenko, V. V. Golubkov, V. P. Spiridonov, A. V. Zgurskii, A. S. Akhmanov, M. G. Vabishevich, V. N. Bagratashvili, *Appl. Phys., B* **1983**, 32, 161.
- [58] A. P. Rood, J. Milledge, *J. Chem. Soc., Faraday Trans. 2* **1984**, 80, 1145.
- [59] L. S. Bartell, T. S. Dibble, *J. Am. Chem. Soc.* **1990**, 112, 890.
- [60] J. D. Ewbank, W. L. Faust, J. Y. Luo, J. T. English, D. L. Monts, D. W. Paul, Q. Dou, L. Schäfer, *Rev. Sci. Instrum.* **1992**, 63, 3352.

- [61] A. A. Ischenko, L. Schäfer, J. D. Ewbank, in 'Time-Resolved Diffraction', Eds. J. R. Helliwell, P. M. Rentzepis, Oxford University Press, New York, 1997, p. 323.
- [62] G. Mourou, S. Williamson, *Appl. Phys. Lett.* **1982**, *41*, 44.
- [63] S. Williamson, G. Mourou, J. C. M. Li, *Phys. Rev. Lett.* **1984**, *52*, 2364.
- [64] H. E. Elsayed-Ali, G. A. Mourou, *Appl. Phys. Lett.* **1988**, *52*, 103.
- [65] M. Aeschlimann, E. Hull, J. Cao, C. A. Schmittenmaier, L. G. Jahn, Y. Gao, H. E. Elsayed-Ali, D. A. Mantell, M. R. Scheinfein, *Rev. Sci. Instrum.* **1995**, *66*, 1000.
- [66] R. C. Dudek, P. M. Weber, *J. Phys. Chem. A* **2001**, *105*, 4167.
- [67] S. Ryu, P. M. Weber, R. M. Stratt, *J. Chem. Phys.* **2000**, *112*, 1260.
- [68] J. D. Geiser, P. M. Weber, *J. Chem. Phys.* **1998**, *108*, 8004.
- [69] A. C. Yates, *Phys. Rev.* **1968**, *176*, 173.
- [70] 'International Tables for Crystallography', Eds. A. J. C. Wilson, E. Prince, Kluwer Academic Press, Dordrecht, 1999.
- [71] J. C. Williamson, Ph.D. Thesis, California Institute of Technology, 1998.
- [72] M. Y. Schelev, M. C. Richardson, A. J. Alcock, *Appl. Phys. Lett.* **1971**, *18*, 354.
- [73] T. Tsang, T. Srinivasan-Rao, J. Fischer, *Phys. Rev. B* **1991**, *43*, 8870.
- [74] P. Chen, *Particle Accelerators* **1987**, *20*, 171.
- [75] J. J. Su, T. Katsouleas, J. M. Dawson, *Phys. Rev. A* **1990**, *41*, 3321.
- [76] W. Pyckhout, N. Horemans, C. Van Alsenoy, H. J. Geise, D. W. H. Rankin, *J. Mol. Struct.* **1987**, *156*, 315.
- [77] D. Zhong, E. W.-G. Diau, T. M. Bernhardt, S. D. Feyter, J. D. Roberts, A. H. Zewail, *Chem. Phys. Lett.* **1998**, *298*, 129.
- [78] E. C. Lim, *Adv. Photochem.* **1997**, *23*, 165.
- [79] P. Avouris, W. M. Gelbart, M. A. El-Sayed, *Chem. Rev.* **1977**, *77*, 793.
- [80] N. Turro, 'Modern Molecular Photochemistry', University Science Books, Sausalito, California, 1991.
- [81] E. Villa, A. Amirav, E. C. Lim, *J. Phys. Chem.* **1988**, *92*, 5393.
- [82] A. L. Sobolewski, C. Woywood, W. J. Domcke, *J. Chem. Phys.* **1993**, *98*, 5627.
- [83] I. J. Palmer, I. N. Ragazos, F. Bernardi, M. Olivucci, M. A. Robb, *J. Am. Chem. Soc.* **1993**, *115*, 673.
- [84] I. Yamazaki, K. Sushida, H. Baba, *J. Chem. Phys.* **1979**, *71*, 381.
- [85] I. Yamazaki, T. Murao, T. Yamanaka, K. Yoshihara, *Faraday Discuss. Chem. Soc.* **1983**, *75*, 395.
- [86] C. E. Otis, J. L. Knee, P. M. Johnson, *J. Phys. Chem.* **1983**, *87*, 2232.
- [87] U. Schubert, E. Riedle, H. J. Neusser, E. W. Schlag, *J. Chem. Phys.* **1986**, *84*, 6182.
- [88] J. H. Callomon, J. E. Parkin, R. Lopez-Delgado, *Chem. Phys. Lett.* **1972**, *13*, 125.
- [89] M. Chachisvilis, A. H. Zewail, *J. Phys. Chem. A* **1999**, *103*, 7408.
- [90] L. R. Khundkar, A. H. Zewail, *J. Chem. Phys.* **1990**, *92*, 231.
- [91] D. Zhong, S. Ahmad, A. H. Zewail, *J. Am. Chem. Soc.* **1997**, *119*, 5978.
- [92] H. Thomassen, S. Samdal, K. Hedberg, *J. Am. Chem. Soc.* **1992**, *114*, 2810.
- [93] 'Free Radicals', Ed. J. K. Kochi, John Wiley & Sons, New York, 1973.
- [94] 'Handbook of Bimolecular and Termolecular Gas Reactions', Ed. J. A. Kerr, CRC Press, Boca Raton, 1981.
- [95] 'Free Radicals in Organic Chemistry', Eds. J. Fossey, D. Lefort, J. Sorba, John Wiley & Sons, New York, 1995.
- [96] P. S. Skell, D. L. Tuleen, P. D. Readio, *J. Am. Chem. Soc.* **1963**, *85*, 2849.
- [97] P. S. Skell, J. G. Traynham, *Acc. Chem. Res.* **1984**, *17*, 160.
- [98] B. Beagley, C. T. Parrott, V. Ulbrecht, G. G. Young, *J. Mol. Struct.* **1979**, *52*, 47.
- [99] I. W. Nowell, D. R. Russell, *J. Chem. Soc., Dalton Trans.* **1972**, 2393.
- [100] M. Y. Antipin, Y. T. Struchkov, A. N. Chernega, M. F. Meidine, J. F. Nixon, *J. Organomet. Chem.* **1992**, *436*, 79.
- [101] P. T. Snee, C. K. Payne, K. T. Kotz, H. Yang, C. B. Harris, *J. Am. Chem. Soc.* **2001**, *123*, 2255.
- [102] H. Wang, K. Brezinsky, *J. Phys. Chem. A* **1998**, *102*, 1530.
- [103] K. Pierloot, B. J. Persson, B. O. Roos, *J. Phys. Chem.* **1995**, *99*, 3465.
- [104] T.-K. Ha, R. Meyer, H. H. Günthard, *Chem. Phys. Lett.* **1980**, *69*, 510.
- [105] W. T. Borden, E. R. Davidson, *J. Am. Chem. Soc.* **1979**, *101*, 3771.
- [106] G. R. Liebling, H. M. McConnell, *J. Chem. Phys.* **1965**, *42*, 3931.
- [107] L. Yu, S. C. Foster, J. M. Williamson, M. C. Heaven, T. A. Miller, *J. Phys. Chem.* **1988**, *92*, 4263.
- [108] L. Yu, D. W. Cullen, J. M. Williamson, T. A. Miller, *J. Chem. Phys.* **1993**, *98*, 2682.
- [109] V. A. Korolev, O. M. Nefedov, *Russ. Chem. Bull.* **1993**, *42*, 1497.

- [110] M. Traetteberg, *J. Am. Chem. Soc.* **1964**, *86*, 4265.
[111] H. Oberhammer, S. H. Bauer, *J. Am. Chem. Soc.* **1969**, *91*, 10.
[112] J. M. Greathead, S. W. Orchard, *Int. J. Chem. Kinet.* **1983**, *15*, 1069.
[113] F. A. L. Anet, I. Yavari, *Tetrahedron Lett.* **1975**, *48*, 4221.
[114] B. E. Thomas IV, J. D. Evanseck, K. N. Houk, *Isr. J. Chem.* **1993**, *33*, 287.
[115] P. J. Reid, S. J. Doig, S. D. Wickham, R. A. Mathies, *J. Am. Chem. Soc.* **1993**, *115*, 4754.
[116] S. A. Trushin, S. Diemer, W. Fuß, K. L. Kompa, W. E. Schmid, *Phys. Chem. Chem. Phys.* **1999**, *1*, 1431.
[117] H.-M. Steuhl, C. Bornemann, M. Klessinger, *Chem.–Eur. J.* **1999**, *5*, 2404.
[118] A. Hertwig, H. Hippler, H. Schmid, A.-N. Unterreiner, *Phys. Chem. Chem. Phys.* **1999**, *1*, 5129.
[119] W. Paulick, C. Jung, U. Kempka, J. Sühnel, K. Gustav, *J. Mol. Struct.* **1981**, *85*, 235.
[120] A. A. Ischenko, L. Schäfer, J. Y. Luo, J. D. Ewbank, *J. Phys. Chem.* **1994**, *98*, 8673.
[121] E. W.-G. Diau, S. D. Feyter, A. H. Zewail, *J. Chem. Phys.* **1999**, *110*, 9785.
[122] K. B. Møller, A. H. Zewail, *Chem. Phys. Lett.* **1998**, *295*, 1.
[123] M. Yan, L. J. Rothberg, R. Callender, *J. Phys. Chem. B* **2001**, *105*, 856.
[124] P. J. Reid, A. P. Shreve, R. A. Mathies, *J. Phys. Chem.* **1993**, *97*, 12691.
[125] M. K. Lawless, S. D. Wickham, R. A. Mathies, *Acc. Chem. Res.* **1995**, *28*, 493.
[126] S. Lochbrunner, W. Fuss, W. E. Schmid, K. L. Kompa, *J. Phys. Chem. A* **1998**, *102*, 9334.
[127] N. A. Andersen, S. H. Pullen, L. A. Walker II, J. J. Shiang, R. J. Sension, *J. Phys. Chem. A* **1998**, *102*, 10588.
[128] W. Fuss, W. E. Schmid, S. A. Trushin, *J. Chem. Phys.* **2000**, *112*, 8347.
[129] D. C. Clary, A. J. H. M. Meijer, *J. Chem. Phys.* **2002**, *116*, 9829.
[130] A. Hoffman, R. de Vivie-Riedle, *Chem. Phys. Lett.* **2001**, *346*, 299.
[131] H.-G. Mack, H. Oberhammer, E. O. John, R. L. Kirchmeier, J. M. Shreeve, *J. Mol. Struct.* **1991**, *250*, 103.
[132] C. W. Mathews, *Can. J. Phys.* **1967**, *45*, 2355.
[133] W. H. Kirchhoff, D. R. Lide Jr., F. X. Powell, *J. Mol. Spectrosc.* **1973**, *47*, 491.
[134] M. R. Cameron, S. H. Kable, G. B. Bacskey, *J. Chem. Phys.* **1995**, *103*, 4476.
[135] B.-S. Cheong, H.-G. Cho, *J. Phys. Chem. A* **1997**, *101*, 7901.
[136] Z.-L. Cai, *J. Phys. Chem.* **1993**, *97*, 8399.
[137] N. Russo, E. Sicilia, M. Toscano, *J. Chem. Phys.* **1992**, *97*, 5031.
[138] C. W. Bauschlicher Jr., H. F. Schaefer III, P. S. Bagus, *J. Am. Chem. Soc.* **1977**, *99*, 7106.
[139] M. Wrighton, *Chem. Rev.* **1974**, *74*, 401.
[140] M. Poliakoff, E. Weitz, *Acc. Chem. Res.* **1987**, *20*, 408.
[141] B. Beagley, D. G. Schmidling, *J. Mol. Struct.* **1974**, *22*, 466.
[142] O. González-Blanco, V. Branchadell, *J. Chem. Phys.* **1999**, *110*, 778.
[143] T. A. Seder, A. J. Ouderkirk, E. Weitz, *J. Chem. Phys.* **1986**, *85*, 1977.
[144] I. M. Waller, J. W. Hepburn, *J. Chem. Phys.* **1988**, *88*, 6658.
[145] B. K. Venkataraman, G. Bandukwalla, Z. Zhang, M. Vernon, *J. Chem. Phys.* **1989**, *90*, 5510.
[146] A. Veillard, A. Strich, C. Daniel, P. E. M. Siegbahn, *Chem. Phys. Lett.* **1987**, *141*, 329.
[147] M. Poliakoff, J. J. Turner, *J. Chem. Soc., Dalton Trans.* **1974**, 2276.
[148] S. A. Trushin, W. Fuss, K. L. Kompa, W. E. Schmid, *J. Phys. Chem. A* **2000**, *104*, 1997.
[149] M. Poliakoff, J. J. Turner, *Angew. Chem., Int. Ed.* **2001**, *40*, 2809.
[150] P. Debye, *Ann. Phys.* **1915**, *46*, 809.
[151] J. Karle, *Struct. Chem.* **2000**, *11*, 91.
[152] K. Hoshina, K. Yamanouchi, T. Ohshima, Y. Ose, H. Todokoro, *J. Chem. Phys.* **2003**, *118*, 6211.
[153] M. Y. Schelev, G. I. Bryukhnevich, M. A. Monastyrski, A. M. Prokhorov, A. V. Smirnov, N. S. Vorobiev, *Opt. Eng.* **1998**, *37*, 2249; H. Niu, V. P. Degtyareva, V. N. Platonov, A. M. Prokhorov, M. Y. Schelev, *Proc. SPIE* **1988**, *1032*, 79.
[154] B.-L. Qian, H. E. Elsayed-Ali, *Rev. Sci. Instrum.* **2001**, *72*, 3507.
[155] B.-L. Qian, H. E. Elsayed-Ali, *Phys. Rev. E* **2002**, *65*, 046502.
[156] B. J. Siwick, J. R. Dwyer, R. E. Jordan, R. J. D. Miller, *J. Appl. Phys.* **2002**, *92*, 1643.
[157] J. Hajdu, *Curr. Opin. Struct. Biol.* **2000**, *10*, 569.
[158] J. Miao, K. O. Hodgson, D. Sayre, *Proc. Natl. Acad. Sci. U.S.A.* **2001**, *98*, 6641.
[159] G. Webster, R. Hilgenfeld, *Single Mol.* **2002**, *3*, 63.
[160] P. Ball, *Nature* **1999**, *402*, C30 Suppl.
[161] J. M. Thomas, *Nature* **1991**, *351*, 694.
[162] R. Hoffmann, *Am. Sci.* **1999**, *87*, 308.
[163] J. R. Helliwell, *Phys. World* **2001**, *14*, 25.

- [164] E. Wilson, *Chem. Eng. News* **2001**, 79, 10.
- [165] N. Hall, *Chem. Commun.* **2002**, 2185.
- [166] J. M. Thomas, *Faraday Discuss.* **2002**, 122, 395.
- [167] P. Coppens, I. V. Novozhilova, *Faraday Discuss.* **2002**, 122, 1.
- [168] I. L. Karle, J. Karle, *J. Chem. Phys.* **1950**, 18, 963.

Received May 26, 2003